Spatial Coulomb effects in semiconductor quantum dot devices

vorgelegt von

Diplom-Physiker
Reinhard Wetzler
aus Erding

von der Fakultät II - Mathematik und Naturwissenschaften
der Technischen Universität Berlin
zur Erlangung des akademischen Grades
Doktor der Naturwissenschaften
Dr. rer. nat.
genehmigte Dissertation

Promotionsausschuss:

Vorsitzender:	Prof. Dr. M. Dähne
Berichter:	Prof. Dr. E. Schöll, PhD
Berichter:	Dr. A. Wacker

Tag der wissenschaftlichen Aussprache: 09. Dezember 2003

Berlin 2003
D83

Zusammenfassung

Die Kapazität-Spannung (C-V) Spektroskopie bietet eine experimentelle Möglichkeit, Quantenpunkte (QDs) elektrisch zu untersuchen. Ohne detaillierte Simulationen war es bisher jedoch nicht möglich, genauere Interpretationen der experimentellen Daten zuzulassen. Die C-V Charakteristiken stellen eine Abbildung der zum Teil sehr komplizierten räumlichen Ladungsverteilung einer Struktur dar, weshalb in dieser Arbeit mehrere theoretische Modelle entwickelt werden, um diese zu berechnen. Es werden numerische Simulationen von Dioden mit QDs durchgeführt, z.B. zur Bestimmung der Energieniveaus in den QDs und deren homogene Verbreiterung durch einen Vergleich mit experimentellen Daten. Die dreidimensionalen Rechnungen zeigen, daß die Coulomb-Wechselwirkung zwischen den QDs eine zentrale Stellung einnimmt. Sie führt zusammen mit der inhomogenen Ladungsverteilung in der Schicht der QDs selbst bei Vernachlässigung aller wachstumsbedingten Fluktuationen zu einem intrinsischen Verbreiterungsmechanismus der diskreten Zustandsdichte einzelner QDs. Diese hängt zudem stark von der elektronischen Umgebung der QDs ab, die sich z.B. durch die angelegte Spannung ändern kann. Es werden QDs ohne strukturelle Fluktuationen aber auch mit zufälligen Fluktuationen sowie Ensembles von QDs, die aus Wachstumssimulationen entnommen werden, simuliert. Generell lassen nur diese sehr detaillierten Rechnungen eine Interpretation von experimentellen Daten bezüglich der Größenverteilung zu.

Die räumliche Ladungsverteilung auf immer kleinem Raum wirft natürlich auch die Frage nach der Rolle von Coulomb-Streuung zwischen Elektronen an unterschiedlichen Orten und von unterschiedlicher Dimension auf. Im Speziellem wird hier auf Strukturen im Zusammenhang mit QDs eingegangen, also die Streuung zwischen Elektronen in den QDs und räumlich ausgedehnten, drei- und zweidimensionalen Elektronen. Es zeigt sich dabei, daß eine solche Kinetik stark auf den Ort der QDs begrenzt ist.

Abstract

Capacitance-Voltage (C-V) spectroscopy provides an experimental method to investigate the electrical properties of quantum dots (QDs). So far, without detailed simulations it has not been possible to give clear interpretations of the experimental data. C-V characteristics represent a mapping of the very complicated spatial charge distribution of a device which can be calculated by the theoretical models developed in this work. Numerical simulations of diodes are performed, e.g., to obtain values for the QD energy levels and their homogeneous broadenings by a fit to experimental data. The three-dimensional simulations show that the Coulomb interaction between the QDs is of central importance. Together with the inhomogeneous charge distribution in the QD layer it leads to an intrinsic broadening mechanism of the zero-dimensional QD density of states, even if all structural fluctuations are neglected. These interactions between QDs depend strongly on the electronic environment of the QDs which can be changed, e.g., by applying a bias. QDs without structural fluctuations but also QDs with random fluctuations and QDs taken from growth simulations are investigated. Generally, only the detailed calculations performed here make an interpretation of the experimental data regarding the size fluctuations possible.

The spatial charge distribution on an increasingly smaller length-scale of course raises the question about the role of Coulomb scattering between electrons of different dimensions and located at different positions. In this work structures with QDs are investigated, i.e., the scattering between electrons in the QDs and spatially extended, two- and three-dimensional electrons. It is shown that such kinetics has a strong local character.

Contents

1 Introduction

1.1 General background

Over the last decades, semiconductor physics and technology has distinguished itself by the rapid pace of improvement of applications used in information technology. Integration level, cost-per-function, speed, power consumption, compactness and functionality are the principal categories of improvement. Most of these trends have resulted principally from the technological ability to exponentially decrease the minimum feature sizes used to fabricate integrated circuits. Of course, the most frequently cited trend is in integration level which is usually expressed as Moore's Law [Moo65]: "The number of components per chip doubles every 18 months". The ongoing demand for further miniaturization has led to structure sizes of typically 100-200 nanometers in nowadays commercial computer chips. The most significant trend for society is the decreasing cost-per-function which has led to significant improvements of productivity and quality of life through proliferation of computers, electronic communication, and consumer electronics.

Understanding and controlling the properties of materials is becoming the crucial step required for improving the information technology on which our modern life is increasingly built. Therefore, one goal of research is to develop theoretical models and apply feasible computational techniques for modeling the linear and nonlinear response properties of semiconductor nanostructures.

1.2 Quantum dots

In the pursuit of further miniaturization of semiconductor devices, such as transistors or diodes, nanometer technology made it possible that the spatial motion of electrons was confined from three to lower dimensions. In this progress, one is currently reaching the regime where a quantum mechanical description and Coulomb effects gain relevance, substituting standard "bulk" semiconductor physics. New terms as two-dimensional electron gas (2DEG) or one-dimensional quantum wire were brought to life in material science.

Confining few electrons in all three spatial dimensions within a small potential box and reducing the spatial motion of the electrons to zero dimensions denotes the ultimative miniaturization in semiconductor technology. Similarly as in atoms, according to quantum mechanical laws, electrons occupy discrete energy levels. Therefore, such semiconductor structures are called quantum dots or QDs (see Ref. [Bim99] and references therein for a more detailed introduction about QDs).

Modern epitaxial techniques allow to form crystal layers with atomic precision. Wetting a plain crystal surface with a lattice mis-matched material may lead under certain conditions to the so-called self-organized formation of QDs. The resulting QDs can be very small, from a few up to several hundreds of nanometers, of regular size and shape and may be grown with very high surface densities. The detailed kinetics leading to the formation of regular QDs have been subject of recent investigations [Sch98b, Shc98, Mei01c, Mei01a, Mei01b, Mei02b, Mei03a, Mei03b]. Interestingly, such a growth process has been described already in 1938 by Stranski and Krastanov [Str39], but the first successful realizations of such semiconductor structures have been reported only about a decade ago [Eag90, Mo90].

Since then, different applications based on QDs have been demonstrated, such as charge storage in field-effect transistor structures [Yus97, Yus98, Fin98, Koi00] or laser devices (see Ref. [Gru00a] and references therein). For all kinds of applications, the detailed

understanding of the electronic structure and the exchange with the surrounding semiconductor matrix is of essential importance.

1.3 This work

Capacitance-voltage (C-V) spectroscopy is a successful method to investigate QDs electrically. The modifications of the local charge and potential distribution due to the charged QDs embedded in a diode provide information about the QDs themselves. Unfortunately, the spatial charge and potential distribution in such devices is rather complicated, and new theoretical approaches are necessary to provide a deeper understanding of the experimental capacitance signals.

In layers of small QDs, where single QDs can confine only few electrons one has to deal with three important parameters: (i) the quantum mechanical confining energy which will suffer from size fluctuations of the QDs, (ii) the charging energy, i.e., the Coulomb repulsion of more than one electron in a QD, and (iii) the Coulomb repulsion of electrons within neighboring QDs. All three parameters are typically of about equal size. It is therefore one of the aims of this work to evaluate the role of Coulomb charging effects and structural fluctuations, i.e., size and position fluctuations of QDs within a layer of self-organized QDs.

The three-dimensional character of a structure with embedded QDs makes it necessary to provide a spatially three-dimensional description of the potential and charge distribution in QD devices. The electric field and the charge carrier distribution are related to each other by a set of differential equations, i.e., the Poisson equation and transport equations. The charge distribution which solves all equations simultaneously is called the self-consistent solution. There exist sophisticated techniques to find these solutions, usually involving an iteration scheme. Especially for arrays of many QDs this can result in numerical and conceptional difficulties. Additionally, if including the charge distribution of a whole QD device,

length scales of tenth of nanometers up to several microns have to be treated simultaneously.

After a short introduction to C-V spectroscopy in chapter 2, the self-consistent models used in this work are proposed in chapter 3. The one-dimensional model is used to find values for the energy levels in the QDs and their broadenings by a fit of simulated C-V curves to experimental data in chapter 4. The three-dimensional model, also proposed in chapter 3, allows an effective and feasible numerical solution of the non-linear three-dimensional Poisson equation. It is a huge improvement towards a more detailed description compared to the one-dimensional model. Simulations of equi-sized and periodically ordered arrays QDs show that Coulomb charging is strongly effected by the charge distribution in the semiconductor matrix the QDs are embedded in (chapter 5). With the ability to simulate arbitrary ensembles of QDs, size and position fluctuations of QDs as well as temperature fluctuations are investigated in chapter 6.

Additionally, the electron kinetics which is of principal scientific interest and is important for applications such as memory devices can be influenced by carriers in the vicinity of the QDs. Scattering between the QD electrons and continuum carriers in the vicinity by Coulomb forces can contribute to the energy relaxation or excitation in QDs, overcoming the so-called phonon bottleneck. A theory for a detailed description of remote Coulomb scattering or Auger-type scattering with two- or three-dimensional continuum electrons is proposed in chapter 7. The resulting scattering rates for different device geometries are shown in chapter 8, discussing the general role of Coulomb scattering in QD structures.

Finally, the main results are briefly summarized at the end of this work.

2 C-V spectroscopy

When investigating semiconductor structures such as QDs by capacitance-voltage (C-V) spectroscopy, these structures usually have to be embedded in diodes as the *pn* junction. Since the *pn* diodes provide a background capacitance, its origin is briefly revisited first.

2.1 Depletion layer capacitance

If an *n*-doped and a *p*-doped semiconductor material are brought in electrical contact, charge in form of free carriers will flow until both parts are in thermodynamic equilibrium. As a consequence, ionized donors and acceptors are left behind in the vicinity of the interface leading to a local violation of the charge neutrality. The layer depleted of free carriers is usually referred to as the "depletion layer". The depletion layer width for an abrupt, one-sided (e.g. the acceptor concentration is much larger than the donor concentration) junction is given by [Sze81]

$$W = \sqrt{\frac{2\epsilon_0\epsilon_r(U_{bi} - U)}{eN_B}}. \tag{2.1}$$

Here, U_{bi} is the built-in potential, i.e., the difference between the conduction band edge between the two contacts in equilibrium, U is the applied bias, N_B is the lower doping concentration, ϵ_0 and ϵ_r are the absolute and relative permittivities, and $e > 0$ is the elementary charge. Figure 2.1 shows for example a sketch of the conduction band profile for an *n*-sided *pn* diode. Equation 2.1 is found straight forwardly from solving the Poisson equation for an abrupt *pn* junction. The depletion layer capacitance per unit area

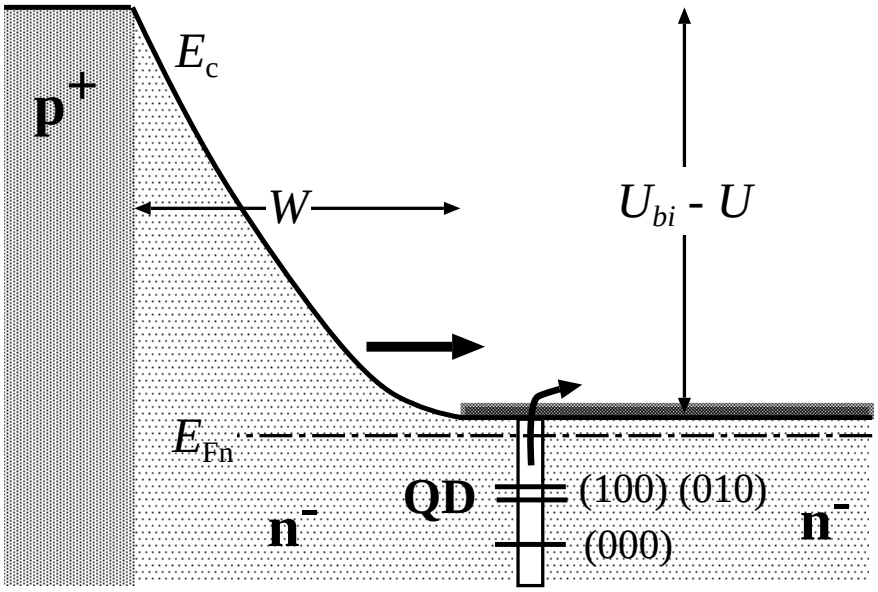

Figure 2.1: Sketch of the band profile of a *pn* diode with depletion layer width W; A sheet of QDs with discrete energy levels is positioned in the n^--doped layer.

is defined as

$$C = \left| \frac{dQ}{dU} \right|, \tag{2.2}$$

where dQ is the incremental change in the depletion layer charge per unit area for an incremental change in the applied voltage dU. The incremental space charges on the n- and p-sides of the depletion region are equal but with opposite polarity, thus maintaining overall charge neutrality. This incremental charge dQ results a change in the electric field by an amount $dQ/(\epsilon_0\epsilon_r) = eN_B dW/(\epsilon_0\epsilon_r)$. Therefore, the depletion capacitance is given by

$$C = \frac{dQ}{dU} = \frac{eN_B dW}{dU} = \frac{\epsilon_0\epsilon_r}{W}. \tag{2.3}$$

Inserting Eqn. (2.1) into Eqn. (2.3) results in the typical behavior of the C-V characteristics of an abrupt *pn* junction:

$$C(U) = \sqrt{\frac{e\epsilon_0\epsilon_r N_B}{2(U_{bi} - U)}} \tag{2.4}$$

Many circuit applications employ the voltage-variable capacitance properties of reverse biased *pn* diodes. A diode designed for such a purpose is called "varactor" which is the shortened form of variable reactor. For example, when a varactor is connected to an induction L in a resonant circuit, the resonant frequency varies with the voltage applied to the varactor:

$$\omega = \frac{1}{\sqrt{LC}} \propto U^{1/4} \tag{2.5}$$

2.2 C-V spectroscopy on QDs

C-V spectroscopy providing experimental capacitance-voltage characteristics is widely used to receive information about the spatial doping profile [Sze81] or band offsets [Ari00, Lu98]. The structure under investigation is therefore usually embedded in a *pn* or a Schottky diode. In this work, arrays of self-organized QDs are investigated. Structures with embedded self-organized Ge/Si [Kap00b, Mie00] or InAs/GaAs [Luy99, MR95, MR97b, MR97a, Bru99] QDs in Schottky- or tunnel-diodes have already been subject of intense experimental investigations. Here, C-V spectroscopy is used to find information about the electronic structure of InAs QDs in *pn* diodes as shown in Fig. 2.1. An array of QDs is positioned in the n^--doped region of a *pn* diode. If a reverse bias $U < 0$ is applied to the device, the depletion layer width rises. First, depletion of the bulk electron concentration arises. When the depletion layer reaches the QD layer, the local potential at the QDs changes, leading to an successively emptying of the electrons initially trapped in the QDs. The modification of the local potential by the charge located in the QDs leads to a variation of C-V characteristic of the depletion layer, containing information about the QDs. These complicated local modifications of the potential in the vicinity of the QDs cannot be estimated by simple expressions as for a bulk *pn* junction. More sophisticated models and numerical simulations are necessary.

3 Self-consistent models

The accurate theoretical description of the electronic QD levels in semiconductor devices is one top goal of research efforts. It is important for the interpretation of fundamental experiments such as the shot noise properties of Coulomb correlated QDs [Kie03a, Kie03b], as well as for the development of future applications involving QDs. The spatial potential distribution, the charge distribution, and the band structure determine the QD energy levels and therefore also the occupation of the QDs with carriers. For a limited number of devices, where the charge distribution in the vicinity of QDs is negligible, one may use simple estimations for the electrical potential, such as the so-called lever-arm method [MR97b, MR97a]. For example, if the QDs are embedded in a *p*-*i*-*n* structure, and neglecting the charge in the QDs themselves, the potential at the QDs is simply given by

$$\Phi(z_{\mathrm{QD}}) = \Phi_p - \mathcal{E}\frac{t}{d}, \tag{3.1}$$

where Φ_p is the potential at the *p*-contact, $\mathcal{E}$ is the constant electric field in the intrinsic, charge neutral region, d is the total width of the intrinsic region, and t is the distance of the QD layer from the highly doped *p*-contact. But for most device geometries such simple approaches must fail, and improved methods are necessary.

In this chapter two models are proposed which allow to calculate self-consistently the potential distribution in a semiconductor device containing a sheet of QDs. Special interest is turned to GaAs *pn* diodes as shown in Fig. 3.1 where a sheet of self-organized InAs QDs is positioned in an n^--doped region.

The one-dimensional sheet charge model [Wet00, Wet01b] approximates the charge stored in the QDs as a homogeneous charge per

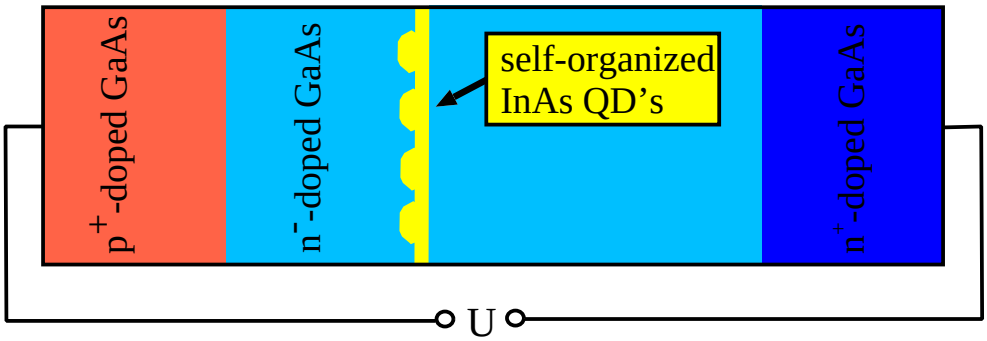

Figure 3.1: Layer sequence of the *pn* diode with an embedded array of self-organized InAs QDs

unit area, using the QD energy levels and their broadenings as parameters. It allows to find values for the QD energy levels and their broadenings by a fit of simulated C-V characteristics to experimental data.

The three-dimensional model [Wet03b] accounts for the inhomogeneous charge distribution in the QD layer and different QD ensembles can be simulated in order to investigate the role of fluctuations in position and size of the QDs. Charging effects are described in detail including the bulk charge distribution in the semiconductor matrix.

3.1 Sheet charge model

The sheet charge model is spatially one-dimensional in the vertical growth direction (z-axis). The spatial bulk charge density distribution per unit volume ρ in a *pn* device consists of the bulk electron density n, the bulk hole density p, the ionized donor N_{D}^{+} and acceptor concentration N_{A}^{-}. Therefore, ρ is expressed as

$$\rho(z) = e\left[p(z) - n(z) + N_{\mathrm{D}}^{+}(z) - N_{\mathrm{A}}^{-}(z)\right], \tag{3.2}$$

where $e > 0$ is the elementary charge.

Charge from electrons trapped in the QD layer is assumed to be homogeneously distributed in the lateral (x-y) directions. The

electron density per unit area in the QD layer is denoted by $\sigma_{\mathrm{n}}^{\mathrm{QD}}$. χ_{QD} shall be the characteristic function given by

$$\begin{aligned} \chi_{\mathrm{QD}}(z) &= 1/h \text{ for } z_{\mathrm{QD}} - h/2 < z < z_{\mathrm{QD}} + h/2 \\ \chi_{\mathrm{QD}}(z) &= 0 \text{ else,} \end{aligned} \tag{3.3}$$

where h is the height of the QDs and z_{QD} is the position of the QD layer, to account for the confinement in the vertical direction.

The charge densities will lead to an inhomogeneous potential distribution Φ which is given by the one-dimensional non-linear Poisson equation

$$\partial_z \left[\epsilon_r(z)\partial_z\Phi(z)\right]\epsilon_0 = -\rho(\Phi, E_{\mathrm{Fn}}, E_{\mathrm{Fp}}) - \sigma_{\mathrm{n}}^{\mathrm{QD}}\chi_{\mathrm{QD}}(z), \tag{3.4}$$

where ϵ_0 and ϵ_r are the absolute and relative permittivities, respectively. E_{Fn} and E_{Fp} are the quasi-Fermi levels of the electrons and the holes. Equation (3.4) is non-linear in Φ, i.e., ρ is a function of Φ, since density gradients and electric fields will lead to a current flow as described in the drift-diffusion model which is used in this work. Latter can be derived from a moment expansion of the Boltzmann equation to the first order, where the charge density is the moment of zero order, and the current is the moment of first order of the distribution function [Mar90, Sch98a]. For small electric fields, the bulk electron density can be expressed by the local potential and the electron quasi-Fermi level

$$n(z) = N_{\mathrm{c}}(z)\mathcal{F}_{1/2}\left(\beta\left[E_{\mathrm{Fn}}(z) - E_{\mathrm{c}}(z)\right]\right). \tag{3.5}$$

Here, β is given by $\beta = 1/(k_B T)$ with the Boltzmann constant k_B and the temperature T, E_{c} is the conduction band edge $E_{\mathrm{c}} = E_{\mathrm{c0}} - e\Phi$ and N_{c} is the effective density of states

$$N_{\mathrm{c}}(z) = 2\left(\frac{k_B T m_{\mathrm{n}}^*(z)}{2\pi\hbar^2}\right)^{3/2}, \tag{3.6}$$

where m_{n}^* is is the effective mass of the conduction band. E_{c0} denotes the intrinsic conduction band edge, including the gap between

the conduction and valence band edge. $\mathcal{F}_j(x)$ denotes the Fermi integral of order j defined by

$$\mathcal{F}_j(x) = \frac{1}{\Gamma(j+1)} \int_0^\infty du \frac{u^j}{1+\exp(u-x)}, \tag{3.7}$$

where Γ is the Gamma function ($\Gamma(3/2) = \sqrt{\pi}/2$). The hole density is given by the sum of the light and heavy hole densities $p = p_\mathrm{l} + p_\mathrm{h}$. Analogously to the electron density, p is given by

$$p(z) = N_\mathrm{v}(z) \mathcal{F}_{1/2}\left(\beta\left[E_\mathrm{v}(z) - E_\mathrm{Fp}(z)\right]\right), \tag{3.8}$$

with the valence band edge $E_\mathrm{v} = E_\mathrm{v0} - e\Phi$ and the effective density of states

$$N_\mathrm{v}(z) = 2\left(\frac{k_B T m_\mathrm{p}^*(z)}{2\pi\hbar^2}\right)^{3/2}. \tag{3.9}$$

The density of states effective hole mass is given by

$$m_\mathrm{p}^* = \left(m_\mathrm{l}^{*3/2} + m_\mathrm{h}^{*3/2}\right)^{2/3}, \tag{3.10}$$

with the light and heavy hole masses m_l^* and m_h^*. Under the usual assumption that all doping atoms are singly ionized, the concentration of the ionized donor and acceptor atoms can be approximated by the doping concentration. In the steady state, the electron and hole drift-diffusion current densities are given by [Mar86]

$$\begin{aligned} j_\mathrm{n}(z) &= \mu_\mathrm{n}(z) n(z) \partial_z E_\mathrm{Fn}(z) \\ j_\mathrm{p}(z) &= \mu_\mathrm{p}(z) p(z) \partial_z E_\mathrm{Fp}(z), \end{aligned} \tag{3.11}$$

with the electron and hole mobilities μ_n and μ_p, respectively. Neglecting generation and recombination in the active region, the continuity equations

$$\begin{aligned} \partial_z j_\mathrm{n}(z) &= 0 \\ \partial_z j_\mathrm{p}(z) &= 0 \end{aligned} \tag{3.12}$$

hold.

To find an expression for the QD electron density, discrete QD energy levels $E_j < 0$, measured from the conduction band edge with a degeneracy α_j are used. These levels are inhomogeneously broadened mainly due to QD size fluctuations with a full width at half maximum ΔE_j. E_j can therefore be conceived as an average QD level energy of the ensemble. In steady state, where transition rates from each Fermi distributed $\boldsymbol{k}$-state in the conduction band into the QD state j and the respective reverse rates balance, the QD electrons are in quasi-equilibrium with the conduction band leading to a Fermi occupation of the QD states. With the QD sheet density N_{QD} the QD electron density per unit area can be expresses as

$$\sigma_{\mathrm{n}}^{\mathrm{QD}} = N_{\mathrm{QD}} \sum_j \frac{\alpha_j}{\sigma_j \sqrt{2\pi}} \int_{-\infty}^{\infty} dE \frac{\exp\left(-\frac{[E-E_{\mathrm{c}}(z_{\mathrm{QD}})-E_j]^2}{2\sigma_j^2}\right)}{1+\exp\left(\beta[E-E_{\mathrm{Fn}}(z_{\mathrm{QD}})]\right)}, \quad (3.13)$$

with $\sigma_j = \Delta E_j / \sqrt{8 \ln 2}$.

In this work, also a device where only a quantum well (QW) structure has been grown instead of the QD array will be considered. To describe the charge density for such a device, $\sigma_{\mathrm{n}}^{\mathrm{QD}}$ has to be replaced by the quantum well sheet charge density $\sigma_{\mathrm{n}}^{\mathrm{QW}}$ given by [And82]

$$\sigma_{\mathrm{n}}^{\mathrm{QW}} = \frac{m^* k_B T}{\pi \hbar^2} \ln\left(1+\exp\left(\frac{E_{\mathrm{Fn}}(z_{\mathrm{QD}}) - [E_{\mathrm{c}}(z_{\mathrm{QD}}) + E_{\mathrm{QW}}]}{k_B T}\right)\right). \quad (3.14)$$

Here, $E_{\mathrm{QW}} < 0$ denotes the quantization energy of the one-dimensionally confined electrons measured from the conduction band edge.

The Poisson equation (3.4) and the continuity equations (3.12) define a self-consistent problem with the variables Φ, E_{Fn} and E_{Fp} [Sel84]. The highly doped Ohmic contacts provide boundary conditions for the potential and the quasi-Fermi levels. Vanishing space charge density ρ at the boundaries is assumed to hold for Ohmic contacts [Rid74], i.e., the electron density equals the donor concentration N_D^+ in the n-contact, and the hole density equals the

acceptor concentration N_A^- in the p-contact. In equilibrium, where $E_{\mathrm{Fn}} = E_{\mathrm{Fp}} = E_{\mathrm{F}}$, with the Fermi level E_{F} and choosing E_{F}=0 this leads to values for the equilibrium potential in the left and right contact, Φ_L^{eq} and Φ_R^{eq}, respectively. In order to hold $\rho = 0$ for all bias conditions, a bias U is applied by choosing the boundary values as

$$\begin{aligned} E_{\mathrm{Fn,L}} = E_{\mathrm{F}} + eU/2 \;\; E_{\mathrm{Fp,L}} = E_F + eU/2 \;\; \Phi_{\mathrm{L}} = \Phi_{\mathrm{L}}^{\mathrm{eq}} - U/2 \\ E_{\mathrm{Fn,R}} = E_{\mathrm{F}} - eU/2 \;\; E_{\mathrm{Fp,R}} = E_{\mathrm{F}} - eU/2 \;\; \Phi_{\mathrm{R}} = \Phi_{\mathrm{R}}^{\mathrm{eq}} + U/2, \end{aligned} \tag{3.15}$$

where $E_{\mathrm{Fn,L}}$, $E_{\mathrm{Fn,R}}$, $E_{\mathrm{Fp,L}}$, $E_{\mathrm{Fp,R}}$, Φ_{L}, and Φ_{R} are the boundary values for the quasi-Fermi levels and the potential.

According to the definition (2.2) the simulated depletion layer capacitance is given by the self-consistent electric field in the depletion layer

$$C = \epsilon_0 \epsilon_r \left| \frac{d\left[\partial_z \Phi(z_{\mathrm{DL}})\right]}{dU} \right|, \tag{3.16}$$

where z_{DL} is a fixed position in the depletion layer.

3.2 Three-dimensional model

In this section a much more detailed model is proposed which in comparison to the sheet charge model includes the charge inhomogeneity in the QD layer. The aim is to derive a description for the Coulomb interaction including all charges, i.e., bulk charge and charges from electrons in the QD. Each level in each single QD is treated as a state which can be occupied by an electron. Since only a small but essential part of the structure is not translational invariant in the lateral (x,y) directions, but most of the device is inhomogeneous only in the vertical growth direction (z) the electrostatic potential is divided up into three parts for practical reasons. To obtain the QD charging energies, the capacitance matrix of a QD ensemble is calculated which, in contrast to other models [Wha96], includes the spatial charge distribution within a device.

The spatial potential distribution in a device is described by the three-dimensional Poisson equation

$$\nabla \left[\epsilon_r(z)\epsilon_0 \nabla \Phi^{\mathrm{3D}}(\boldsymbol{r})\right] = -\rho^{\mathrm{tot}}(\boldsymbol{r}), \tag{3.17}$$

where Φ^{3D} is the three-dimensional potential distribution and ρ^{tot} is the self-consistent total charge distribution in the device including bulk and QD charges. The idea is to perform a linear Taylor expansion around the solution Φ^{1D} of the one-dimensional Poisson equation

$$\partial_z \left[\epsilon_r(z)\epsilon_0 \partial_z \Phi^{\mathrm{1D}}(z)\right] = -\rho(z) - \chi(z)\sigma_{\mathrm{n}}^{\mathrm{QD}}, \tag{3.18}$$

where the QD charge has been approximated as a sheet charge $\sigma_{\mathrm{n}}^{\mathrm{QD}}$ averaged over the cross section area A of the sample

$$\sigma_{\mathrm{n}}^{\mathrm{QD}} = \frac{-e}{A} \sum_{\alpha\mu} p_{\alpha\mu}. \tag{3.19}$$

Here, $p_{\alpha\mu}$ denotes the integer occupation numbers of the level μ in the QD labeled with α ($p_{\alpha\mu} = 0$ if state $\alpha\mu$ is not occupied, $p_{\alpha\mu} = 1$ if state $\alpha\mu$ is occupied). ρ is the one-dimensional bulk charge distribution as obtained from a self-consistent solution with the current equations as in the previous section. Approximating the QD charge as a three-dimensional perturbation, a Taylor expansion in the bulk charge density now leads to

$$\nabla \left[\epsilon_r(z)\epsilon_0 \nabla \Phi^{\mathrm{3D}}(\boldsymbol{r})\right] = -\rho(z) - \frac{\partial \rho(z)}{\partial \Phi}\left[\Phi^{\mathrm{3D}}(\boldsymbol{r}) - \Phi^{\mathrm{1D}}(z)\right] - \rho_{\mathrm{n}}^{\mathrm{QD}}(\boldsymbol{r}), \tag{3.20}$$

where $\rho_{\mathrm{n}}^{\mathrm{QD}}$ is the three-dimensional QD charge distribution. Due to the linearity of the Poisson equation, Φ^{3D} can be written as a sum of the one-dimensional potentials Φ^{1D} and $\hat{\Phi}^{\mathrm{1D}}$, with

$$\partial_z \left[\epsilon_r(z)\epsilon_0 \partial_z \hat{\Phi}^{\mathrm{1D}}(z)\right] = \chi(z)\sigma_{\mathrm{n}}^{\mathrm{QD}} - \frac{\partial \rho(z)}{\partial \Phi}\hat{\Phi}^{\mathrm{1D}}(z) \tag{3.21}$$

and the three-dimensional part Φ^{QQ}, with

$$\nabla \left[\epsilon_r(z)\epsilon_0 \nabla \Phi^{\mathrm{QQ}}(\boldsymbol{r})\right] = -\rho_{\mathrm{n}}^{\mathrm{QD}}(\boldsymbol{r}) - \frac{\partial \rho(z)}{\partial \Phi}\Phi^{\mathrm{QQ}}(\boldsymbol{r}), \tag{3.22}$$

as

$$\Phi^{3D}(\boldsymbol{r}) = \Phi^{1D}(z) + \hat{\Phi}^{1D}(z) + \Phi^{QQ}(\boldsymbol{r}) \tag{3.23}$$

Note that $\Phi^{BQ} = \hat{\Phi}^{1D} + \Phi^{1D}$ can be conceived as a background potential for a single QD electron, excluding all other QD charges. Equation 3.22 can be solved by a Green's function technique. The respective Poisson equation for the Green's function reads as

$$\begin{aligned} \partial_z \left[\ln(\epsilon_r(z))\partial_z G(z, r_{\shortparallel}, z')\right] + \Delta_{\boldsymbol{r}_{\shortparallel}} G(z, r, z') = \\ -\frac{\delta((0, z') - (\boldsymbol{r}_{\shortparallel}, z))}{\epsilon_r(z)\epsilon_0} - \frac{\lambda_{3D}^2(z)}{e^2} G(z, r, z'). \end{aligned} \tag{3.24}$$

where $\Delta_{\boldsymbol{r}_{\shortparallel}}$ is the two-dimensional Laplace operator, $r_{\shortparallel} = |\boldsymbol{r}_{\shortparallel}|$ is the radial distance in the lateral plane and λ_{3D} is the static Debye screening wave length [Lan91]

$$\lambda_{3D}(z) = \sqrt{\frac{e^2}{\epsilon_0 \epsilon_r(z)} \frac{\partial \rho(z)}{\partial \Phi^{1D}}}. \tag{3.25}$$

Note that G has a cylinder symmetry, since λ_{3D} and ϵ_r depend only on z.

The QD charging energies, i.e., the values of the three-dimensional potential at the QDs, are of interest for a self-consistent solution, since they determine the level energies and therefore the occupation of the QDs with electrons. The QD level μ is represented by $\mu = (n_x, n_y, n_z)$ with the quantum numbers n_x, n_y and n_z. Here, the intrinsic quantization energy of electronic QD states $E_{\alpha\mu}^{\text{intr}} < 0$ is measured from the background conduction band edge $E_{c0}(z_{QD}) - e\Phi^{BQ}(z_{QD})$. $E_{\alpha\mu}^{\text{intr}}$ is a material parameter. Throughout this work fitted results of $\boldsymbol{k} \cdot \boldsymbol{p}$ calculations [Sti99] are used to account specifically for the size dependence of $E_{\alpha\mu}^{\text{intr}}$ of InAs QDs as shown in Fig. 3.2.

Treating the charging energies $E_{\alpha\mu}^{\text{char}}$ as a first order perturbation, the total QD electron energy can be expressed as

$$E_{\alpha\mu}^{QD} = E_{c0}(z_{QD}) - e\Phi^{BQ}(z_{QD}) + E_{\alpha\mu}^{\text{intr}} + E_{\alpha\mu}^{\text{char}}. \tag{3.26}$$

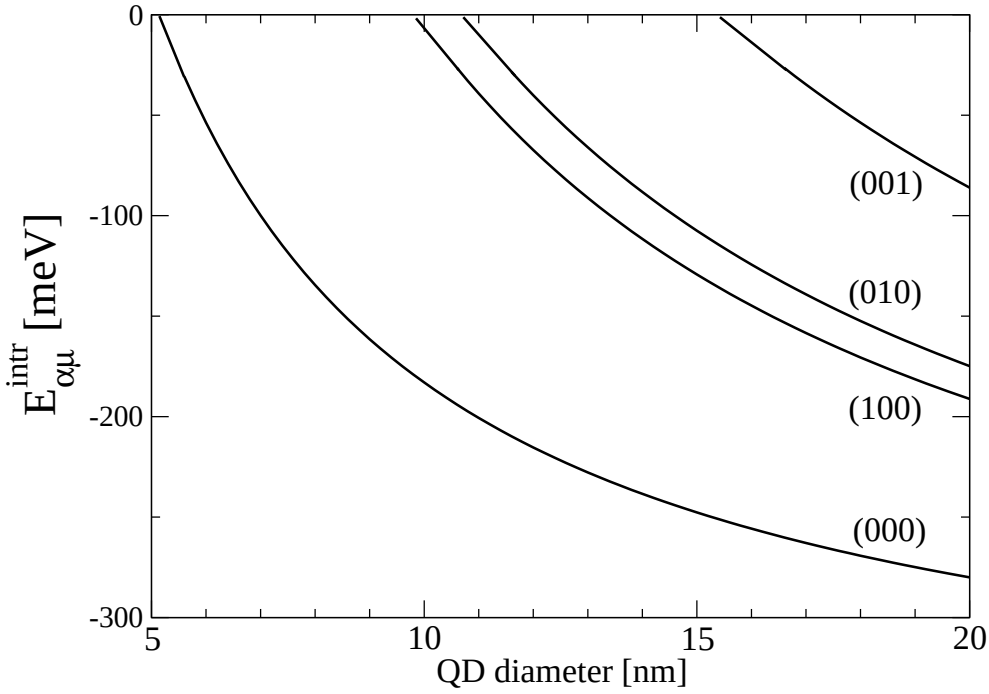

Figure 3.2: Size dependence of the electron level energies $E^{\text{intr}}_{\alpha\mu}$ for μ=(000), (100), and (010) according to a fit to $\boldsymbol{k}\cdot\boldsymbol{p}$ calculations [Sti99] for a single QD

The level charging energy is obtained by a summation over all occupied QD levels

$$E^{\text{char}}_{\alpha\mu} = e^2 \sum_{\beta\nu} p_{\beta\nu} \left(C^{-1}\right)_{\alpha\beta} \left[1 - \delta_{\alpha\mu,\beta\nu}\right], \tag{3.27}$$

where $\delta_{\alpha\mu,\beta\nu}$ ensures that an elementary charge does not interact with itself. C is the capacitance matrix of the QD ensemble. The elements of the inverse capacitance matrix is calculated by using the Green's function

$$\left(C^{-1}\right)^{\mu\nu}_{\alpha\beta} = \int\int |\psi_{\alpha\mu}(\boldsymbol{r})|^2 \, G(\boldsymbol{r},\boldsymbol{r}') \, |\psi_{\beta\nu}(\boldsymbol{r})|^2 \, d^3\boldsymbol{r}' d^3\boldsymbol{r}, \tag{3.28}$$

with the QD wave functions $\psi_{\alpha\mu}$ and $\psi_{\beta\nu}$ [War98]. For well confined QD electrons, the electrons are assumed to be homogeneously distributed over the QD volumes V_α and V_β, neglecting further details of the wave functions. Then C^{-1} has only indices of the QD labels,

leading to

$$\left(C^{-1}\right)_{\alpha\beta} = \frac{1}{V_\alpha V_\beta} \int\limits_{V_\alpha} \int\limits_{V_\beta} G(\boldsymbol{r}, \boldsymbol{r}') d^3\boldsymbol{r}' d^3\boldsymbol{r}. \tag{3.29}$$

To determine the stationary occupation of the QD layer with electrons, each level is occupied statistically according to the occupation probability $f_{\alpha\mu}$, in order to account for the statistical character of the microscopic in and out scattering processes in QDs [Gru97]. $f_{\alpha\mu}$ is a function of the local quasi-Fermi level and the QD level energies which can be derived from detailed balance consideration between a QD level and the continuum electrons of the conduction band. In thermodynamic equilibrium, emission and capture rates have to "balance in detail", i.e., the scattering rates from each microscopic continuum state $\boldsymbol{k}$ to a QD level have to be equal to the scattering probability of the respective reverse process, thus

$$W_{k,\alpha\mu} f_k^{\mathrm{eq}} \left[1 - f_{\alpha\mu}^{\mathrm{eq}}\right] = W_{\alpha\mu,k} f_{\alpha\mu}^{\mathrm{eq}} \left[1 - f_k^{\mathrm{eq}}\right] \tag{3.30}$$

must hold, where f_k^{eq} and $f^{\mathrm{eq}_{\alpha\mu}}$ denote the occupation probabilities of a continuum $\boldsymbol{k}$-state and the QD level, respectively, and $W_{k,\alpha\mu}$ and $W_{\alpha\mu,k}$ denote the transition probabilities from state $\mathbf{k}$ into the QD state $\alpha\mu$ and vice versa. In the case of equilibrium the occupation probabilities are given by the Fermi distribution functions

$$f_k^{\mathrm{eq}} = \frac{1}{1 + \exp\left(\beta \left[E_k - E_{\mathrm{F}}\right]\right)} \tag{3.31}$$

and

$$f_{\alpha\mu}^{\mathrm{eq}} = \frac{1}{1 + \exp\left(\beta \left[E_{\alpha\mu}^{QD} - E_{\mathrm{F}}\right]\right)}. \tag{3.32}$$

Inserting Eqn. (3.31) and (3.32) into (3.30) leads to

$$W_{\alpha\mu,k} = W_{k,\alpha\mu} \exp\left(\beta \left[E_{\alpha\mu}^{QD} - E_k\right]\right). \tag{3.33}$$

Assuming that the latter relation holds under all bias conditions leads to the stationary non-equilibrium occupation probability of

the QD level

$$f_{\alpha\mu} = \frac{1}{1 + \exp\left(\beta\left[E_{\alpha\mu}^{QD} - E_{\mathrm{Fn}}(z_{\mathrm{QD}})\right]\right)}. \tag{3.34}$$

Since only a finite cross-section area A can be simulated, containing typically a hundred QDs which is smaller than typical cross section areas in experiments with millions of QDs, appropriate boundary conditions have to be chosen in the lateral directions. Here, periodic boundary conditions as obtained from a charge distribution outside A as shown in Fig. 3.3 are used. The cross section area A with its QD charge distribution is surrounded by eight identical areas with identical QD charge distributions. It is necessary that the typical screening length, i.e., the extension of the Green's function in lateral directions, is shorter than the base length of the quadratic area A to avoid artificial double-counting.

In conclusion, the self-consistent, non-linear problem of calculating the QD energy levels with respect to the three-dimensional potential distribution has now been reduced to:

- finding the self-consistent, one-dimensional solution Φ^{1D}, E_{Fn} and E_{Fp} of the Poisson equation and the current equations for a given $\sigma_{\mathrm{n}}^{\mathrm{QD}}$
- solving the two-dimensional Poisson equation in order to find the Green's function
- calculation of the inverse capacitance matrix
- statistical realization of a new QD occupation configuration to find the QD sheet charge σ_{n}^{QD} by changing the occupation of a single QD state by one electron
- start from the beginning with the new $\sigma_{\mathrm{n}}^{\mathrm{QD}}$

Note that the occupation of the QD levels according to (3.34) is coterminous to the stationary solution of a respective Master-equation [vK81].

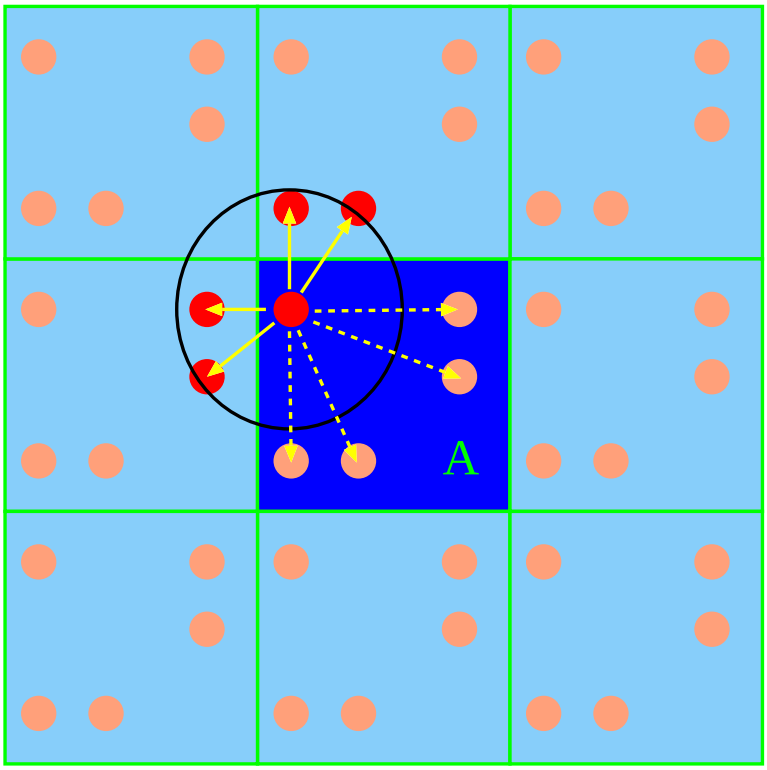

Figure 3.3: Sketch of the QD layer with one center cross-section area A and the eight cross-sections which hold the periodic boundary conditions: relevant Coulomb interaction (solid yellow arrows) occurs only within the typical screening length (black circle)

Because λ_{3D} depends on σ^{QD}, the capacitance matrix is changed whenever the occupation of a single QD state changes. Therefore, the iteration scheme is still very time consuming. In the following context this three-dimensional model is referred to as model A.

For small QD surface charges one may neglect the dependence of the screening length and therefore the capacitance matrix on the QD occupation (model B, [Wet03b]). Then the iteration scheme reduces to:

- finding the self-consistent, one-dimensional solution Φ^{1D}, E_{Fn} and E_{Fp} of the Poisson equation and the current equations for $\sigma_n^{QD} = 0$

- solving the two-dimensional Poisson equation in order to find the Green's function
- calculation of the inverse capacitance matrix
- statistical realization of QD occupation configurations to find the average QD sheet charge σ_{n}^{QD}
- finding the self-consistent, one-dimensional solution Φ^{1D}, E_{Fn} and E_{Fp} of the Poisson equation and the current equations for $\sigma_{\mathrm{n}}^{\mathrm{QD}}$

Now three different self-consistent models are available, one one-dimensional and two versions of a three-dimensional model, to simulate the charge distribution in QD devices.

Analogously to the one-dimensional model (see Eqn. (3.16)), the depletion layer capacitance is given by the bias dependence of the vertical electric field in the depletion layer

$$C = \epsilon_0 \epsilon_r \left| \frac{d\left[\partial_z \Phi^{\mathrm{1D}}(z_{\mathrm{DL}})\right]}{dU} \right| . \tag{3.35}$$

4 Energy level analysis

Many groups have investigated QDs by optical techniques such as photoluminescence spectroscopy (PL) (see Ref. [Bim99] and references therein), providing information on the transition between strongly correlated excitonic levels. The study of single levels, e.g., in electrostatically defined QDs [Ash92] or self-organized QDs [Dre94, Kap99, Bro98] can only be accomplished by electrical methods like C-V spectroscopy. Here, a *pn* diode as displayed in Fig. 4.1 considered. A triple stack of InAs QDs was grown in the Stranski-Krastanov mode within the n^--doped GaAs layer [Kap98, Kap99]. Since the barriers between the QDs are only about 0.8 nm thin, the stacked QDs with a total height of h=9.1 nm behave like a single QD. This is also manifested by the shape of QD wave functions as obtained from $\boldsymbol{k} \cdot \boldsymbol{p}$ calculations. The QD sheet density is N_{QD}=10^{10} cm^{-2} as has been obtained from top view transmission electron microscopy (TEM), and circular mesas with a radius of 400 μm were defined by chemical etching. A wetting layer (WL) device containing the triple quantum well (QW) or wetting-layer (WL) structure, and reference device were grown under identical conditions. C-V characteristics have been measured for all three structures at T=75 K and an AC measurement frequency of f=1 kHz using an amplitude of 100 mV [Wet00, Wet01a].

The temperature is chosen such that on one hand thermal broadening effects are kept as small as possible, and on the other hand to avoid dynamical effects, i.e., all QD electrons can follow the frequency which has been chosen as small as possible. If the QD electrons have to overcome an energy barrier of ΔE to leave the QD into the conduction band continuum, the emission rate strongly depends on the temperature. The minimum temperature to measure a sta-

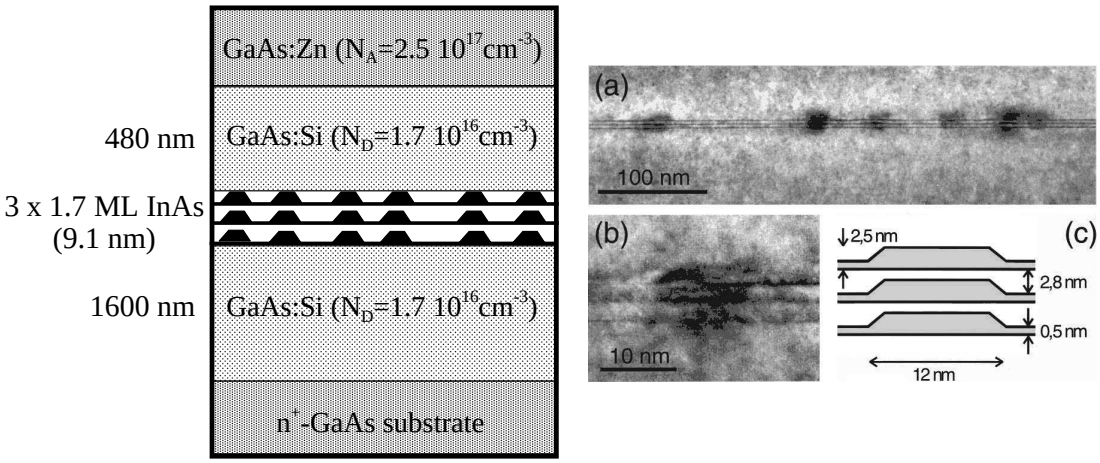

Figure 4.1: Left: layer sequence of the *pn* diode with embedded quantum dots; Right: (a) cross-section TEM image of the QD layer, (b) close-up of a single QD stack, (c) approximate geometry [Kap99]

tionary C-V characteristics can be estimated by a detailed balance consideration (see chapter 3.2) as

$$T = \frac{\Delta E}{k_B \ln(f/c)}, \tag{4.1}$$

where c is the capture rate. For c=1 ps^{-1}, a minimum temperature of 58 K for ΔE=100 meV is estimated. Typically, ΔE is equal to the QD level energy below the conduction band edge, or the QD energy level spacing to an excited QD state from which electron can leave the QD very fast, e.g., by a tunneling process. The temperature dependence of the emission process is for example used in dynamical capacitance measurements or deep level transient spectroscopy (DLTS) to find values for the energy levels of the QD states [Kap99].

4.1 Reference device

The experimental C-V curve of the reference device is displayed in Fig. 4.2 (black symbols). Over all it shows the typical behavior of

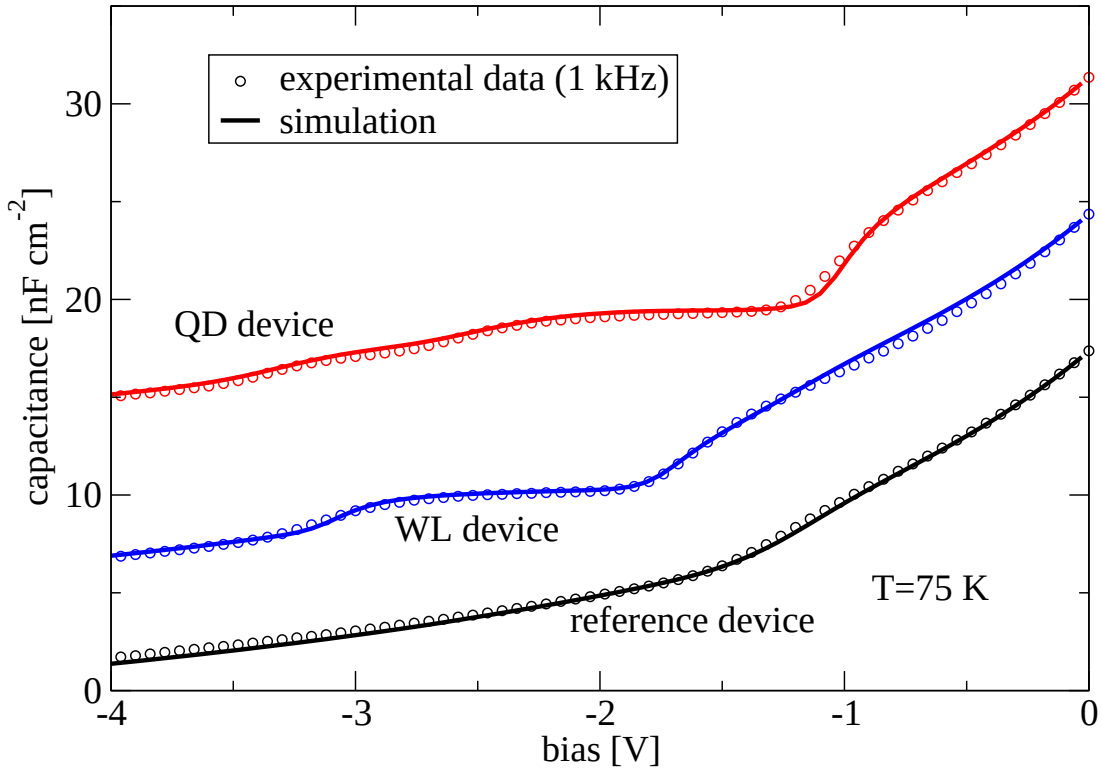

Figure 4.2: Symbols: experimental C-V characteristics for the sample of Fig. 4.1; Lines: simulated C-V curves for a QD device (red), WL device (blue) and a reference device (black); graphs of the WL and reference device are offset by -7 nFcm^{-2} and -14 nFcm^{-2}, respectively. Experimental data by courtesy of Christian Kapteyn, (TU Berlin) [Wet00, Wet01a]

the depletion layer capacitance of a *pn* diode except a little kink around U=-1.5 V. Numerical simulations of this structure and a fit to the experimental data, where the doping densities of the n^--doped buffer layers are used as fit parameters, are performed. The resulting curve is shown in Fig. 4.2 as a solid black line. A doping density of N_D=1.7×10^{16}cm^{-3} is found except in a 70 nm layer above the region where the QDs would have grown. Here, the doping density is reduced by 75 %. This reduced doping can be explained by the fact that the growth temperature is temporarily reduced when the QDs are grown, and that the identical temporal temperature

profile has been used for the reference and the WL sample. It is well known that the diffusion of doping atoms is reduced with lower temperature. Also further investigations of similar devices with this model have shown the impact of the diffusion of doping atoms during the growth process [Rac02a]. The following simulations of the WL and QD device include this reduction of the concentration of donor atoms above the WL and QD layer.

4.2 Wetting layer device

The WL device is considered next. The experimental C-V characteristic is shown in Fig. 4.2 as blue symbols. In contrast to the reference device it exhibits a flat plateau between U=-1.8 V and U=-3.0 V. The change of capacitance in this bias region originates from charge in the WL region. It has been shown analytically [Wan96] that a two-dimensional electron gas results in a constant capacitance in the bias region, where a quantum well is discharged as a direct consequence of the constant density of states [Moo98, Bro94, Bro96]. Here, the simulated C-V characteristics is fit to the experimental data (blue solid line in Fig.4.2), using the WL energy E_{QW} as the fit parameter. This fit leads to a WL quantization energy for the triple WL structure of E_{QW}=-55 meV. Note that for a single WL structure higher values, i.e., binding energies closer to the conduction band edge are expected [Sti99].

4.3 Quantum dot device

Figure 4.2 shows the experimental C-V characteristic for the QD device for T=75 K (red symbols). It exhibits the typical depletion layer behavior, modified by two plateaus in the bias region -3.6 V $\leq$ U $\leq$ -0.8 V which can be attributed to the emptying of the QD levels. In order to analyze the experimental data, the level energies E_0 and E_1 of the ground and excited state and the respective level broadenings ΔE_0 and ΔE_1 are used as fit parameters in the sheet

charge model. Degeneracy factors including the spin of α_0=2 for the ground state (000), and α_1=6 for the excited levels consisting of the states (100), (010) and (001) are used. This degeneracy corresponds to the nearly cubic symmetry of the triple-stacked QDs, and has also been shown by the 8-band $\boldsymbol{k} \cdot \boldsymbol{p}$ calculations. A fit (Fig. 4.2, solid red line) to the experimental data leads to the values E_0=-211 meV, E_1=-128 meV, ΔE_0=141 meV and ΔE_1=95 meV. A variation of the parameters corroborates an accuracy of the results of about 10 meV [Wet00].

This structure has also been investigated by deep-level-transient-spectroscopy (DLTS) and 8-band $\boldsymbol{k} \cdot \boldsymbol{p}$ calculations [Kap99, Kap98]. The DLTS measurements resulted in a separation of the (000) state and the excited states of 94 meV which is only 11 meV less than obtained here. Also the $\boldsymbol{k} \cdot \boldsymbol{p}$ calculations (E_0=-195 meV, $E_{1,2}$=-115 meV, E_3=-111 meV) result in only slightly smaller energies with about the same separation.

The ground state broadening is also in good agreement with the broadening of the photoluminescence peak for this structure [Kap99] (both about 150 meV). But the results also indicate that the broadening of the ground state is larger than that of the excited states. This is in contrast to the size dependence of the QD energies as found by $\boldsymbol{k} \cdot \boldsymbol{p}$ theory, where the excited states have been found to be more sensitive to size fluctuations.

So far, the one-dimensional model has allowed to find values for the QD level energies and their broadenings, by simulating the charge distribution in the vicinity of the QDs. Over all, this method seems to be suitable to measure the QD level energies by C-V spectroscopy. However, these findings also indicate the possibility of an over-simplification of Coulomb charging effects especially for the excited states in the QD array and emphasize the need to account for the truly three-dimensional nature of the QD layer.

5 Charging effects

In this chapter the true three-dimensional character of arrays of self-organized QDs is taken into account in the simulations [Wet03b]. With the three-dimensional models proposed in chapter 3 different ensembles of QDs and their C-V characteristics can be simulated. In the present chapter, the detailed Coulomb charging effects in arrays of QDs are investigated. Structural fluctuations are neglected. The QDs are of the same size and are periodically ordered.

5.1 C-V characteristic

A *pn* diode similar to the structure proposed in chapter 4 is considered, with a QD sheet density of $N_{QD} = 10^{10}$ cm^{-2}, a n^--doping of 3×10^{16} cm^{-3} in the surrounding semiconductor matrix, a QD diameter of 15 nm, and a QD height of 3 nm. The distance of the QD layer to the *pn* interface is 400 nm. Arrays of 10×10 QDs are simulated. Size or position fluctuations are neglected, thus all QDs have the same size and are periodically ordered. The calculations are performed for T=70 K.

In Fig. 5.1 the simulated C-V characteristic of the diode, as well as the mean number of electrons per QD, and the differential QD sheet charge (QD capacitance) $d\sigma_{QD}/dU$ are plotted.

First, the results as obtained from model B which neglects the dependence of the capacitance matrix on the QD sheet charge density which is a good approximation for low QD sheet charge densities are discussed. At zero bias the QDs are filled with six electrons each. Applying a reverse bias and enlarging the depletion layer width of the diode reduces the QD occupation to five, four, three, two, one and zero electrons per QD. Each change in the QD occupation leads

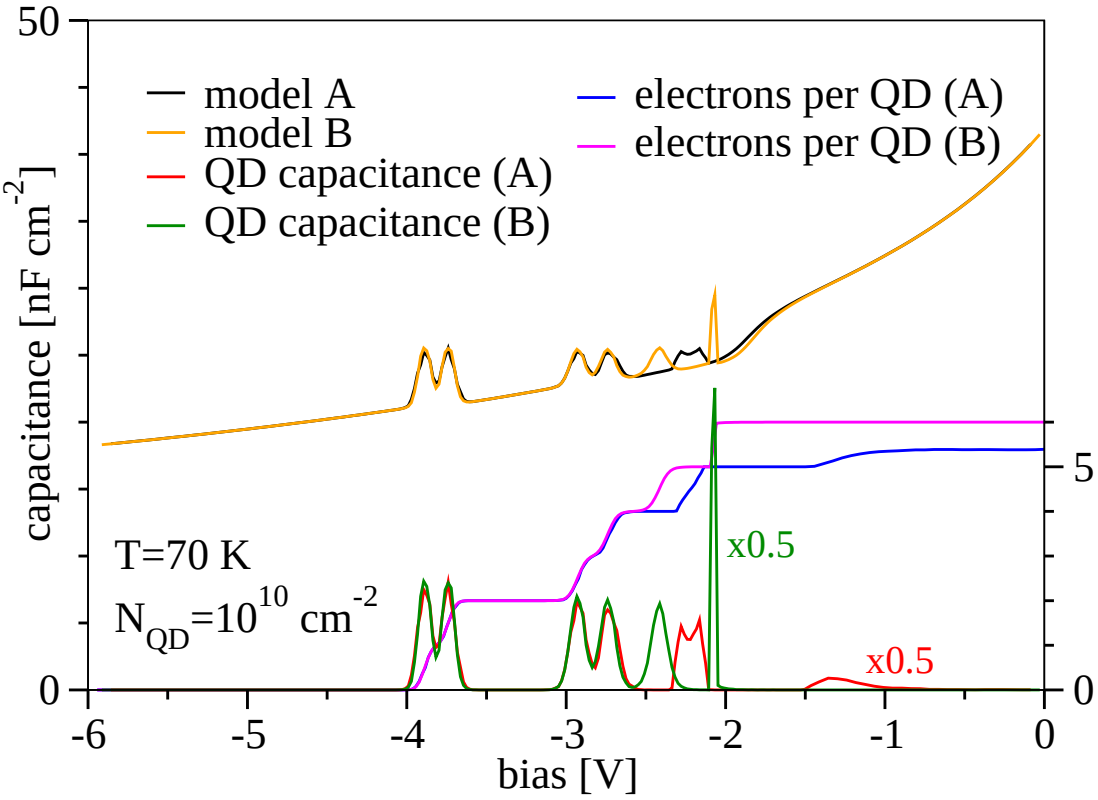

Figure 5.1: the depletion layer capacitance-voltage characteristics of a *pn* diode with N_{QD}=10^{10} cm^{-2} at T=70 K (model A: black line; model B: orange line), the corresponding QD capacitance (model A: red line; model B: green line) and the mean number of electrons per QD as a function of the bias (model A: blue line; model B: magenta line)

to a corresponding peak in the C-V characteristic. The peaks can be attributed - with increasing reverse bias - to the spin degenerate QD states (010), (100) and (000). Clearly a splitting of the spin degenerate states by Coulomb charging effects, i.e., the repulsion of two electrons in the same QD, and a broadening of the peaks can be observed. The broadening of the first peak is strongly reduced.

Model A which includes the QD sheet density dependence of the capacitance matrix results mainly in the same C-V characteristic, but it shows a clear deviation from model B for a QD occupation larger than four electrons in each QD which reflects exactly the addi-

tional approximation made for model B. The QDs are occupied with less than six electron at zero bias since the occupation dependent Coulomb repulsion strength in model A is larger than in model B, since the Coulomb repulsion between the QD sheet charge and the screening bulk electrons is neglected in model B. Additionally, the peak at U=-2.1 V is broadened and shifted to a lower reverse bias, compared to model B.

As can be observed in Fig. 5.1, the total depletion layer capacitance is not just given by the sum of a background depletion layer capacitance and the QD capacitance, but the QD capacitance shows the identical peak shape as observed in the total capacitance. Typically, the QD capacitance is much larger than the contribution of the QDs to the total capacitance.

To obtain a deeper understanding of the mechanisms determining the Coulomb charging effects and broadening mechanisms, a closer look at the electronic details of the device is necessary.

5.2 Screening

For biases U=0.0 V, -2.0 V and -4.0 V Fig. 5.2 shows the bulk electron and hole densities as well as the QD electron volume density $-\sigma_{QD}/(eh)$ as a function of the vertical position (left column) and the corresponding Green's function $G(z, z_{QD}, r)$ as a contour plot (right column) for the calculations made with model A. The Green's function has been normalized to the unscreened Green's function (λ_{3D}=0) for more clarity. With rising reverse bias not only the QDs are emptied, but also the bulk electron density surrounding the QDs is more and more depleted. At zero bias, the QDs are fully embedded within a spatial bulk electron density distribution. The Green's function which represents the potential of a point-like unit charge is therefore strongly screened. With the depletion of the bulk electrons with rising reverse bias the Green's function starts to extend in vertical and lateral directions within the depletion layer. The shape of the Green's function determines

the Coulomb repulsion between electrons trapped in neighbor QDs and electrons within the same QD. From the shape of the Green's function and considering the QD-QD distance of 100 nm one can already estimate that at U=0.0 V Coulomb repulsion should be smaller than for U=-4.0 V, where especially Coulomb interaction between QDs will play an important role.

5.3 Charging energies

Since the Green's function changes its shape with the applied bias, the charging energies will also be bias dependent. Holding the QD charge fixed at one electron per QD, the matrix elements of the inverse capacitance matrix contain the charging energies between the electrons in the QD layer. Figure 5.3 shows the matrix elements for U=0.0 V, -2.0 V, -3.0 V and -4.0 V. The diagonal matrix elements, i.e., the charging energy resulting from the repulsion of two electrons in the same QD, hardly depend on the bias. With rising reverse bias and reduced screening effects, the strength of Coulomb interaction between neighboring QDs rises. For this particular structure a charging energy between nearest neighbor QDs of up to the order of 1 meV is obtained.

But an electron confined at a QD "sees" the sum of all other electrons in the QD layer, and therefore the total charging energies are of special interest. It is useful to distinguish between the intra-QD charging energy resulting from mean value of the diagonal elements of the inverse capacitance matrix, and the inter-QD charging energy as resulting from the mean value of the sum of all non-diagonal elements of a row (or a column due to symmetry) of the inverse capacitance matrix. In other words, the occupation is kept fixed at one electron per QD. Figure 5.3 displays the intra-QD and inter-QD charging energy as a function of the bias for both model A and B. The intra-QD charging energy is reduced due to screening at U=0.0 V where it is almost bias independent and then changes rather rapidly at U=-2.0 V from a value of about 17 meV

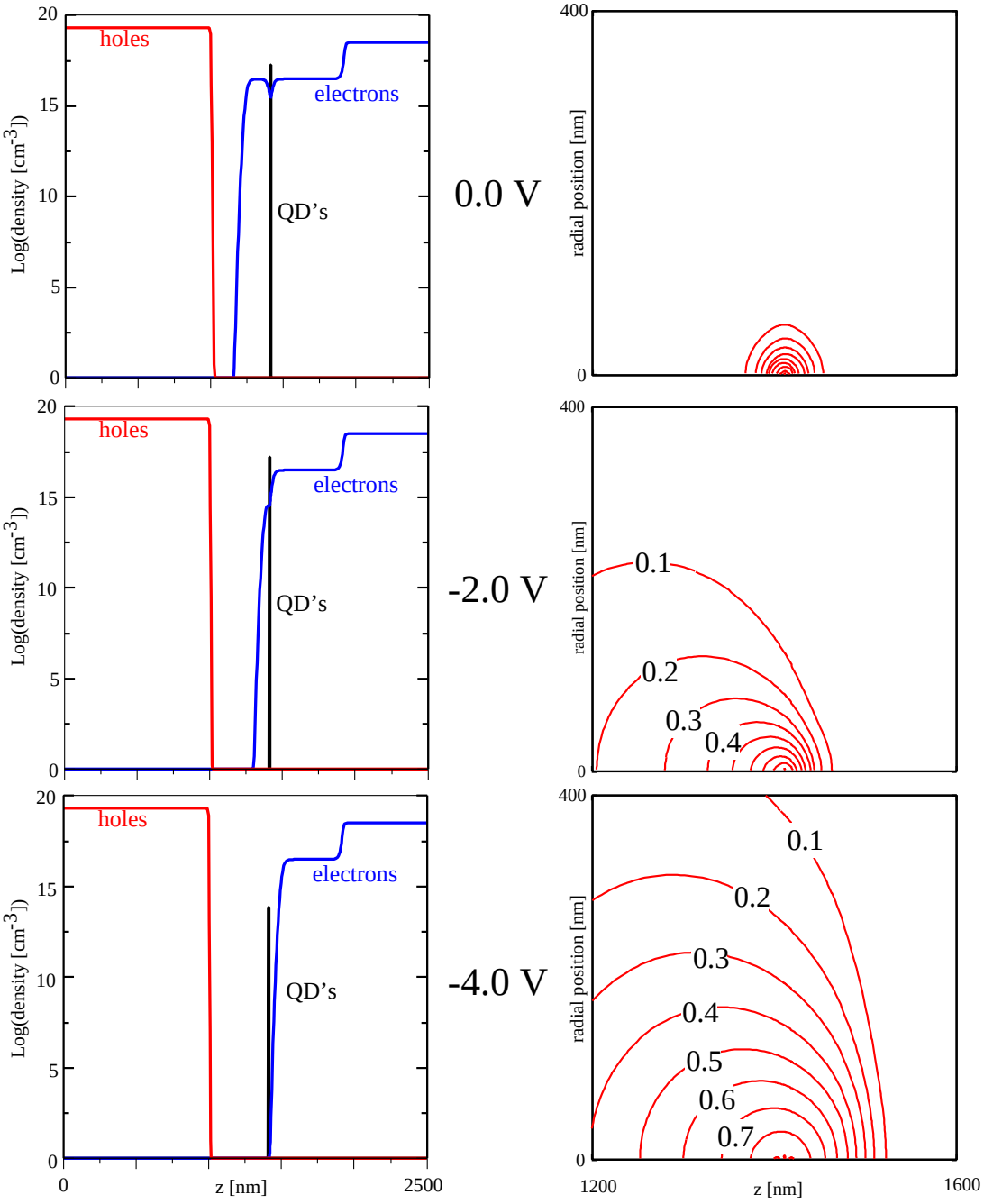

Figure 5.2: vertical bulk electron and hole and QD electron density distribution (left) and the Green's function normalized to the unscreened Green's function (right) for U=0.0 V, -2.0 V, and -4.0 V (model A)

(model A) to a value of about 18 meV. The effect of screening on the inter-QD charging is more significant. Here, the inter-QD charging is almost completely suppressed for $U \leq$-2.0 V, since the distance between the QDs is larger than the extension of the Green's function in the lateral directions. For larger reverse biases, the repulsion between the electrons in the QD layer rises continuously due to the reduction of the amount of screening which depends on the bias dependent depletion layer width. The inter-QD Coulomb repulsion of the two models deviates in the bias region where the QDs are occupied. Since the bulk electrons which do the screening are repelled by the QD electrons themselves which is not taken into account in model B, the inter-QD Coulomb charging is larger in model A.

So far, the actual occupation of the QDs which changes with the bias has not been considered. The resulting average charging energies per QD electron for both models are shown in Fig. 5.4 together with the one-dimensional potential barrier $e\hat{\Phi}^{1D}(z_{QD})$ as obtained from the one-dimensional Poisson equation (3.21). The latter can be conceived as a one-dimensional charging energy. The charging energy exhibits a nonlinear behavior. It rises with the reverse bias due to reduced screening effects, and drops when energetically higher lying QD levels are successively emptied. Figure 5.4 shows that a one-dimensional model underestimates charging effects by far for a QD occupation of more than two electrons per QD, but may also lead to a small overestimation, as shown here for an occupation of less than two. One also observes that the two models result in charging energies with a major difference for bias values where the QDs are occupied with more than four electrons.

5.4 Inhomogeneous QD charge

The statistical character and the dependence on the three-dimensional potential distribution of the microscopic capture and emission processes lead to fluctuations and an inhomogeneous charge distribution in the QD layer. Especially for biases when it comes to

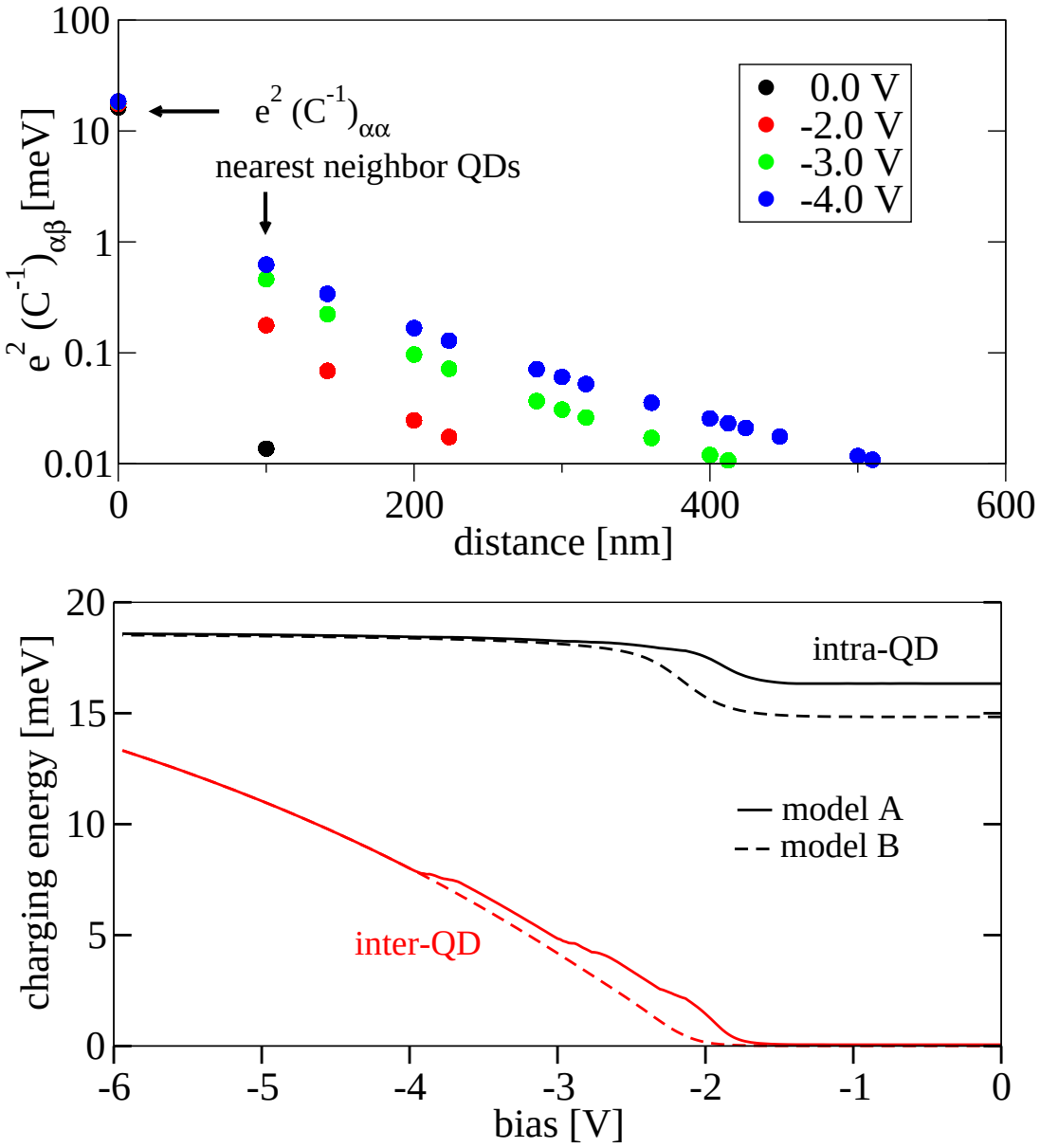

Figure 5.3: top: inverse capacitance matrix elements as a function of the QD-QD distance for U=0.0 V, -2.0 V, -3.0V and -4.0 V (model A); bottom: intra- (black) and inter-QD (red) charging energy as a function of the applied bias assuming one electron per QD; model A: solid lines; model B: dashed lines

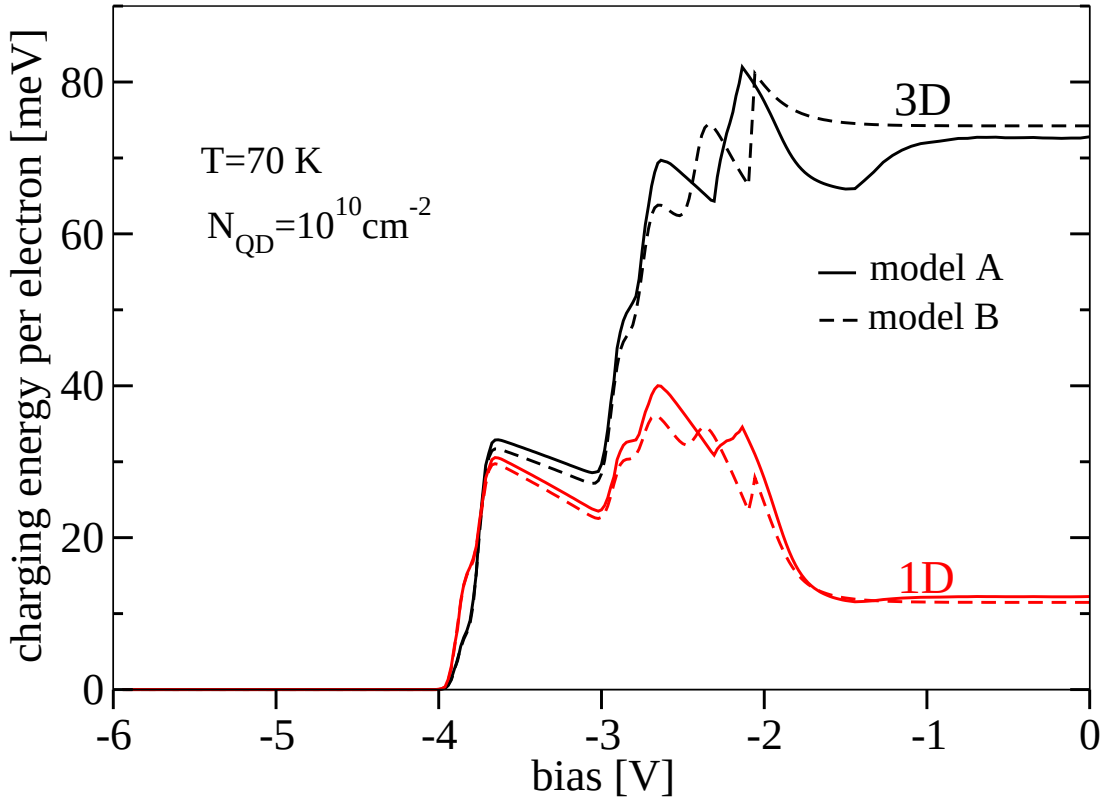

Figure 5.4: mean charging energy per QD electron as obtained from the three-dimensional calculation (black solid line: model A; black dashed line: model B), and the one-dimensional potential barrier $e\hat{\Phi}^{1D}(z_{QD})$ (red solid line: model A; red dashed line: model B) as a function of the bias

discharging processes, i.e., the difference between QD levels and the quasi-Fermi energy is of the order of k_BT, fluctuations in the QD charge will occur.

In the simulations, the QD levels are occupied statistically according to the Fermi distribution function (see Eqn. 3.34). Figure 5.5 shows a typical realization of the charge distribution in the QD layer for the bias range where the two QD ground state electrons are emitted. For the bias values, where the peaks are observed in the C-V characteristic (U=-3.73 V and U=-3.88 V) the degree of inhomogeneity is large, while the charge distribution is (almost) ho-

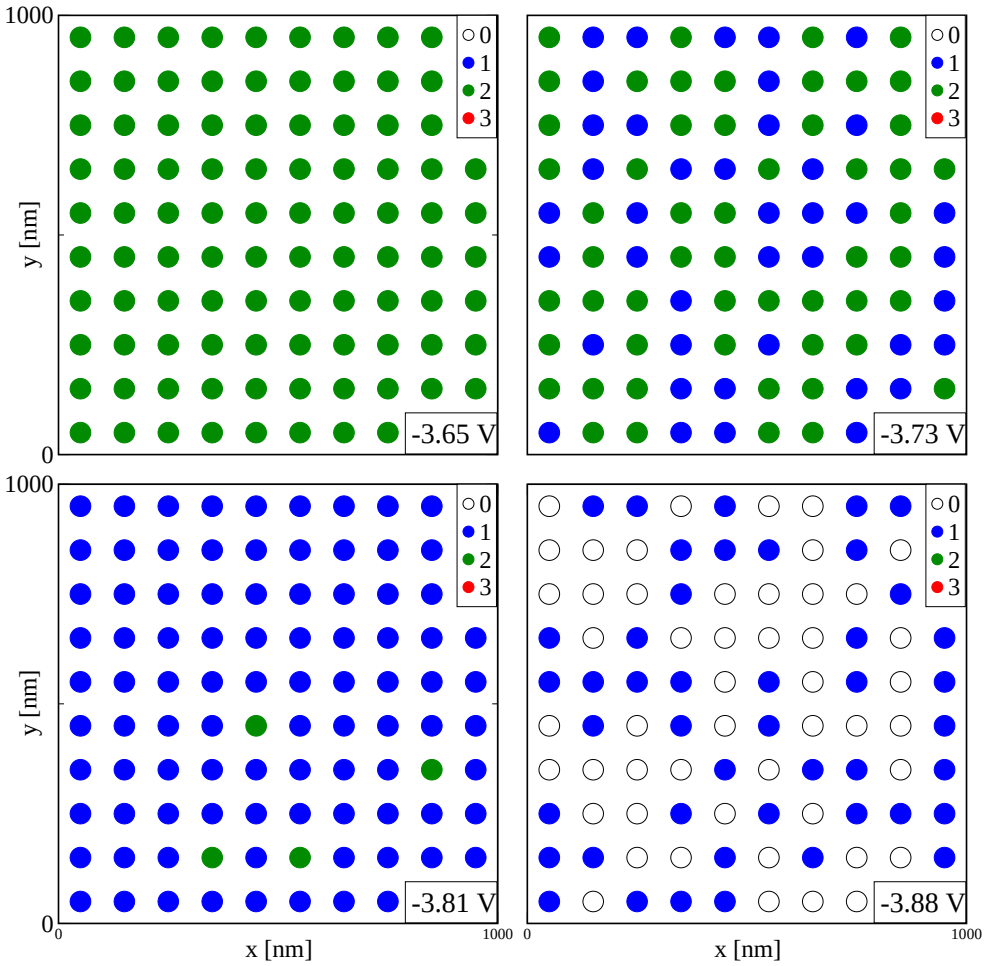

Figure 5.5: QD charge distribution for different bias values at T=70 K. The number of electrons per QD is represented by the color code.

mogeneous for biases outside the peaks (U=-3.65 V and U=-3.81 V).

The charge inhomogeneity in the QD layer together with the Coulomb repulsion between the QDs can lead to a broadening of the QD level energies as will be discussed in the following section.

5.5 Level energies

The charging effects determine the QD level energies during a bias sweep. Figure 5.6 shows the occupation and the energy of the (000) ground state level below the conduction band edge. The number

of electrons per QD is hereby indicated by colors. Rising inter-QD charging due to the change in the bulk charge distribution raises the QD level energies, shifting them towards the conduction band edge. Discharging processes of energetically higher electron levels on the other hand reduce the charging energy, leading to lower lying QD levels. This nonlinear dependence on the bias is indicated in Fig. 5.6 by a line which follows this zig-zag behavior of the level energy during a reverse bias sweep. Side peaks or two peaks occur if the QDs are not homogeneously charged. Additionally, the energy levels are broadened with rising bias, since the range of Coulomb forces rises with the bias. The individual charge distribution of the neighbor QDs leads to an individual change of the level energy of a depicted QD, and therefore to an overall broadening of the QD energies of the ensemble. Similar Coulomb mediated broadening effects have been found in the current-voltage characteristics of QD arrays embedded in a *p-i-n* diode [Kie03c, Kie02].

5.6 High QD sheet density

The Coulomb interaction between electrons trapped in different QDs of course strongly depends on the distance between the QDs. So far, a QD sheet density of N_{QD}=10^{10} cm^{-2} has been used with a corresponding QD-QD distance of 100 nm. This is a rather typical QD sheet density for self-organized InAs QDs, but also higher densities can be grown, depending on the growth conditions. Now a QD sheet density of N_{QD}=10^{11} cm^{-2} will be used which corresponds to a QD-QD distance of 31.6 nm, while using identical parameters as in the sections before.

The C-V characteristics for 70 K as obtained from model A and B are shown in Fig. 5.7. For biases where the two QD ground states (000) are discharged ($U \leq$-3.0 V) both models result in about the same characteristics. For biases where the QD sheet charge density is larger ($U \geq$-2.5 V) there is a major difference between both models.

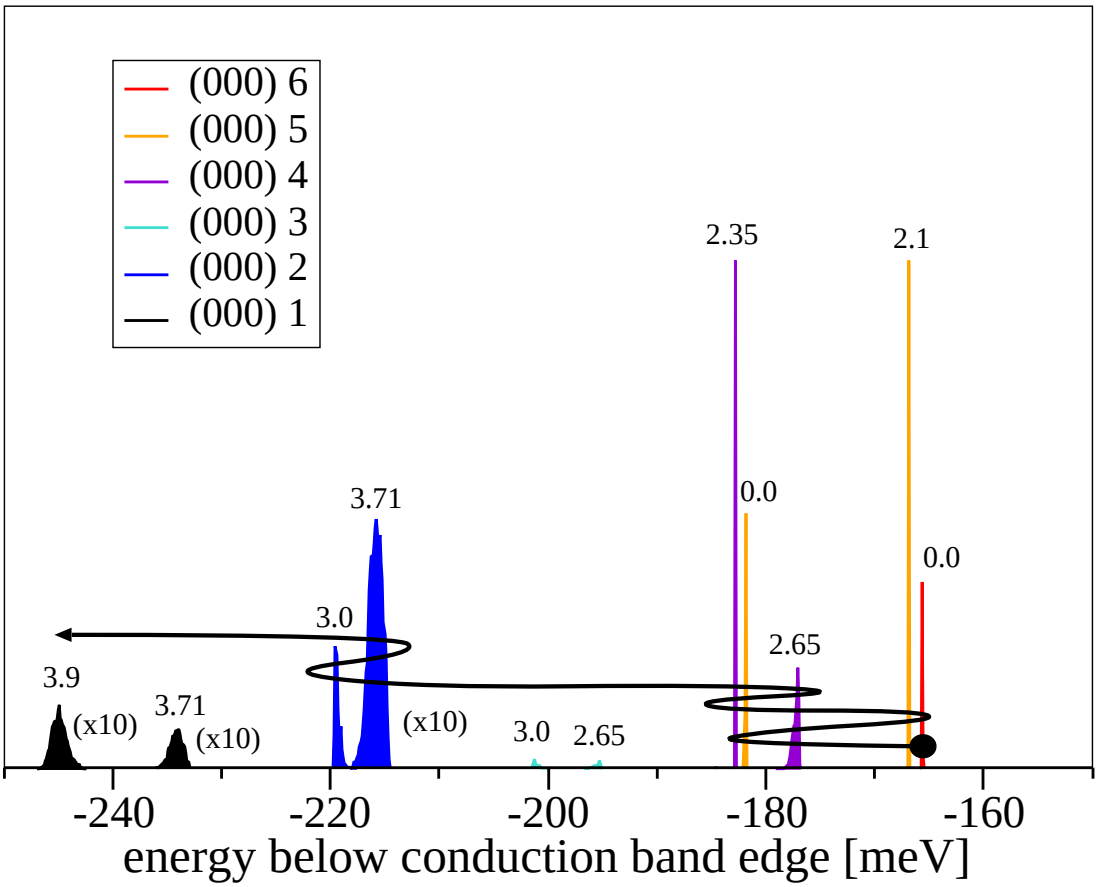

Figure 5.6: occupation (a.u.) of the (000) QD level for depicted reverse bias values in units of volts; the number of electrons per QD is indicated by colors

The curve calculated with model B shows a rather sharp peak structure for the discharging of the excited states (100) and (010). Especially, when changing the occupation from five to four electrons per QD a peak splitting occurs when the QDs are occupied with a fractional mean number of electrons. This result shows that the QD levels which have all four nearest neighbor QDs charged with five electrons have a different energy than QD levels which have their nearest neighbor QD charged with four electrons, and are therefore discharged at different biases. This splitting vanishes for the ground state electrons which show up a larger broadening in the C-V curve. This has to do with the range of the inter-QD charging. Where for

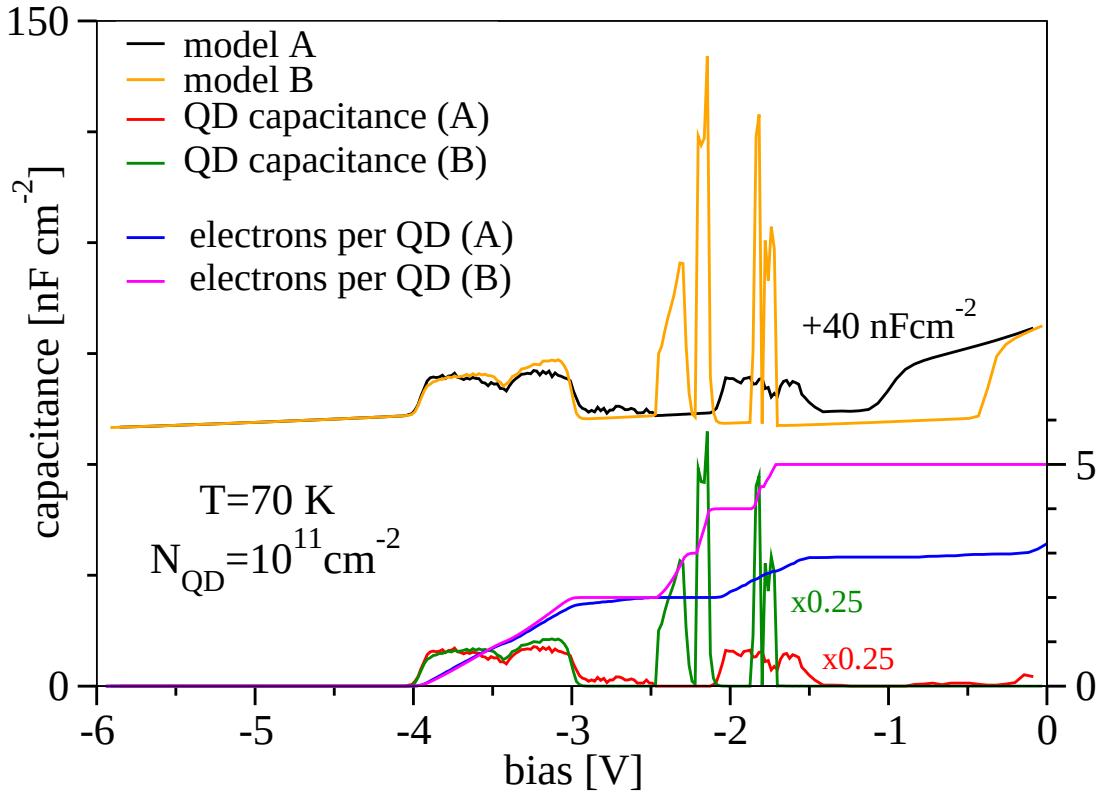

Figure 5.7: the capacitance-voltage characteristics for N_{QD}=10^{11} cm^{-2} at 70 K (model A: black line; model B: orange line), the QD capacitance (model A: red line; model B: green line), and the mean number of electrons per QD as a function of bias (model A:blue line; model B: magenta line)

the excited states the inter-QD range is rather short and mostly only the interaction between nearest neighbor QDs occurs, the ground state electrons are discharged where the inter-QD interactions range over a large number of neighbor QDs, leading to an averaging, and therefore broadening effect.

Obviously, the dependence of the capacitance matrix on the QD sheet charge density which is neglected in model B leads to an additional broadening effect of the sharp peaks as obtained by model B and to a shift towards a lower reverse bias. The latter can be explained by the fact that the screening effects are less in model A,

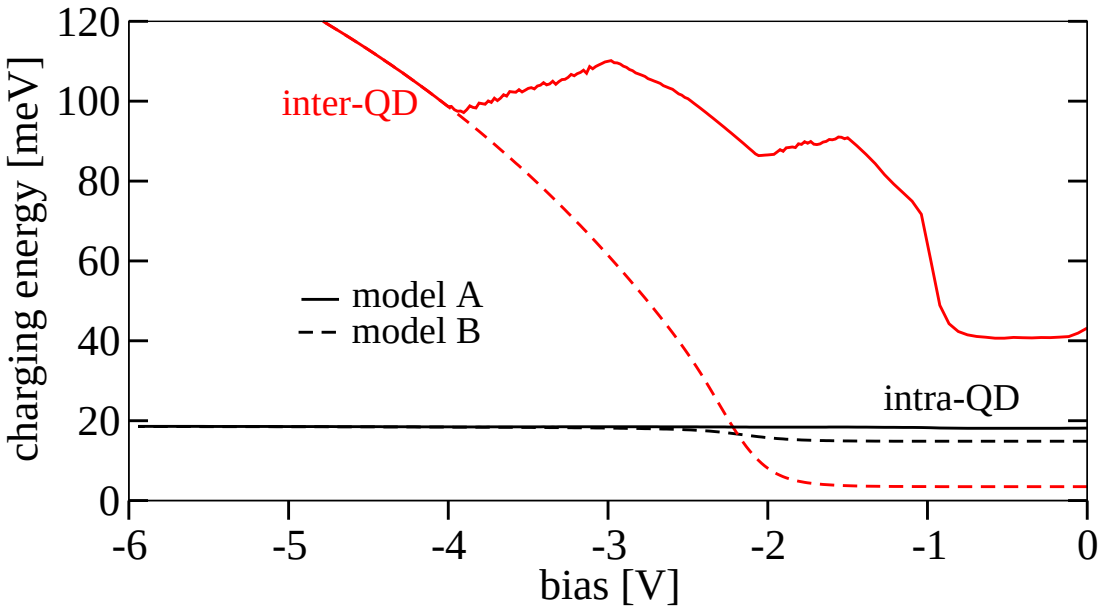

Figure 5.8: intra-QD (black) and inter-QD (red) charging energy as a function of the applied bias assuming one electron per QD for N_{QD}=10^{11} cm^{-2} at 70 K ; model A: solid lines; model B: dashed lines

since the surrounding bulk electrons are repelled by the QD sheet charge itself. The broadening also occurs from the inter-QD charging which has a longer range in model A. As mentioned earlier, the repulsion between a QD electron and its neighbor QDs can lead to a QD level broadening. Since the number of neighbor QDs is larger within the range of inter-QD Coulomb forces for a larger QD sheet charge density, this leads to an additional broadening.

For the two ground state levels both models result in a larger broadening, compared to the characteristics for N_{QD}=10^{10} cm^{-2} due to the larger inter-QD Coulomb charging.

The Coulomb charging as a function of the bias is plotted in Fig. 5.8. Compared to the calculations for N_{QD}=10^{10} cm^{-2}, the intra-QD charging energy has similar values, and also the two models result values which differ only marginal. As expected, the higher QD sheet density has a huge effect on the inter-QD charging energy. It rises with the reverse bias, and becomes even much larger than

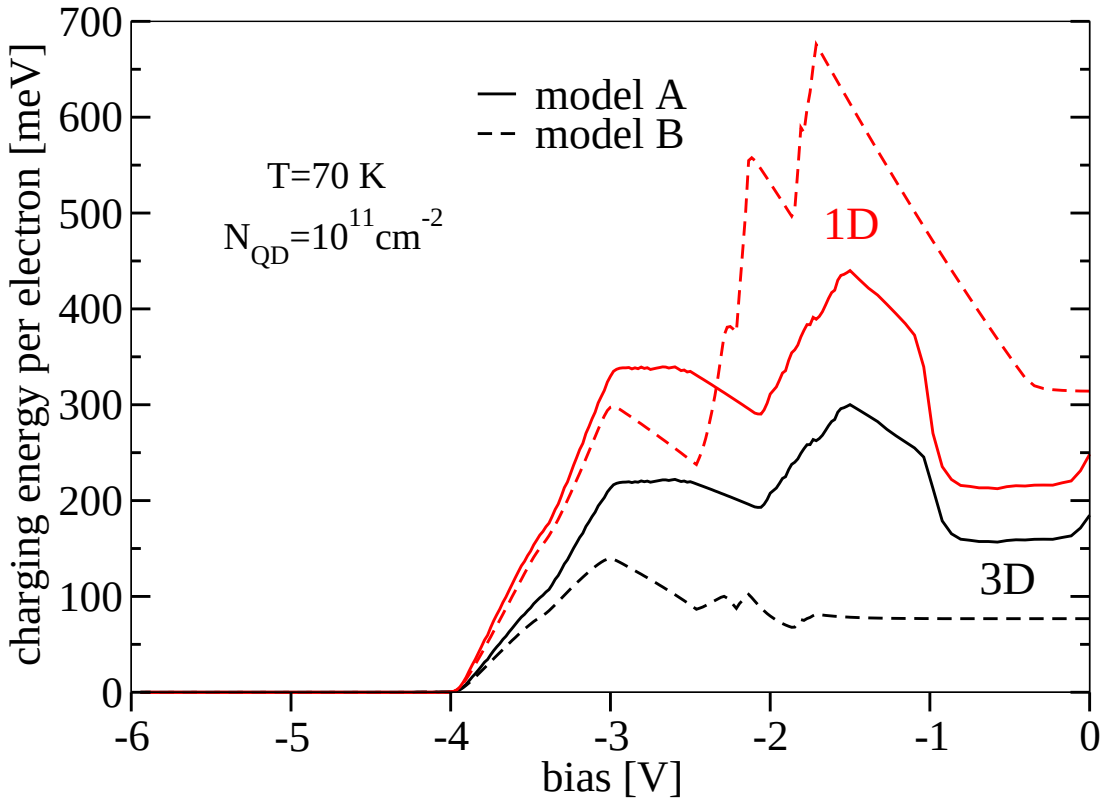

Figure 5.9: mean charging energy per QD electron as obtained from the three-dimensional calculation (black solid line: model A; black dashed line: model B), and the one-dimensional potential barrier $e\hat{\Phi}^{1D}(z_{QD})$ (red solid line: model A; red dashed line: model B) as a function of the bias

the intra-QD charging. For such a large QD density per unit area, model B obviously looses validity, since it strongly underestimates the true Coulomb interaction between the QDs.

Taking into account the actual occupation of the QDs leads to the mean charging energy per QD electron as shown in Fig. 5.9. The results from model B deviate strongly from the more accurate model A. Model B typically over-estimates the one-dimensional charging energy $e\hat{\Phi}^{1D}(z_{QD})$ (red dashed line in Fig. 5.9), where it underestimates the mean three-dimensional charging energy per QD electron (black dashed line in Fig. 5.9). Comparing the 1D and 3D

charging energies as obtained with model A (solid lines in Fig. 5.9), one observes that the 1D charging energy is even larger than the 3D values, just vice versa as for the case N_{QD}=10^{10} cm^{-2}. For the large QD sheet density, the localization of the electrons in QDs reduces the over-all Coulomb repulsion. In other words, the localization "costs" less charging energy, than if the electrons were delocalized in the lateral directions.

5.7 *p-i-n* diode structure

As an alternative to the *pn* structures investigated so far, the QDs can for example also be embedded in a *p-i-n* device to do C-V spectroscopy. The QDs are located within the intrinsic, undoped region, between the highly doped contact regions. A sketch of the conduction band for this device in shown in Fig. 5.10. In contrast to the *pn* diode, the QDs are uncharged in equilibrium. A forward bias is applied to charge the QDs successively. The bulk charge in the vicinity of the QDs is negligible, and the inter-QD charging energies are mainly defined by the distance of the QDs to the doped contact layers.

Due to the linear field distribution in the charge neutral layer, the capture and emission processes in such structures are based on the tunneling of the electrons between the conduction band and the QDs. The temperature independence of these emission and capture processes makes in contrast to the *pn* diodes stationary C-V spectroscopy possible even for very low temperatures [Mil97].

Here, two samples are investigated, where the QD layer is positioned 600 nm and 150 nm from the *p*-contact and 200 nm and 50 nm from the *n*-contact to which will be referred to as sample A and sample B, respectively. Arrays of QDs as in the previous sections are simulated with N_{QD}=10^{10} cm^{-2} at T=70 K.

Figure 5.11 shows the resulting C-V characteristics of both structures. Since the electric field in the intrinsic region is proportional to the applied bias, the background capacitance of the diode mainly

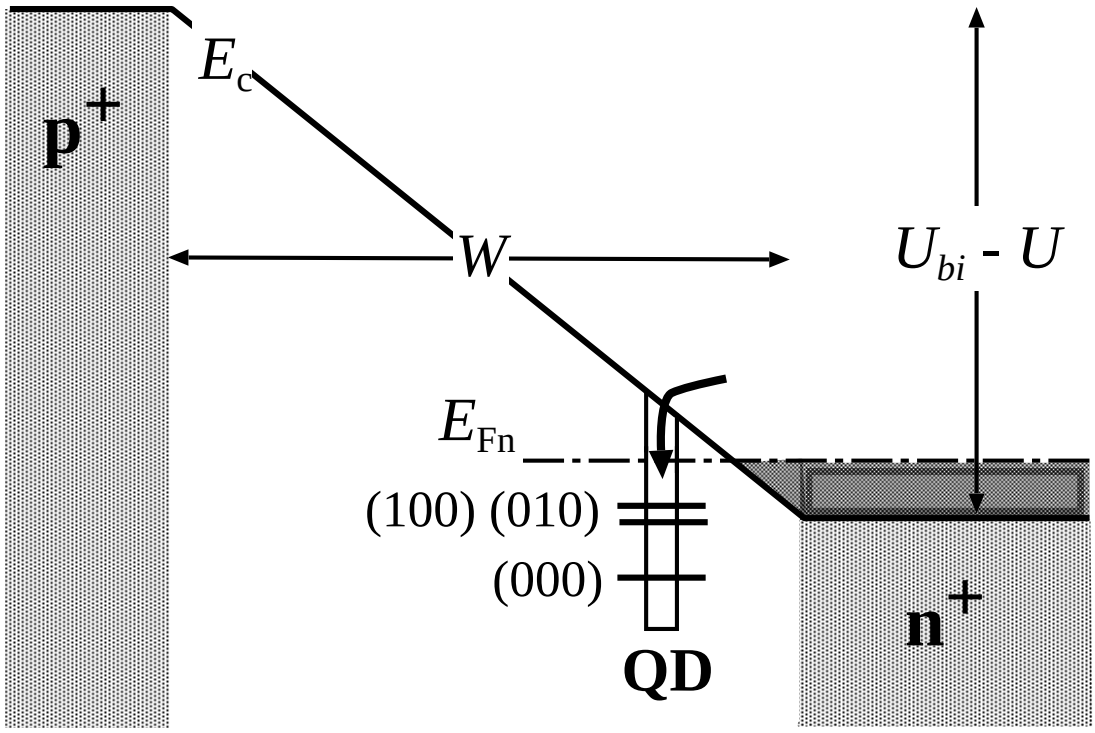

Figure 5.10: band sketch of a *p-i-n* diode with an embedded array of QDs

appears as a constant background. In addition to this background, peaks originating from the charging of the two ground state electrons and the excited electrons appear.

A comparison between the C-V curves of the two samples demonstrates once again the role of the surrounding bulk charge density. For sample A, the peaks appear broader than for sample B, since the distance between the n^+ contact and the QDs is larger than in sample B.

5.8 Summing-up

At this point a short summary is made of what has been found out about self-consistent Coulomb effects in QD arrays.

The intra-QD charging energy, i.e., the Coulomb energy which is necessary to put an additional electron on a QD is typically about

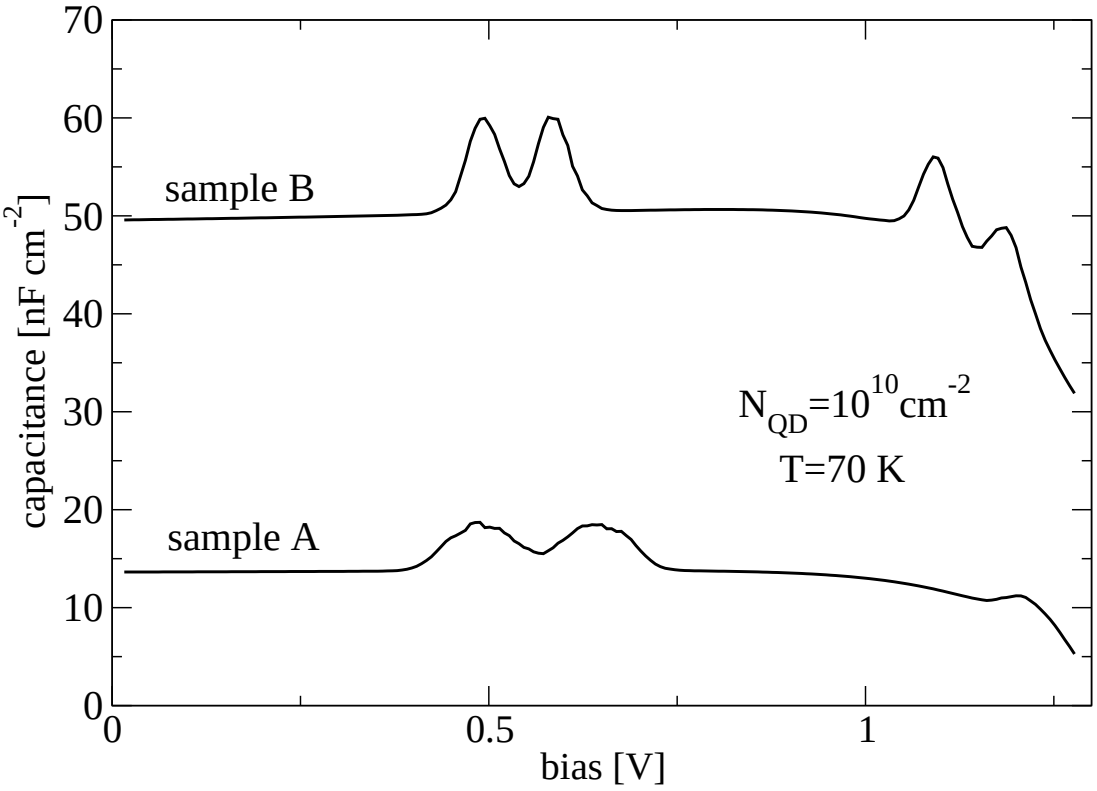

Figure 5.11: C-V characteristics of *p-i-n* diodes as displayed in Fig. 5.10; The distance between the QDs and the *n*-contact is chosen differently in sample A (200 nm) and sample B (50 nm).

20 meV for InAs QDs with a size of 15 nm. It is almost independent of the surrounding bulk charge distribution, and therefore of the applied bias.

The Coulomb charging between different QDs in the QD layer has a huge impact on the level energies of the QD ensemble. It strongly depends on the surrounding bulk charge distribution which is given by the material properties in the vicinity of the QDs, and it can be manipulated, e.g., by applying a bias.

The impact of the strength of inter-QD Coulomb charging on the QD level energies and the C-V characteristics can be classified into three regimes. First, the bulk charge distribution surrounding the QDs is closer than the distance between the QDs so that the

Coulomb interaction between the QDs is negligible. Then QDs are electrically independent from each other, and the level energies are only given by the charge on the QDs themselves. The discrete density of states of the QDs is preserved.

If the range of inter-QD Coulomb interaction is about of the range of the QD-QD distance, the repulsion between nearest neighbor QDs leads to different level energies for inhomogeneously occupied QD arrays. This nearest neighbor charging leads to a splitting of the peaks in the C-V characteristics for large QD sheet densities.

A long range Coulomb interaction which ranges over a larger number of inhomogeneously charged neighbor QDs leads to a broadening of the QD levels. The broadening of the QD levels also leads to a broadening in the C-V curves.

6 Fluctuations

It has been shown in the previous chapter that the inhomogeneous QD charge distribution together with the inter-QD charging leads to a broadening of the QD levels, and to a broadening in C-V characteristics. So far, a temperature dependent broadening has not been discussed explicitly. In addition, the QDs have been idealized by assuming that they are all of identical size and are periodically ordered. The latter is a strong approximation, since the QDs investigated here are "naturally" grown by self-organization. Such growth processes are always subject to fluctuations, and QDs are not equi-sized and deviate from a periodic ordering.

6.1 Temperature fluctuations

By changing the temperature, the statistics of the QD level occupation is modified. The crucial point which determines the inhomogeneity of the self-consistent QD charge distribution is the relation between the thermal energy k_BT and the QD level- and charging energies. Additionally, the amount of screening by bulk electrons changes with temperature. With lower temperature the amount of screening is stronger, since the electrons follow potential fluctuations in a more pronounced way than for higher temperatures.

The simulated C-V characteristics for T=4 K, 70 K, and 300 K for N_{QD}=10^{10} cm^{-2} and N_{QD}=10^{11} cm^{-2} as well as the mean number of electrons per QD are plotted in Fig. 6.1. The C-V characteristics for 4 K and N_{QD}=10^{10} cm^{-2} shows up six sharp peaks, corresponding to the discharging of the QDs initially occupied with six electrons. The width of the peaks at a low temperature is mainly given by the Coulomb interaction with the nearest neighbor QDs. QDs with

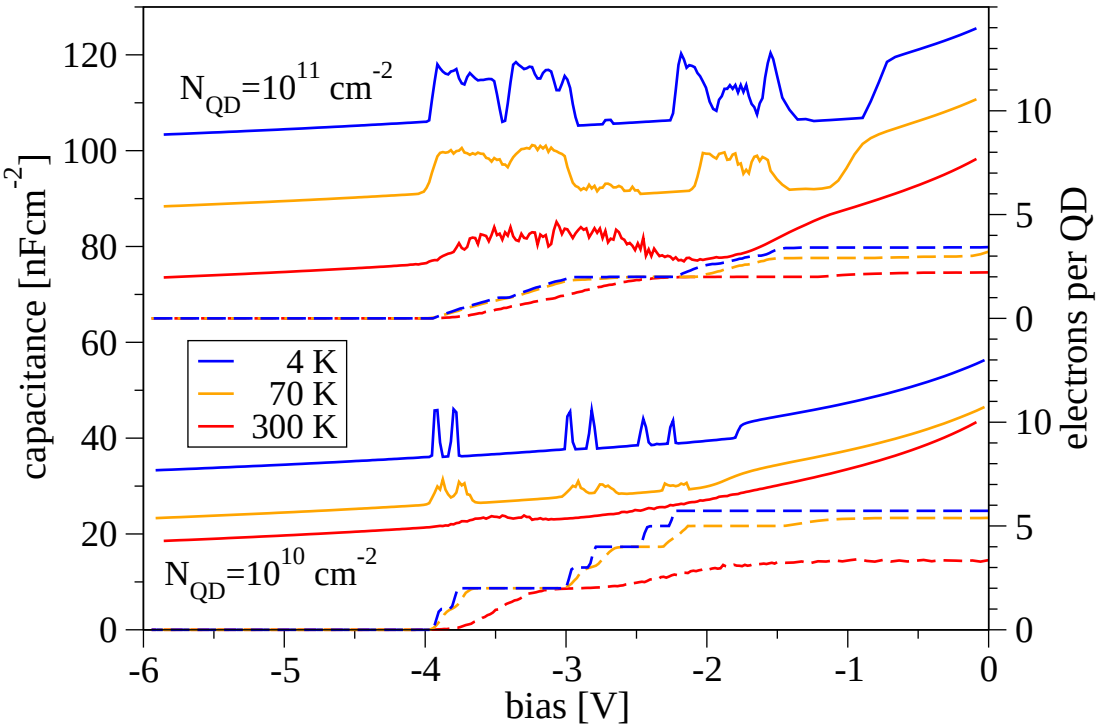

Figure 6.1: C-V characteristics (solid lines) at T=4 K (blue), 70 K (orange), and 300 K (red), for N_{QD}=10^{10} cm^{-2} and N_{QD}=10^{11} cm^{-2}, and the corresponding occupation of the QDs (dashed lines); C-V curves are offset for clarity, except the curve for 300 K and N_{QD}=10^{10} cm^{-2}.

all four neighbor QDs occupied with electrons are discharged at a different bias than QDs where all four neighbors are already discharged. For T=70 K the peaks are thermally broadened, but can still be observed as peaks. At room temperature the peak structure is totally gone. Instead, the discharging of the QD electrons appears as a broad plateau. Here, the thermal energy k_BT is larger than the intra-QD as well as the inter-QD charging energy. Additionally, the QDs are only occupied with about three electrons at zero bias, since for high temperatures the degree of degeneracy is lower, thus the quasi-Fermi level is lying lower relatively to the conduction band edge.

With rising temperature, the peaks are shifted towards lower reverse biases. As mentioned above, the amount of screening by

the surrounding bulk electrons is reduced with rising temperature, which leads to higher QD level energies, and the discharging of theses levels appears then at a lower reverse bias.

For N_{QD}=10^{11} cm^{-2} the peaks in the C-V characteristics are much broader compared to N_{QD}=10^{10} cm^{-2}. Obviously, the increasing inter-QD Coulomb charging effects due to the reduced distance between the QDs lead to the broadening. But still, each of the four levels which are initially occupied can be identified. Interestingly, the splitting between QD levels with an occupation larger and smaller than 3.5 can be clearly observed. For T=70 K this spitting vanishes, but the discharging of the four electron levels is still observable by broadened peaks. Again, at 300 K thermal broadening lets the peak structure disappear.

6.2 Structural Fluctuations

For most applications involving QDs, it is a key importance to have equally sized QDs to achieve a well defined response to optical or electronic signals, keeping losses as small as possible. Also a high degree of ordering is often desired to achieve high QD sheet densities. Unfortunately, the self-organized growth process of QDs is always subject to fluctuations. The positions of the QDs deviate from a periodic ordering, and the QDs are to some extend of different size. Principally it should be possible to obtain information about growth conditioned fluctuations by an analysis of C-V characteristics. Typically such fluctuations should lead to additional broadening effects in the C-V characteristics, which makes a clear distinction from Coulomb charging effects or thermal fluctuations necessary. The simulations performed with the one-dimensional model in chapter 4 already provided a method to obtain the broadening of the QD levels, but a differentiation between a broadening due to Coulomb charging and the residual broadening due to structural fluctuations was not possible. Therefore, an ensemble of uni-sized QDs but with a random QD position in the QD layer is simulated first, before ad-

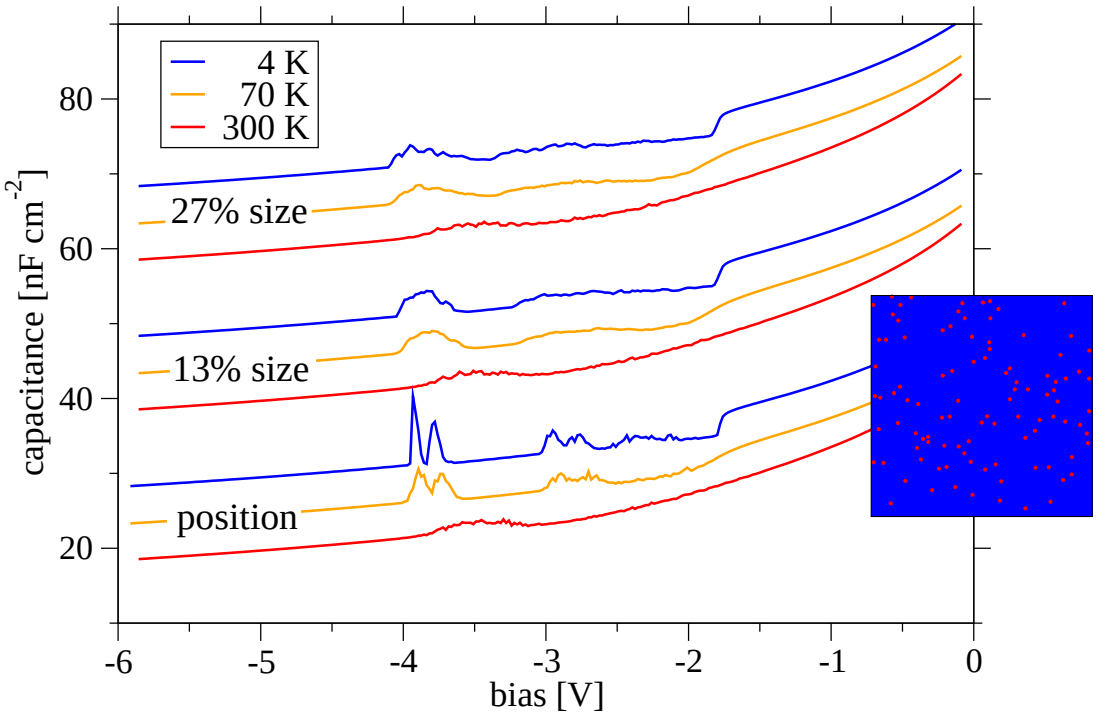

Figure 6.2: C-V characteristics for N_{QD}=10^{10} cm^{-2} with random position fluctuations, a random size fluctuation of ±13 %, and a random size fluctuation of ±27 % at T=4 K (blue), 70 K (orange), and 300 K (red); C-V curves are offset for clarity, except the curve for 300 K with position fluctuations. The inset shows the 1000 nm×1000 nm sample with random position fluctuations.

ditional random QD size fluctuations are considered. Finally, also samples from Kinetic Monte-Carlo (KMC) simulations are investigated.

6.2.1 Random Position

Figure 6.2 shows the C-V characteristics for the *pn* diode as in the previous chapter, but where the QDs have random positions in the lateral directions. The positions have been chosen such that two QDs never have the same position or overlap. As can be seen for

the curve for 4 K, position fluctuations mainly have a broadening effect on the excited states. Obviously, with rising bias, and therefore with rising inter-QD charging the position fluctuations are evened out. When the excited states are discharged, the nearest neighbor charging plays the major role which suffers from the position fluctuation. With a long range inter-QD Coulomb charging it comes to an averaging of the Coulomb repulsion of many neighbor QDs, leading to more similar energies for all QD levels. With rising temperature, thermal fluctuations dominate the shape of the C-V curve.

6.2.2 Random Size

Fluctuations in the QD size is investigated next. A shape dependence of the QD level energies is hereby neglected, thus all QDs are uniform. In addition to the random position fluctuations, a uniform random distribution of the QD size between a QD diameter of 13 nm and 17 nm is chosen. This corresponds to a relative width of the fluctuation of ± 13 %. The C-V characteristics of this ensemble is shown in Figure 6.2. The size fluctuations lead to a broad plateau for the excited states, but the two ground state electrons still appear as a single broadened peak. This reflects the fact that the intrinsic QD level energies of the excited states are more sensitive to size fluctuations than the ground state electrons (see Fig. 3.2).

Using a random size distribution between 11 nm and 19 nm, which corresponds to a fluctuation of ± 27 %, leads to the formation of plateaus even for the ground state. A qualitative comparison of the C-V characteristics with experimental data which show up plateaus for all QD levels (e.g. Ref. [Kap00a]) indicates that the typical size fluctuations of InAs QDs is about $\pm 30\%$.

Fig. 3.2 indicates that such a size fluctuation corresponds to an energy fluctuation of about 70 meV (full width). In contrast, the one-dimensional calculations in chapter 4 resulted in a broadening of the spin-degenerate ground state level about twice as large than obtained here. This indicates, that a significant part of the total broadening of the QD levels originates from Coulomb charging. A

value of ±30 % for the size distribution as obtained for random fluctuation in this section also agrees well with the typical size distribution as obtained from Kinetic Monte-Carlo growth simulations [Mei02a].

6.2.3 Samples from KMC simulations

So far, C-V spectroscopy has been used to learn about the detailed potential distribution, and to obtain information about the size distribution in QD arrays by a quantitative and qualitative comparison of the simulations to experimental data. Within the three-dimensional simulations, position fluctuations or fluctuations in the size have been chosen randomly. Now for the first time QDs ensembles taken from Kinetic Monte-Carlo (KMC) growth simulations as performed in the group of Prof. Schöll at the TU Berlin are used. Thus a full, consistent description of self-organized QDs including growth and electronic properties has been achieved. This elucidates the physics of self-assembled QDs.

These KMC simulations are limited to the initial, two dimensional phase of growth, where the first layer is formed after the wetting layer has been established. Hereby the strain field induces the size ordering but it is related to the spatial ordering as well. Most important growth parameters are, as in the real fabrication, growth temperature, the flux of the deposited material, and the total coverage given in units of monolayers (ML) of the substrate. A detailed description of KMC can be found in Ref. [Mei02a].

The following context refers to sample A which has a coverage of 0.2 ML (or 20 %), and sample B with a coverage of 0.25 ML (or 25 %). Both samples were simulated for a growth temperature of 700 K and a flux of 0.01 ML/s. Figure 6.3 displays a topview of the two 200 nm×200 nm samples, where the wetting layer and the QDs are colored in blue and red, respectively. The size distribution histograms are also shown. It should be noted that both samples originate from the identical simulation, what explains the similarity of the two structures. An estimate of the full width at half max-

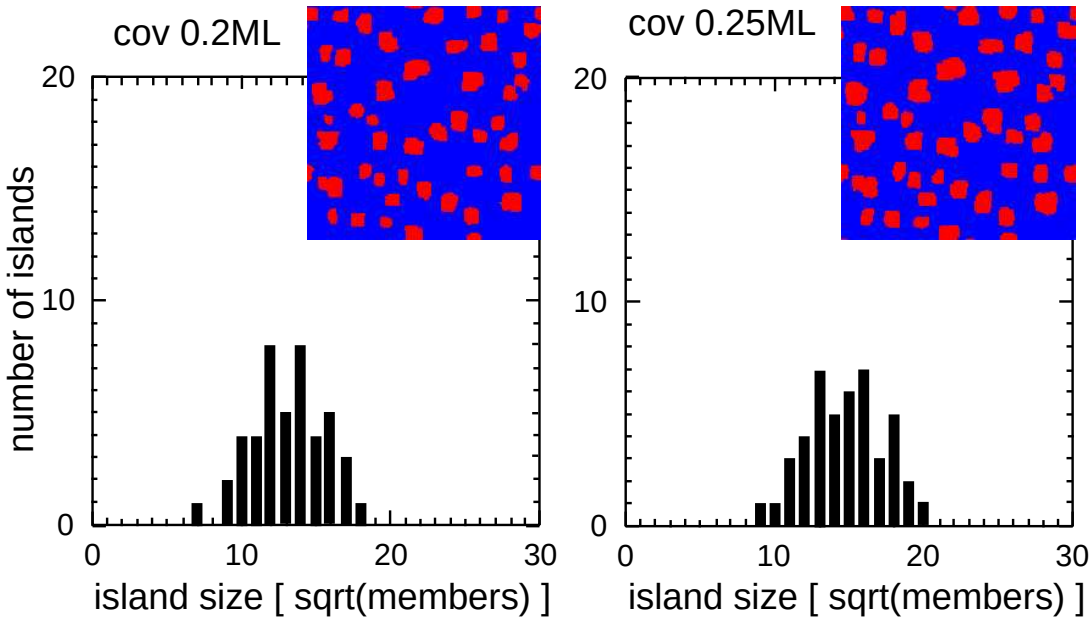

Figure 6.3: Two 200 nm×200 nm samples of QDs grown by KMC simulations: left: coverage of 20 % (sample A); right:coverage of 25 % (sample B) (by courtesy of Roland Kunert, TU Berlin); For both samples a growth temperature of 700 K, a deposition rate of 0.01 ML/s, and a simulation time of 50 s have been used.

imum of these distributions is in agreement with the fluctuations of 30% as found with the random fluctuations. Both samples have a QD sheet density of 1.125×10^{11} cm^{-2}. The shape fluctuations of the QDs is neglected, thus the simulated QDs are approximately replaced by cylinder shaped QDs matching the size of each QD leading to average QD diameters of 14.8 nm in sample A and 16.6 nm in sample B. A QD height of 3 nm is used for all QDs.

Figure 6.4 shows the C-V characteristics of sample A and B at T=70 K and the corresponding occupation of the QDs with electrons. Both simulated C-V curves are rather similar, but sample B tends to have a higher QD occupations since the QDs are in average little larger than in sample A. The discharging of the (000) ground state appears as a modulation of the C-V characteristic, providing interesting information about the QD ensemble. The discharging

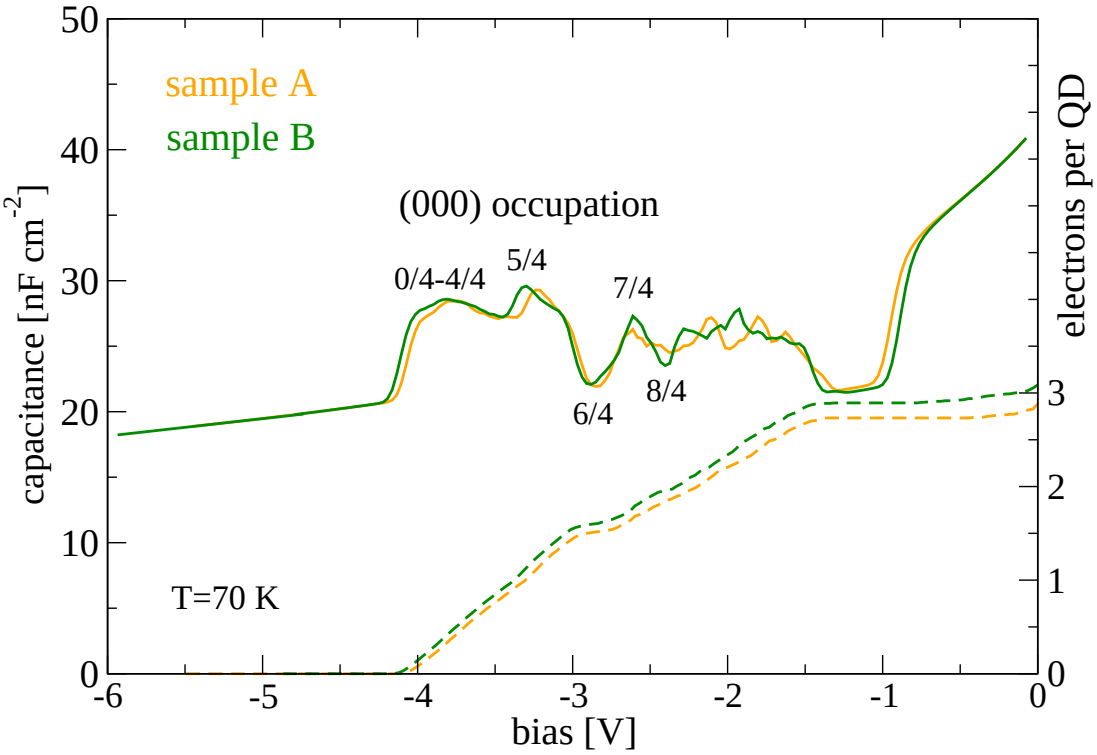

Figure 6.4: C-V characteristics at T=70 K for the samples A and B as shown in Fig. 6.3 and the corresponding mean occupation of the QDs

of the second last electron is ruled by the inter-QD charging. The fractional occupation in fractions of one quarter is observable very clearly from the C-V curve, and the inter-QD charging with the four nearest neighbor QDs as explained in the previous chapter has been identified as the responsible mechanism. As a consequence, the positions of the QDs must be correlated such that each QD has effectively four nearest neighbors. This is manifested by a look at the samples as shown in Fig. 6.3.

When discharging the last QD electron, this inter-QD charging is not resolved anymore, due to the reduced screening and the long range of the inter-QD charging.

7 Remote Coulomb scattering

The free bulk carrier distribution in the vicinity of QDs not only influences their energy levels by charging effects as shown in chapters 5 to 6. Coulomb scattering between QD electrons and continuum electrons over some distance from the QDs can lead to an energy relaxation or excitation in QDs. The energy difference between two QD levels i and j is hereby transferred to the remote continuum states. Similar investigations of energy relaxation have been made on He^+ ions near metal surfaces [Ech85, Fon93, Mon95, Caz98]. Here, continuum states can originate from the wetting layer, a quantum well (2DEG), a doped bulk region, or a metal contact (3DEG). Figure 7.1 shows the sketched band profile of a QD with the energy levels E_i and E_j, a quantum well and doped bulk region with the continuum states $\boldsymbol{k}$ and $\boldsymbol{k}'$ and a distance d to the QD.

This chapter proposes a theoretical description of the remote Coulomb scattering [Wet03a]. First, the scattering probabilities between an occupied QD state and an occupied continuum state into an empty QD state and an empty continuum state are calculated. The effective Coulomb potential is considered as a time-dependent perturbation and includes static screening effects within the Debye screening approach, taking into account the three-dimensional Poisson equation. The total probability is then obtained by a multidimensional numerical integration over the continuum $\boldsymbol{k}$-space.

7.1 General

The transition probability per unit time between the QD states i and j, and the continuum states $\boldsymbol{k}$ and $\boldsymbol{k}'$ is calculated by Fermi's

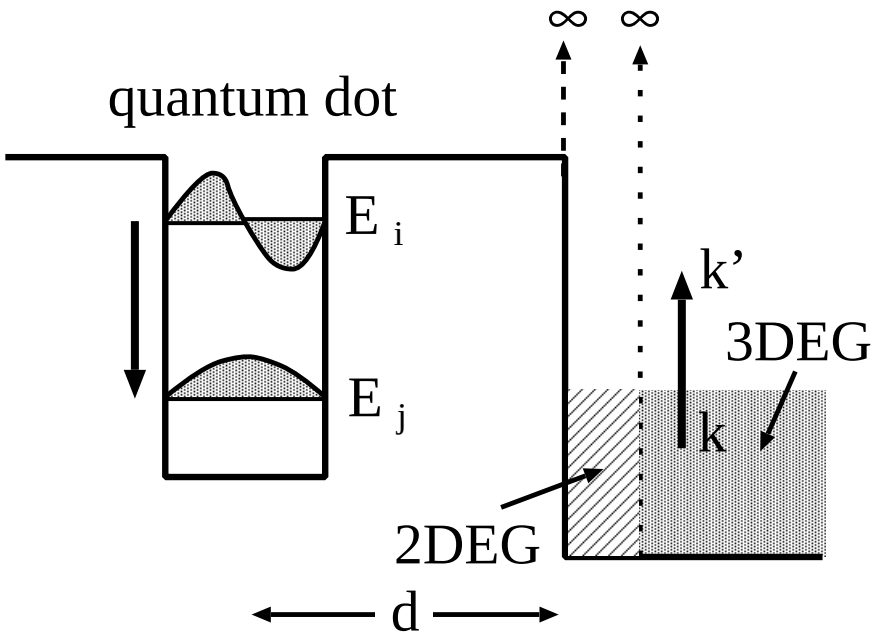

Figure 7.1: sketched band profile of a QD with the two energy levels E_i and E_j, a remote quantum well confined by infinite barriers (2DEG) and a remote bulk region, semi-confined by an infinite barrier (3DEG) with the distance d to the QD; The arrows indicate the remote Coulomb scattering process leading to an energy relaxation in the QD (Auger-process) [Wet03a].

Golden Rule

$$W_{i\boldsymbol{k}\to j\boldsymbol{k}'} = \frac{2\pi}{\hbar}|M_{i\boldsymbol{k}\to j\boldsymbol{k}'}|^2\delta(E_{\text{ini}} - E_{\text{fin}}), \tag{7.1}$$

where $E_{\text{ini}} = E_i + E_{\boldsymbol{k}}$ and $E_{\text{fin}} = E_j + E_{\boldsymbol{k}'}$ are the initial and final energies. The matrix element is given by

$$M_{i\boldsymbol{k}\to j\boldsymbol{k}'} = \iint d^3\boldsymbol{r}d^3\boldsymbol{r}'\psi^*_{\boldsymbol{k}'}(\boldsymbol{r})\psi^*_j(\boldsymbol{r}')U(\boldsymbol{r},\boldsymbol{r}')\psi_i(\boldsymbol{r}')\psi_{\boldsymbol{k}}(\boldsymbol{r}), \tag{7.2}$$

where ψ_i, ψ_j, $\psi_{\boldsymbol{k}}$ and $\psi_{\boldsymbol{k}'}$ symbolize the respective wave functions [Lan91]. U represents the effective Coulomb potential which can be written in a Fourier representation as

$$U(\boldsymbol{r},\boldsymbol{r}') = \frac{1}{A}\sum_{\boldsymbol{q}'} U(q',z,z')e^{i\boldsymbol{q}'(\boldsymbol{r}_{\shortparallel}-\boldsymbol{r}'_{\shortparallel})}, \tag{7.3}$$

with

$$U(q', z, z') = \frac{e^2 e^{-q'(z-z')}}{2q'\epsilon_0\epsilon_r\epsilon_e(q', z, z')}. \tag{7.4}$$

Here, ϵ_r and ϵ_0 are the relative and absolute permittivities, $e > 0$ is the elementary charge, A is the normalization area, and $\boldsymbol{q}'$ is a two-dimensional wave vector with $|\boldsymbol{q}'| = q'$. $\boldsymbol{r}_{\shortparallel}$ denotes the lateral position, and z is the vertical position. The dielectric function ϵ_e accounts for static screening effects of free electron charges which is calculated in the following section. The evaluation of the matrix elements (7.2) depends on the QD wave functions which depend crucially on their shape. Since the wave functions $\psi_i(\boldsymbol{r})$ and $\psi_j(\boldsymbol{r})$ are orthogonal, the lowest order contribution of the integral results from the dipole moment $-e\mathbf{a}$ of the effective charge density $-e\psi_j^*(\boldsymbol{r})\psi_i(\boldsymbol{r})$. This transition dipole moment is approximated by two localized charges of opposite sign

$$\int d^3\boldsymbol{r}'\psi_i^*(\boldsymbol{r}')U(\boldsymbol{r}, \boldsymbol{r}')\psi_i(\boldsymbol{r}') \approx U(\boldsymbol{r}, \frac{\boldsymbol{a}}{2}) - U(\boldsymbol{r}, -\frac{\boldsymbol{a}}{2}), \tag{7.5}$$

where the center position of the QD is chosen as $\boldsymbol{r}' = 0$. The total transition probability is then obtained from an integration over the continuum states

$$W_{i\to j} = \left(\frac{2\Omega}{(2\pi)^n}\right)^2 \iint d^n\boldsymbol{k} d^n\boldsymbol{k}' W_{i\boldsymbol{k}\to j\boldsymbol{k}'} f_k[1 - f_{k'}], \tag{7.6}$$

where f_k and $f_{k'}$ are the Fermi-distribution functions of the initial and final continuum states. Here, n symbolizes the dimension of the continuum electron gas and Ω is a volume of dimension n ($n = 2$ and $\Omega = A$ for a two-dimensional electron gas and $n = 3$ and $\Omega = AL$ for a three-dimensional electron gas).

7.2 Effective Coulomb potential

Before the formulas for the remote Coulomb scattering matrix elements can be derived, expressions for the dielectric function ϵ_e are needed. Therefore, the three-dimensional potential distribution for

a point-like charge in the presence of a 2DEG and a semi-confined 3DEG is calculated.

7.2.1 2DEG

Since the dielectric function will be a function of the vertical position and the two-dimensional Fourier component, the three-dimensional Poisson equation is solved in the two-dimensional Fourier space. The Fourier components of the Poisson equation for the potential U_{ind} induced by the charge e positioned at $z = 0$ read as

$$-q^2 U_{\mathrm{ind}}(q,z) + \partial_z^2 U_{\mathrm{ind}}(q,z) = -\frac{e^2 \delta n_{\mathrm{2D}}(q)}{\epsilon_0 \epsilon_r} \delta(z-d). \tag{7.7}$$

Here, δn_{2D} denotes the corresponding induced charge in the 2DEG layer positioned at $z = d$. The continuous solution of Eqn. (7.7) is given by

$$U_{\mathrm{ind}}(q,z) = \frac{e^2}{2\epsilon_0 \epsilon_r} \delta n_{\mathrm{2D}}(q) e^{-q|z-d|}. \tag{7.8}$$

Within the Debye screening approach, the induced sheet charge can be expressed as

$$\delta n_{\mathrm{2D}}(q) = \frac{\partial n_{\mathrm{2D}}}{\partial E_{\mathrm{F}}} \left[U_{\mathrm{ind}}(q,d) + U_{\mathrm{ext}}(q,d) \right], \tag{7.9}$$

with the external potential originating from the charge e at $z = 0$

$$U_{\mathrm{ext}}(q,d) = \frac{e^2 e^{-qd}}{2q\epsilon_0 \epsilon_r}. \tag{7.10}$$

E_{F} denotes the Fermi level. Assuming a narrow quantum well with a single quantization energy E_{2D}, the 2DEG electron density can be expressed as [Sch01]

$$n_{\mathrm{2D}} = \frac{m^* k_B T}{\pi \hbar^2} \ln\left(1 + \exp\left(\frac{E_{\mathrm{F}} - E_{\mathrm{2D}}}{k_B T}\right)\right). \tag{7.11}$$

Inserting Eqn. (7.11) into Eqn. (7.9) now leads to the dielectric function for a 2DEG as

$$\epsilon_e^{-1}(q,0,d) = \frac{U_{\mathrm{ext}}(q,d) + U_{\mathrm{ind}}(q,d)}{U_{\mathrm{ext}}(q,d)} = \left[1 + \frac{\lambda_{\mathrm{2D}}}{q}\right]^{-1}, \tag{7.12}$$

where the Debye screening wave number for a 2DEG is given by [And82]

$$\lambda_{2D} = \frac{e^2 m^*}{2\pi\epsilon_0\epsilon_r\hbar^2}\left[1+\exp\left(\frac{E_{2D}-E_F}{k_BT}\right)\right]^{-1}. \tag{7.13}$$

7.2.2 3DEG

Analogously to the 2DEG the Fourier components of the Poisson equation are

$$-q^2U_{ind}(q,z)+\partial_z^2U_{ind}(q,z) = -\frac{e^2\delta n_{3D}(q,z)}{\epsilon_0\epsilon_r}\Theta(z-d), \tag{7.14}$$

where a constant electron density n_{3D} for $z > d$ and zero electron density for $z < d$ has been assumed. For $z > d$ the induced electron density is given within the Debye approximation as

$$\delta n_{3D}(q,z) = \frac{\partial n_{3D}}{\partial E_F}\left[U_{ind}(q,z)+U_{ext}(q,z)\right]. \tag{7.15}$$

Using the formula for the bulk electron density (see Eqn. 3.5)

$$n_{3D} = 2\left(\frac{m^*k_BT}{2\pi\hbar}\right)^{3/2}\mathcal{F}_{1/2}\left(\frac{E_F-E_c}{k_BT}\right) \tag{7.16}$$

the bulk Debye screening wave number can be written as [Lan91]

$$\lambda_{3D} = \sqrt{\frac{e^2}{\epsilon_0\epsilon_r}\frac{\partial n_{3D}}{\partial E_F}} = \sqrt{\frac{e^2\ n_{3D}}{\epsilon_0\epsilon_r}\frac{\mathcal{F}_{-1/2}\left(\frac{E_F-E_c}{k_BT}\right)}{\mathcal{F}_{1/2}\left(\frac{E_F-E_c}{k_BT}\right)}}. \tag{7.17}$$

Solving Eqn. (7.14) using Eqn. 7.15 and Eqn. 7.10 leads to

$$\begin{aligned} U_{ind}(q,0<z<d) &= \frac{e^2e^{q(z-2d)}}{2q\epsilon_0\epsilon_r}\left[\frac{2q}{q+\sqrt{\lambda_{3D}^2+q^2}}-1\right] \\ U_{ind}(q,z>d) &= \frac{-e^2e^{-qz}}{2q\epsilon_0\epsilon_r}+\frac{e^2e^{-qd+\sqrt{\lambda_{3D}^2+q^2}(d-z)}}{\epsilon_0\epsilon_r\left[q+\sqrt{\lambda_{3D}^2+q^2}\right]}. \end{aligned} \tag{7.18}$$

Note that U_{ind} is continuously differentiable at $z = d$. Equation (7.18) results exactly in the potential distribution as obtained from the mirror charge method for $\lambda_{3\mathrm{D}} \to \infty$ (ideal lead). With the external potential

$$U_{\mathrm{ext}}(q, z) = \frac{e^2 e^{-q|z|}}{2q\epsilon_0\epsilon_r}, \tag{7.19}$$

the relevant dielectric function for $z > d$ can be expressed as

$$\epsilon_e^{-1}(q, 0, z > d) = \frac{2qe^{-(z-d)(\sqrt{\lambda_{3\mathrm{D}}^2+q^2}-q)}}{q + \sqrt{\lambda_{3\mathrm{D}} + q^2}}. \tag{7.20}$$

7.3 Remote quantum well

Inserting the static dielectric function (7.12) for a 2DEG into Eqn. (7.2) and using plane waves for the initial and final quantum well wave functions leads to the matrix element for the remote Coulomb scattering with a 2DEG

$$\begin{aligned}\left|M_{i\boldsymbol{k}\to j\boldsymbol{k}'}^{2\mathrm{DEG}}\right|^2 = \Bigg|\int_A \frac{e^{-i\boldsymbol{k}'\boldsymbol{r}_{\shortparallel}}}{\sqrt{A}} \sum_{\boldsymbol{q}'} \frac{e^2 e^{-q'd+i\boldsymbol{q}'\boldsymbol{r}_{\shortparallel}}}{2\epsilon_0\epsilon_r A(q'+\lambda_{2\mathrm{D}})} \\ \times \left[e^{q'\frac{a_z}{2}+i\boldsymbol{q}'\frac{\boldsymbol{a}_{\shortparallel}}{2}} - e^{-q'\frac{a_z}{2}-i\boldsymbol{q}'\frac{\boldsymbol{a}_{\shortparallel}}{2}}\right] \frac{e^{i\boldsymbol{k}\boldsymbol{r}_{\shortparallel}}}{\sqrt{A}} d^2\boldsymbol{r}_{\shortparallel}\Bigg|^2 .\end{aligned} \tag{7.21}$$

Integration in real space (see appendix A.1) gives the final form of the matrix element

$$\left|M_{i\boldsymbol{k}\to j\boldsymbol{k}'}^{2\mathrm{DEG}}\right|^2 = \frac{e^4 e^{-2qd}\left[\cosh(qa_z) - \cos(\boldsymbol{q}\boldsymbol{a}_{\shortparallel})\right]}{2A^2(\epsilon_0\epsilon_r)^2(q+\lambda_{2\mathrm{D}})^2}, \tag{7.22}$$

with the momentum transfer $q = |\boldsymbol{q}| = |\boldsymbol{k} - \boldsymbol{k}'|$ and the lateral and vertical part of the dipole moment $\boldsymbol{a}_{\shortparallel}$ and a_z, respectively.

Note that the matrix element decreases exponentially with the distance and the momentum transfer which is determined by the energy transfer and the parabolic band dispersion in the well.

7.4 Remote bulk carriers

Using plane waves for the bulk electron wave functions, and assuming an infinitely high barrier at $z = d$ (Fig. 7.1) leads to the boundary conditions $\psi_{\boldsymbol{k}}(d) = 0$ and $\psi_{\boldsymbol{k}'}(d) = 0$. Inserting the static dielectric function for $z > d$ (7.20) into Eqn. (7.2) leads to

$$\begin{aligned}\left|M^{\mathrm{3DEG}}_{i\boldsymbol{k}\to j\boldsymbol{k}'}\right|^2 = \frac{1}{A^2}\Bigg|\int_d^\infty dz\sqrt{\frac{2}{L}}\sin(k'_z(z-d))\\ \frac{e^2}{2\epsilon_0\epsilon_r q}\frac{2qe^{-qd+\sqrt{\lambda_{\mathrm{3D}}^2+q^2}(d-z)}}{q+\sqrt{\lambda_{\mathrm{3D}}^2+q^2}}\left[e^{q\frac{a_z}{2}+i\boldsymbol{q}\frac{\boldsymbol{a}_{\shortparallel}}{2}}-e^{-q\frac{a_z}{2}-i\boldsymbol{q}\frac{\boldsymbol{a}_{\shortparallel}}{2}}\right]\\ \sqrt{\frac{2}{L}}\sin(k_z(z-d))\Bigg|^2,\end{aligned} \tag{7.23}$$

where the integration in the lateral directions has already been performed. An integration in the z-direction (see appendix A.2) results an expression for the matrix element

$$\begin{aligned}\left|M^{\mathrm{3DEG}}_{i\boldsymbol{k}\to j\boldsymbol{k}'}\right|^2 = \frac{2e^4e^{-2qd}\left[\cosh(qa_z)-\cos(\boldsymbol{q}\boldsymbol{a}_{\shortparallel})\right]}{(AL)^2(\epsilon_0\epsilon_r)^2}\\ \frac{\lambda_{\mathrm{3D}}^2+q^2}{(\sqrt{\lambda_{\mathrm{3D}}^2+q^2}+q)^2}\left[\frac{1}{p_z^2+\lambda_{\mathrm{3D}}^2+q^2}-\frac{1}{q_z^2+\lambda_{\mathrm{3D}}^2+q^2}\right]^2,\end{aligned} \tag{7.24}$$

with $q_z = k'_z - k_z$ and $p_z = k'_z + k_z$ and the momentum change in lateral direction $\boldsymbol{q}$.

Now all expressions are ready for a numerical evaluation of the remote Coulomb scattering probabilities for different device geometries.

8 The role of Coulomb scattering

The issue of carrier relaxation in semiconductor QD states has attracted much attention during the last decade since it is of particular scientific interest and of central importance for the development of fast optoelectronic devices such as QD laser diodes (see Ref. [Gru00b] and references therein), memory devices [Yus97, Fin98, Koi00] and photoelectronic devices [Böd99, Shi99, Kro03]. Time-resolved photoluminescence spectroscopy with picosecond [Ohn96, Adl96, Gro97] and subpicosecond resolution [San97, Mor99b, Zha00] as well as picosecond and subpicosecond optical pump-probe experiments [Fel01, Sos98] have been applied to obtain information about the carrier relaxation in various III-V QD systems. At high excitation densities, carrier-carrier Coulomb scattering (Auger effect) leads to fast and efficient filling of the QD states, whereas the carrier-phonon scattering is thought to be the dominant relaxation path at low densities [Ver00, Fer99, Mag02b, Mag02a]. The measured time-constant for low-density excitonic carrier relaxation has been reported to vary from about 40 ps [Mal01] to about 150 ps [Hei00].

It has been predicted that an electron-phonon scattering process or multi-phonon process [Mag02c] should suffer from phonon bottleneck effect [Boc90] due to the discrete energy dispersion of QDs and optical phonon modes. A strict bottleneck has never been observed, but depending on the detailed shape of the QDs, the relaxation can be quenched to a ns time scale [Hei01]. Such a bottleneck effect can be overcome by a Coulomb scattering process with continuum states where energy conservation can easily be fulfilled.

The Coulomb scattering with electrons located in the wetting layer has been subject of intense experimental [Ray00, Mor99a],

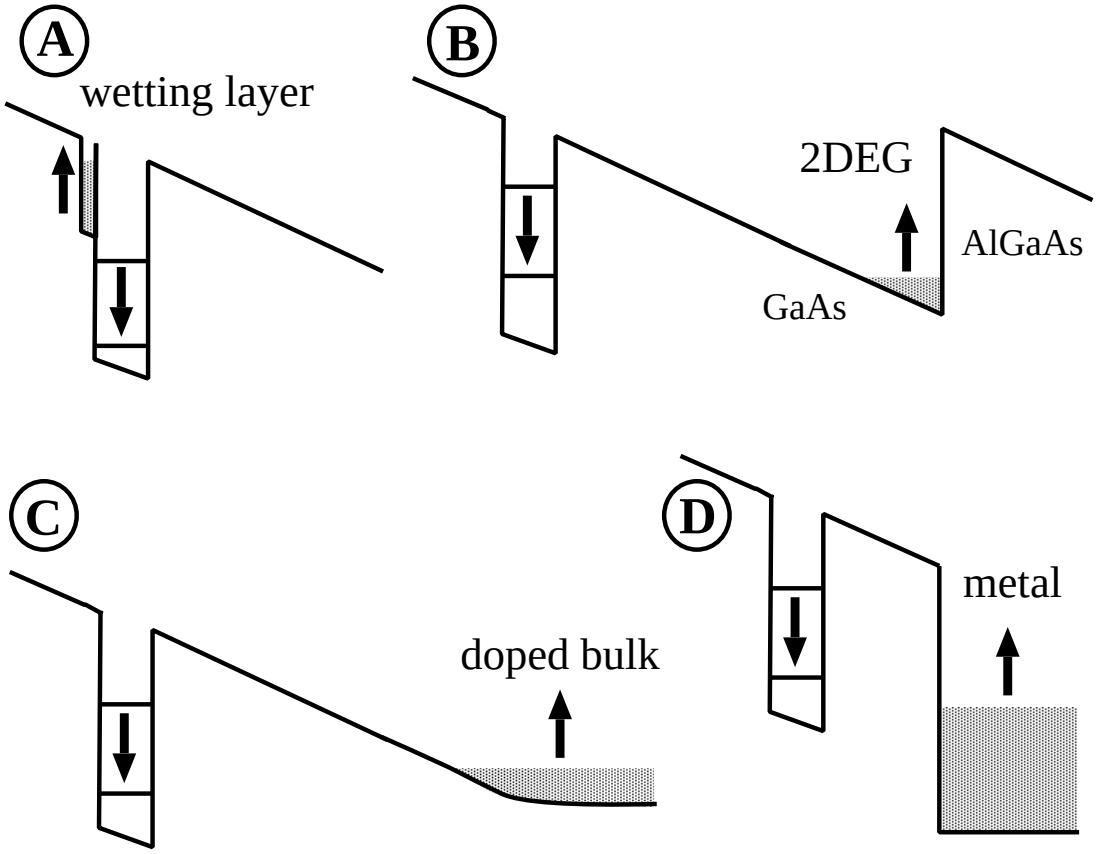

Figure 8.1: sketched band diagrams, showing the Coulomb scattering with the wetting layer (A), a remote two-dimensional electron gas (B), a remote doped bulk region (C) and a metal contact (D)

as well as theoretical [Usk97, Usk98] research, and the dependence of the capture and emission rates on the local electron density is well known. For example, the hysteresis and the dynamical bistability of the memory structure as reported in Ref. [Yus97] can be explained by Auger-type electron capture and emission [Rac02b], using the Auger coefficients found in the literature [Ray00, Usk98], but a phonon process could not be precluded. For such nonvolatile memory structures a very slow electron kinetics is essential, to preserve the occupation of the QDs over a long time range.

In some devices it can occur that due to the depletion of the local electron density at the position of the QDs by local electric fields

[Fry00, Kap00b], Coulomb scattering with the local wetting layer can be excluded. Electrons at some distance from the QDs may then be the next potential scattering partners for the QD electrons. In addition, Ref. [San02] reports of an increase of the electron relaxation with increasing photo-generated carrier injection for QDs without the existence of a wetting layer. This indicates that the dimension of the continuum electrons is not relevant, and scattering with bulk electrons can come into play.

Therefore, the role of Coulomb scattering with continuum electrons located not only in the wetting layer (Fig. 8.1: A), but also with remote electrons [Wet03a, Wet04] is investigated. These electron densities can be defined by a two-dimensional electron gas (2DEG) at some distance from the QDs (B), a doped region (C) or a metal contact (D) (3DEG). With the numerical evaluations of the scattering probabilities as derived in chapter 7, the role of Coulomb scattering in QD devices is discussed for different device configurations. According to the geometry and the size of InAs QDs which have a typical base length of about 10 nm and a strong quantization in z-direction, a transition dipole moment of a_x=5 nm, a_y=0 nm, and a_z=0 nm is used.

In the following context an electron relaxation in the QD due to Coulomb scattering is called "Auger effect", where an energy absorption in the QD is called "impact excitation". One may also call the latter process impact ionization which is less accurate since the QD does not change its total charge. The nomenclature is historically motivated from the Auger effect and impact ionization of semiconductor impurity atoms [Sch87, Lan91].

8.1 The wetting layer

First, calculations of the Auger and impact excitation probabilities as a function of the electron density per unit area in the wetting layer are performed, where the electrons confined in the wetting layer are approximated as a two-dimensional electron gas with a

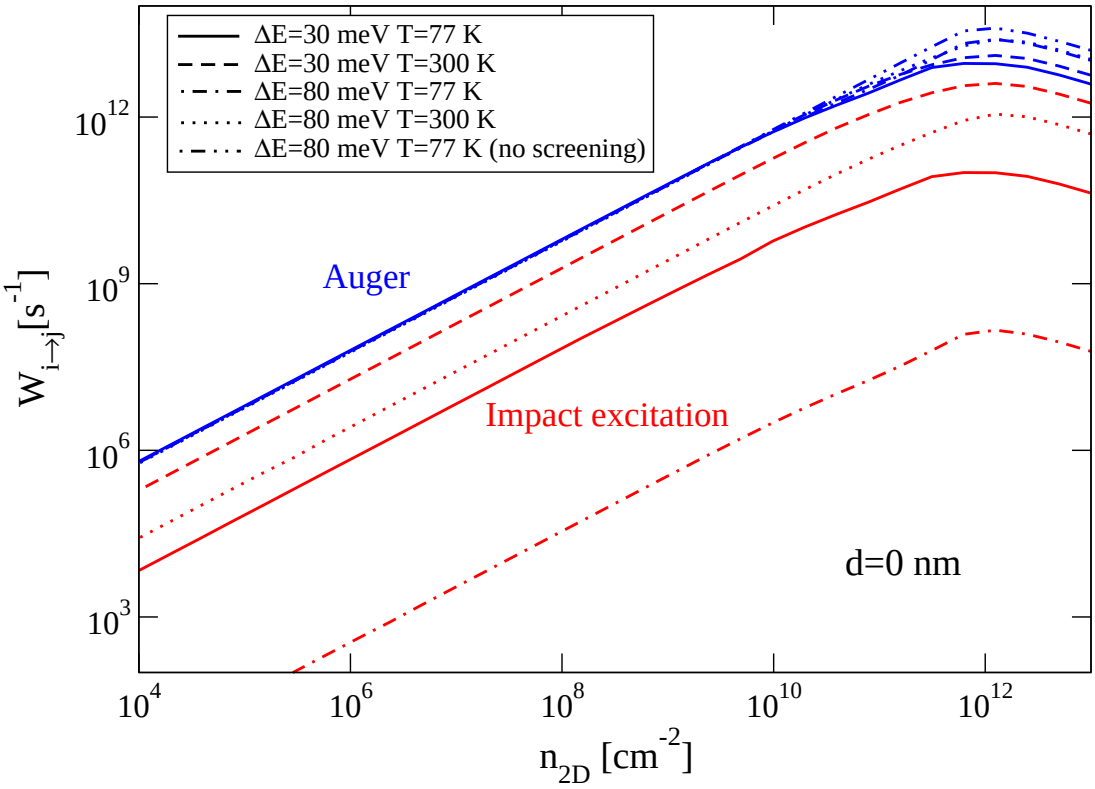

Figure 8.2: Auger (blue) and impact excitation (red) probabilities as a function of the 2DEG density at d=0 nm (wetting layer): solid lines: ΔE=30 meV, 77 K; dashed lines: ΔE=30 meV, 300 K; dash-dotted lines: ΔE=80 meV, 77 K; dash-dotted lines: ΔE=80 meV, 300 K; dash-double-dotted lines: ΔE=80 meV, 77 K, without screening [Wet03a]

vanishing distance d=0 nm from the QDs. The effective mass of the wetting layer material is m^*_{InAs}=0.023 m_0. Different QD level spacings $\Delta E = |E_j - E_i|$ are used. Figure 8.2 shows the resulting probabilities for ΔE=30 meV and 80 meV at 77 K and 300 K. The Auger probabilities hardly depend on ΔE and the temperature. For densities less than 10^{10} cm^{-2} the Auger probability is a linear function of the density. A fit $W_{i\to j} = T^{\mathrm{2D}}_{\mathrm{Aug}} n_{\mathrm{2D}}$ for low densities leads to an Auger relaxation coefficient of $T^{\mathrm{2D}}_{\mathrm{Aug}}$ =60 cm^{2}s^{-1}. This value is about one order of magnitude larger than the corresponding value

reported in Ref. [Usk98] (1 cm^2s^{-1}). This deviation can be explained by the different values for the transition dipole moment and the effective mass used in this work. Note that the experimental Auger capture coefficients of Ref. [Ray00] (10^{-8} cm^4s^{-1}) are also much larger than in Ref. [Usk98] (2×10^{-12} cm^4s^{-1}). For large densities, i.e., when the 2DEG becomes degenerate, the density dependence becomes nonlinear, and the probabilities are even reduced. Due to the parabolic bands in the 2DEG the momentum change q is reduced for high densities and for a fixed energy transfer ΔE, leading to smaller values for the matrix element (7.22) for d=0 nm. A similar behavior is found in Ref. [Boc92], where screening for the wetting layer has been described dynamically.

The corresponding impact excitation probabilities are also displayed in Fig. 8.2. They depend strongly on ΔE and T. The ratio between the impact excitation and Auger probabilities is given by the Boltzmann factor $\exp(-\Delta E/(k_BT))$. Latter is in agreement with a detailed balance consideration on the transition probabilities between equilibrium distributed QD states.

The Auger probability for ΔE=80 meV and T=77 K but neglecting screening effects is also plotted in Fig. 8.2. Obviously, screening effects play only a role for densities typically larger than 10^{10} cm^{-2}.

Attributing to phonon-assisted relaxation mechanism a time constant of about 150 ps [Hei00], Coulomb scattering with wetting layer electrons gains relevance if the electron density injected in the wetting layer is larger than about 10^9 cm^{-2}.

8.2 Remote 2DEG

A remote two-dimensional electron gas at some distance d from the QDs is considered next. Such a setup occurs for example in applications as QD-based transistors where the conductance of a 2DEG channel in the vicinity of the QDs is determined by the occupation of the QDs [Yus97, Shi99]. High Coulomb scattering rates between the QDs and the 2DEG would lead to a reduction of the lifetime

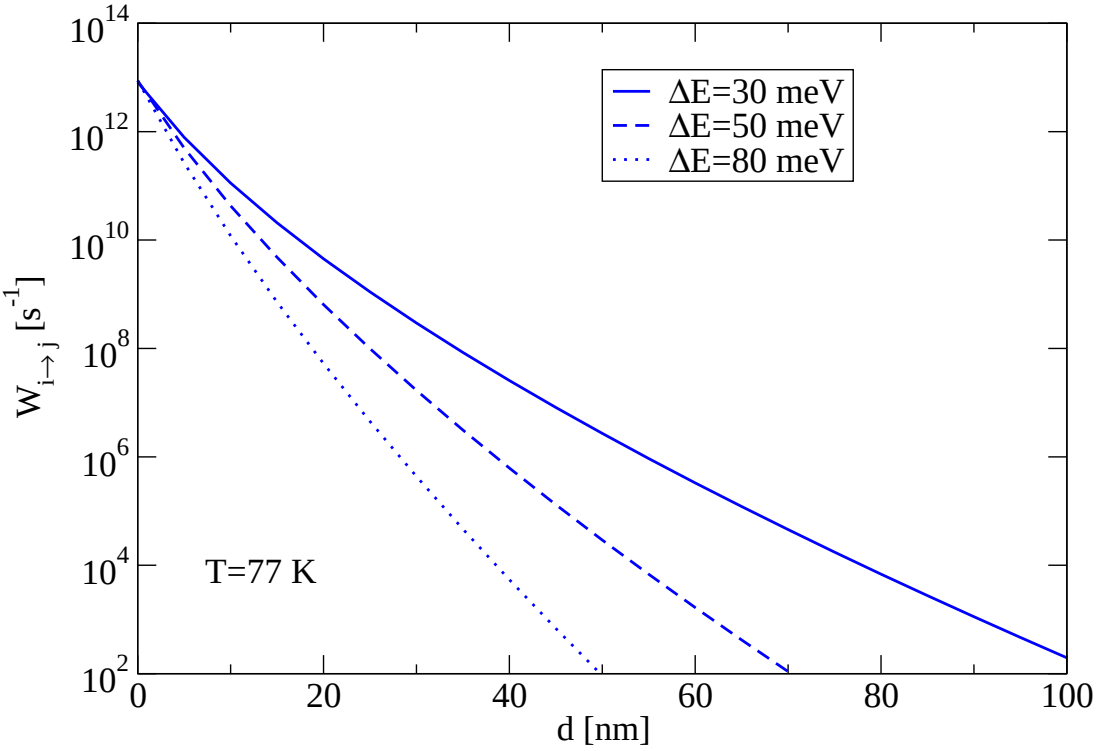

Figure 8.3: Remote Auger probabilities as a function of the distance of the 2DEG from the QDs for n_{2D} =10^{11} cm^{-2}, ΔE =30 meV (solid line), ΔE =50 meV (dashed line) and ΔE =80 meV (dotted line) at 77 K

of charged QD states, and therefore would influence the quality of such a device.

Figure 8.3 shows the remote Auger probabilities as a function of the distance d between the QDs and the 2DEG, for $n_{2D} = 10^{11}$ cm^{-2}, m^*_{GaAs}=0.06 m_0, T=77 K and ΔE=30 meV, ΔE=50 meV and ΔE=80 meV. The Auger probabilities decrease exponentially with d, depending on the energy transfer and the corresponding momentum change q. Coulomb scattering is already reduced by about three to five orders of magnitude for d=20 nm. Compared to the size of the QDs, the Coulomb scattering with a 2DEG can be attributed a rather local character.

For example, in structures as reported in Ref. [Shi99], where the distance between the QDs and the 2DEG is rather small (d=10 nm)

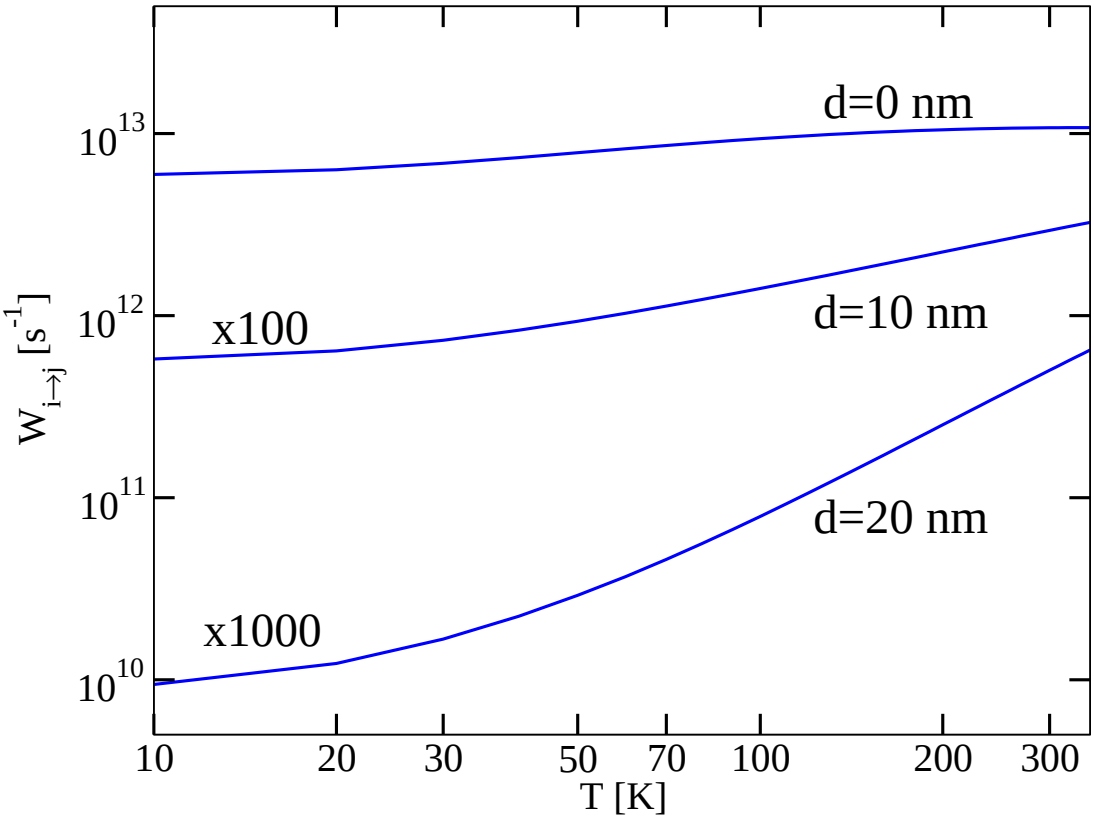

Figure 8.4: Remote Auger probabilities for n_{2D} =10^{11} cm^{-2} as a function of the temperature for d=0 nm, 10 nm, and 20 nm and for ΔE=80 meV and m^*_{GaAs}=0.06 m_0

the results indicate a strong Coulomb scattering. On the other hand, a life time limitation of charge QD states due to scattering with the 2DEG can be excluded for structures as in Ref. [Yus97], where the distance d=200 nm is rather large.

The temperature dependence of the Auger relaxation probabilities is often neglected [Fel01], but its theoretical knowledge can help to clarify capture and relaxation mechanisms in QDs. With the detailed calculations performed in this work also this aspect can be included. Figure 8.4 shows the Auger probabilities as a function of T for d=0 nm, 10 nm, and 20 nm with m^*_{GaAs} = 0.06 m_0. Interestingly, the probabilities depend on the temperature and the dependence rises with d, which can be explained by the different momentum change of the thermally occupied continuum states. A

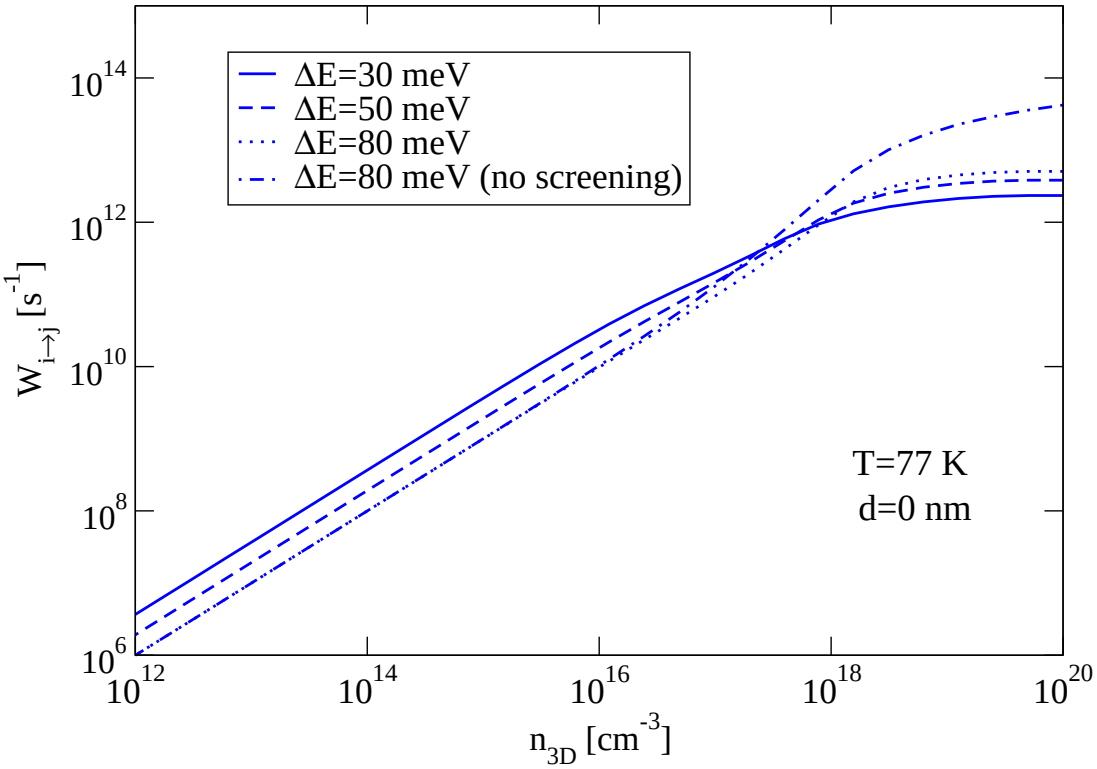

Figure 8.5: Density dependence of the Auger probabilities for ΔE =30 meV (solid line), ΔE =50 meV dashed line, ΔE =80 meV (dotted line) and ΔE =80 meV without screening (dash-dotted line) at 77 K and with d =0 nm and m^*_{GaAs}=0.06 m_0

similar temperature behavior has been found for example by time-resolved photoluminescence spectroscopy in Ref. [Ohn96].

8.3 Remote 3DEG

Next, the scattering with bulk electrons at some distance from the QDs is considered. These can be electrons of an n-doped region of a diode structure or a metal contact. Figure 8.5 shows the Auger probability as a function of the bulk electron density $n_{3\mathrm{D}}$ for ΔE=30 meV (solid line), ΔE=50 meV (dashed line) and ΔE=80 meV (dotted line) with d=0 nm at 77 K. As for the 2DEG, the Auger probabilities are linear in $n_{3\mathrm{D}}$ for low densities. Here, the

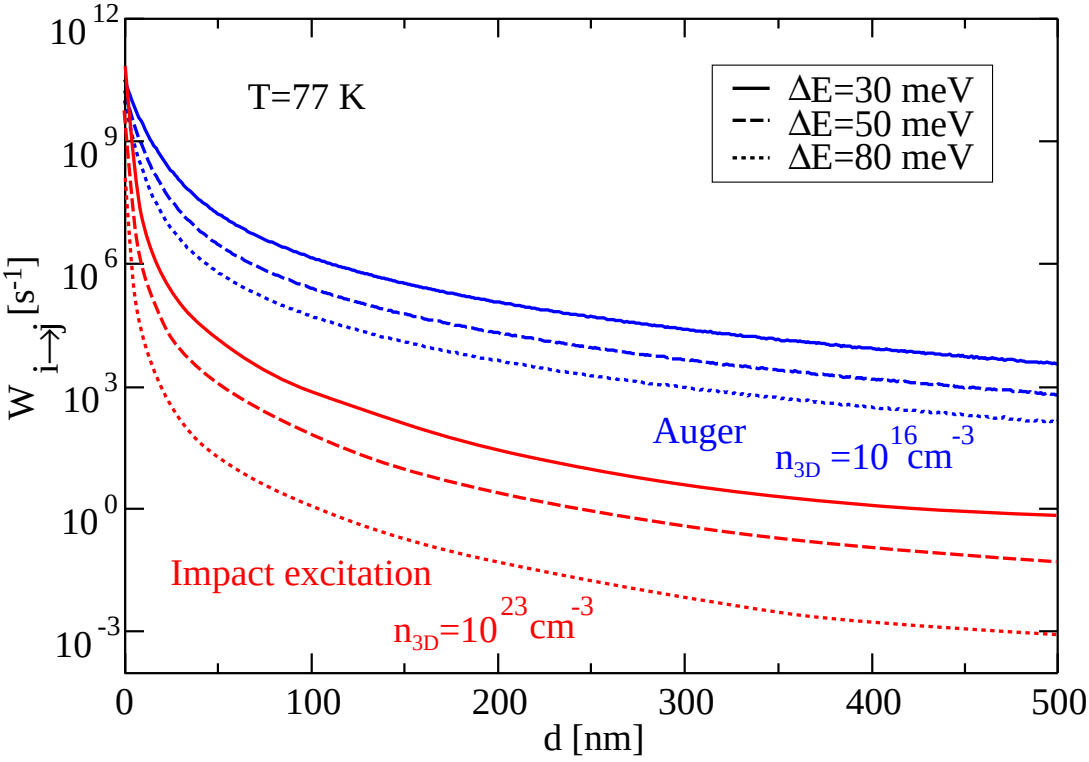

Figure 8.6: The Auger probabilities (blue) for n_{3D}=10^{16} cm^{-3}, m^*=0.06 m_0) and the impact excitation probabilities (red) for n_{3D}=10^{23} cm^{-3}, m^*=m_0) as a function of d for ΔE=30 meV (solid line), ΔE=50 meV (dashed line), and ΔE=80 meV (dotted line) at 77 K

fitted Auger coefficients $T^{3D}_{Aug} = W_{i\to j}/n_{3D}$ depend on the QD level spacing. The values T^{3D}_{Aug}=4.7×10^{-8} cm^{3}s^{-1}, 1.9×10^{-8} cm^{3}s^{-1} and 1.0×10^{-8} cm^{3}s^{-1} are obtained for ΔE=30 meV, ΔE=50 meV, and ΔE=80 meV, respectively. For high electron densities a deviation from this linear behaviour occurs, since pairs of occupied and unoccupied continuum states can only be found near the Fermi level. The resulting Auger probability neglecting screening effects is also plotted for ΔE=80 meV, showing that screening is only important for densities above 10^{17} cm^{-3}. Therefore, if QDs are embedded within doped buffer layers with doping concentrations above 10^{16} cm^{-3}, scattering times of about 100 ps or even less are expected, and Coulomb scattering gains relevance for such concentrations. Exper-

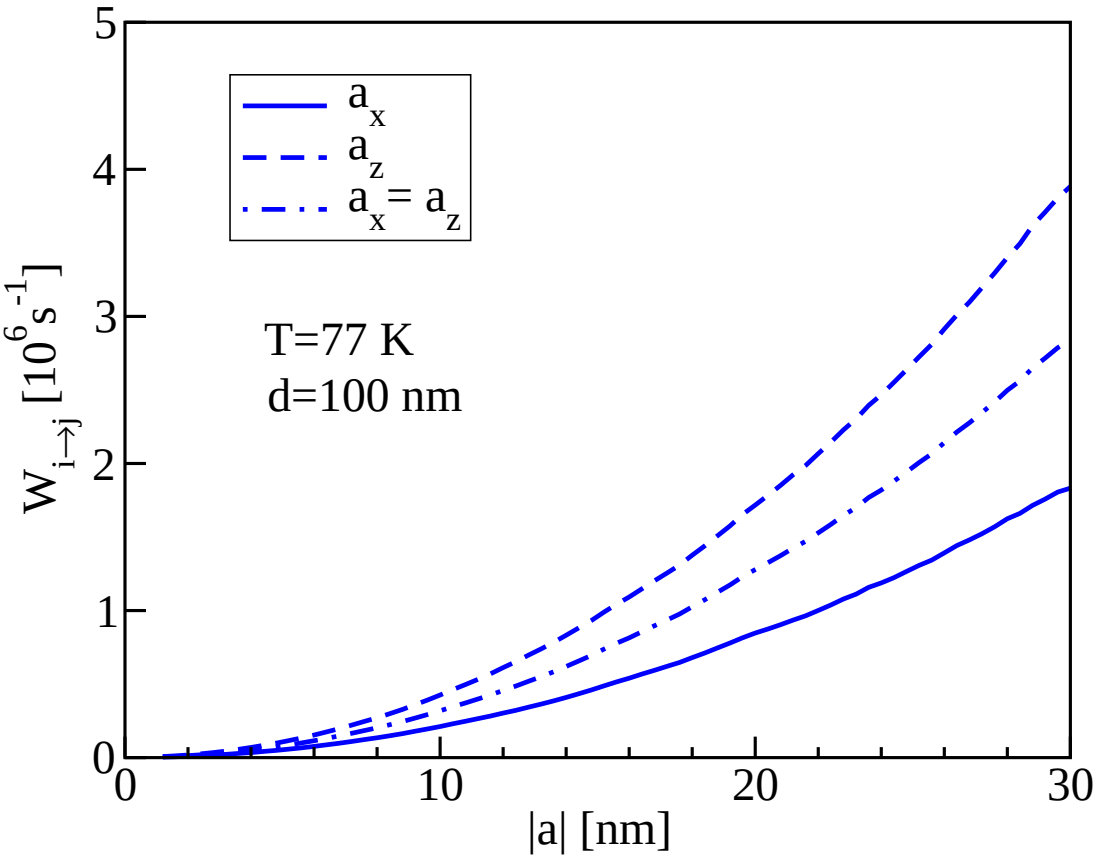

Figure 8.7: dependence of the Auger probability on the transition dipole moment for d=100 nm, n_{3D}=10^{16} cm^{-3}, T=77 K, ΔE=80 meV and m^*=0.06 m_0: $a_x \neq 0$, a_z=0 (solid line); a_x=0, $a_z \neq 0$ (dashed line) and a_x=$a_z \neq 0$ (dash-dotted line); a_y=0 for all curves

imentally for example, a relaxation time of 17 ps has been found for an optically generated electron excitation density of 2.3×10^{16} cm^{-3} [San97].

The dependence of the Auger probabilities on the distance d between the QD and the bulk electrons is investigated next. The distance can be defined for example by the bias dependent depletion layer width in a pn diode. The resulting curves for n_{3D}=10^{16} cm^{-3}, m^*_{GaAs} =0.06 m_0, ΔE =30 meV (solid line), ΔE =50 meV (dashed line), and ΔE =80 meV (dotted line) at 77 K are shown in Fig. 8.6. Compared to the remote 2DEG scattering, momentum in the 3DEG

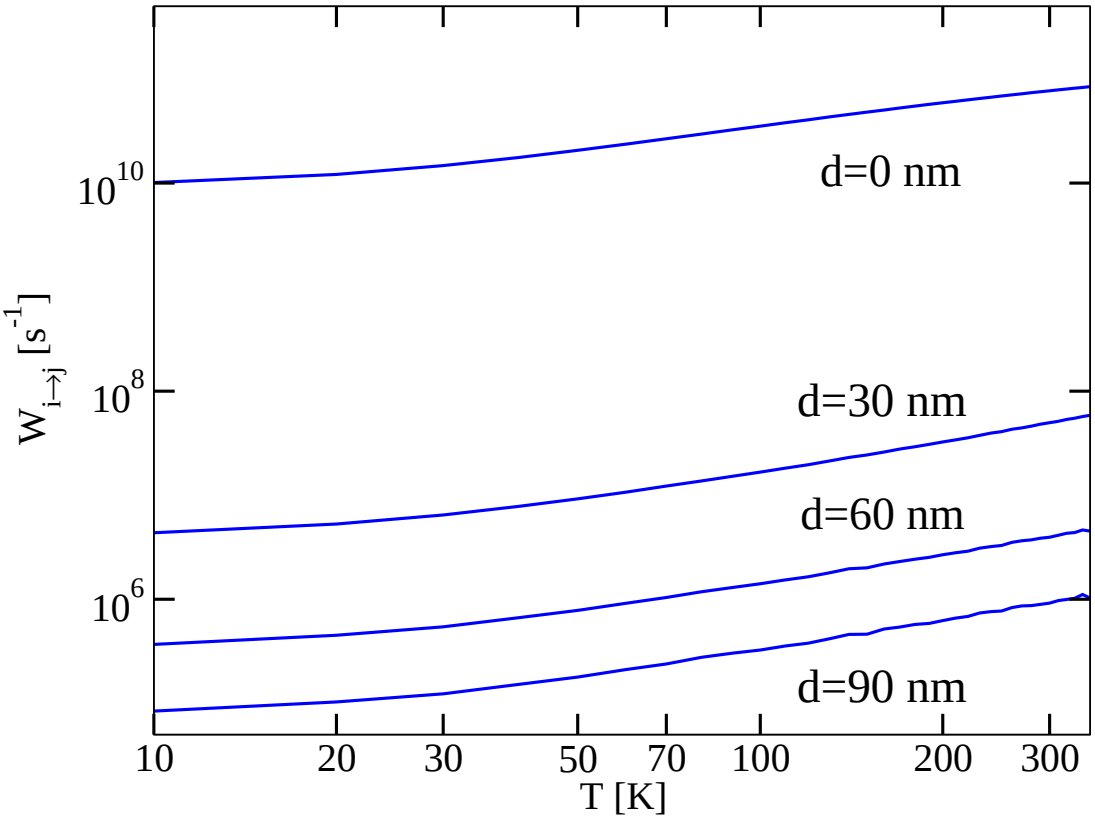

Figure 8.8: temperature dependence of the Auger probablilities for n_{3D}=10^{16} cm^{-3}, m^*=0.06 m_0, d=0 nm, 30 nm, 60 nm, and 90 nm and ΔE=80 meV

can additionally be changed in the third dimension. For low d, the distance dependence is high, similar to the 2DEG, but for large distances the dependence becomes weaker on a low level.

QDs embedded in a *pn* diode, where the QDs are positioned within 3×10^{16} cm^{-3} n-doped GaAs layers similar to the device investigated in the chapters 3 to 5 shall be another example. Such a device has been investigated in DLTS experiments, and a level spacing between the ground and excited states of ΔE =82 meV with an emission time of 62 ms at T=40 K has been observed [Kap00a]. The emission from the QD ground state level is hereby dominated by an excitation into the excited state, from which the electron escapes into the continuum by a fast tunneling process. Taking into account the Boltzmann factor between excitation and relax-

ation processes a time scale for the relaxation process from the excited state into the ground state of about 3 ps can be estimated. Scattering with wetting layer electrons can be excluded since the wetting layer is not occupied due to the electric field in the depletion layer. From Fig. 8.2 one can see that a wetting layer density of about n_{2D} =10^{10} cm^{-2} would be necessary to obtain a ps time scale. From the parabolic band bending and a QD ground state energy of 200 meV below the conduction band edge an extension of the depletion layer of d=90 nm measured from the QD layer can be estimated. The results obtained so far supply an electron relaxation time scale of milliseconds or above for a Coulomb scattering in this device. This is much too slow to explain the observations made in the experiments, indicating a phonon mediated emission process. Neglecting the strong electric field in growth direction in the depletion layer (about several tens of kV/cm) and the simplifications made for the QD band structure in the model used here, should also be notified.

Another interesting point is how a metal contact with its high electron density limits the lifetime of charged QDs. Therefore, the impact excitation probabilities are also displayed in Fig. 8.6 for n_{3D}=10^{23} cm^{-3} which is a typical electron density in metal contacts, and m^*=m_0. Transition times of the order of an hour for ΔE=80 meV and d=400 nm are obtained. This goes well with the observation of bistable behavior in QD structures on this time scale [Yus97, Rac02b, Rac03], where it is necessary that scattering processes with the metal back contact do not lead to a fast electron kinetics.

So far all calculations have been made for a fixed lateral transition dipole moment, but the results can easily be rescaled for other QDs with other corresponding transition dipole moments. Figure 8.7 shows the dependence of the Auger probability on the transition dipole moment $-e\boldsymbol{a}$ which can be well approximated by a quadratic law resulting from the Taylor expansion of Eqn. (7.24). The Taylor expansion also explains that the transition probabilities are enlarged

by a factor of 2 for vertical dipole moments (in growth direction) compared to the lateral dipole moments studied throughout this work.

Figure 8.8 shows the temperature dependence of the Auger probabilities for n_{3D}=10^{16} cm^{-3}, m^*=0.06 m_0, d=0 nm, 30 nm, 60 nm, and 90 nm. In contrast to the 2DEG (Fig. 8.4), where the temperature dependence increases with the distance to the continuum electrons, the temperature dependence is similar for all distances for a 3DEG. The values for the Auger probabilities are reduced to about one order of magnitude for very low temperatures, compared to room temperature. The temperature dependence of the Auger probabilities clearly depends on the dimension of the continuum electrons.

Summary

In summary, Coulomb charging and Coulomb scattering in quantum dot (QD) devices has been studied.

In order to investigate self-organized QDs by capacitance-voltage (C-V) spectroscopy, a deep knowledge of the charge and potential distributions is necessary. Here, feasible models have been proposed to perform numerical self-consistent simulations of the charge and potential distribution in QD arrays, resulting in theoretical C-V characteristics.

A self-consistent one-dimensional model has been proposed in chapter 3 where the QDs have been modeled by a homogeneously broadened density of states. With this model is was possible to obtain values for the electronic level energies of self-organized InAs QDs and their broadenings by a fit to experimental data in chapter 4. An energy of 211 meV and a broadening of 141 meV has been found for the spin-degenerate QD ground state of InAs QDs on a GaAs substrate.

The sophisticated three-dimensional model also proposed in chapter 3 allows for a three-dimensional calculation of the potential and charge distribution in a QD device. To make a three-dimensional self-consistent simulation numerically feasible, the QDs have been treated as a linear perturbation of a one-dimensional approximation, where the QDs appear as a sheet charge in the semiconductor equations. Despite this crude approximation, this model allows for accurate three-dimensional simulations of QD devices with large QD arrays.

The simulations performed in chapter 5 demonstrated the detailed Coulomb charging effects that occur in a *pn* device with embedded QDs. Where the charging energy resulting from two electrons in the same QD is rather independent from the bulk charge distribution in the vicinity of the QDs, the latter has a strong impact on the Coulomb repulsion between adjacent QDs. The interplay between depletion of the surrounding bulk material and the discharging of the QDs leads to a complicated non-linear behavior of the QD en-

ergy levels during a bias sweep. Additionally, the inter-QD Coulomb charging together with the inhomogeneous QD charge distribution can lead to a broadening of the discrete single QD density of states.

A comparison between the three-dimensional and one-dimensional charging energies has shown that for QD sheet densities of 10^{10} cm^{-2} and an occupation of two or less electrons per QD one dimensional models can be applied. For larger QD occupations, or large QD sheet densities, one-dimensional models fail.

Thermal broadening and structural fluctuations have been investigated in chapter 6. The three-dimensional simulations allow to investigate Coulomb mediated broadenings and position or size fluctuations independently. It has been shown that the size fluctuations are about 30 % in self-organized InAs QDs. According to the results of 8-band $\boldsymbol{k} \cdot \boldsymbol{p}$ calculations, this size fluctuations correspond to an intrinsic energy level broadening of the QD ground state of 70 meV. This value is just half the value found with the one-dimensional model for the spin-degenerate ground state electrons.

Samples obtained from Kinetic Monte-Carlo simulations have additionally been investigated. Even marginal differences in the size distribution can be resolved by C-V spectroscopy. It has been shown that the Coulomb forces between the QDs can lead to information about the position correlations in a QD sample.

The nature of the electron kinetics in QDs is one of the main topics of recent research. Energy relaxation and excitation can be mediated by phonon assisted processes or electron-electron scattering, and a distinction between these two mechanisms is often not easy. So far, only Coulomb scattering with the continuum electrons of the local wetting layer has been investigated. Depending on the device structure also scattering with other electrons surrounding the QDs can come into play.

Therefore, Coulomb scattering between QD electrons and remote two- and three-dimensional continuum states has been described theoretically in chapter 7. The dependence on the electron density, the distance between the electron systems and the temperature de-

pendence has been investigated numerically in chapter 8. The results show a good agreement with several experiments. Typically, Coulomb scattering in QD devices has a range of tens of nanometers.

Outlook

When introducing new computational methods as has been done in this work, there will naturally be residual aspects for further investigations. Some of them are briefly outlined here.

Similar to the fit to experiments which has been performed in this work with the one-dimensional model to find values for the QD energy levels and their broadenings, a fit with the three-dimensional model as proposed in this work should be made to investigate structural fluctuations in different QD devices even more quantitatively. Such fits are of course rather expensive, but should be possible with sophisticated parallelized computer codes.

Conceivable are also other QD materials which can be charged with more carriers than InAs/GaAs QDs such as Si/Ge QDs. For such QDs materials many-particle charging effects have already been observed experimentally [Kap00b] which are covered by the model proposed in this work.

Introducing a time scale for the microscopic statistical capture and emission processes, e.g., using probabilities from literature, the effort for time-resolved simulations should be manageable compared to the stationary calculations performed here.

Additionally, optical non-resonant and resonant excitations in combination with capacitance spectroscopy should be considered. This would open the possibility to charge QDs selectively, and to quantify size distributions within QD ensembles in much more detail.

With the theoretical description of Coulomb scattering of QDs with the surrounding electron density as has been done in this work, a clear separation of phonon and Coulomb mediated energy relaxation in QDs is possible. This can help to gather insight into the phonon modes in QDs and their coupling to electrons.

Acknowledgments

I would like to take this opportunity to express my gratitude to my supervisor Prof. Dr. Eckehard Schöll, PhD for the opportunity to work in his group. His steady support has been instrumental in the success of this work. I would also like to thank Dr. Andreas Wacker for many helpful suggestions and discussions.

I appreciated very much the fruitful collaboration with Dr. Christian Kapteyn and thank him for providing his experimental results. I am grateful to Dr. Robert Heitz for his expert knowledge on the field of quantum dots.

I would like to thank all the former colleagues of the Institute of Theoretical Physics at the Technical University of Berlin for the pleasant atmosphere: Dr. Andreas Amman, Dr. Sumit Bose, Gerold Kießlich, Roland Kunert, Dr. Georg Schwarz and Grischa Stegemann, just to mention some of them. Special thanks to those who kept the computers running!

This work was supported by the DFB in the framework of Sfb296.

A Coulomb matrix elements

A.1 QD-2DEG

Integration of Eqn. (7.21)

$$\left|M^{\mathrm{2DEG}}_{i\boldsymbol{k}\to j\boldsymbol{k}'}\right|^2 = \left|\int_A \frac{e^{-i\boldsymbol{k}'\boldsymbol{r}_{\shortparallel}}}{\sqrt{A}} \sum_{\boldsymbol{q}'} \frac{e^2 e^{-q'd+i\boldsymbol{q}'\boldsymbol{r}_{\shortparallel}}}{2\epsilon_0\epsilon_r A(q'+\lambda_{\mathrm{2D}})} \times \left[e^{q'\frac{a_z}{2}+i\boldsymbol{q}'\frac{\boldsymbol{a}_{\shortparallel}}{2}} - e^{-q'\frac{a_z}{2}-i\boldsymbol{q}'\frac{\boldsymbol{a}_{\shortparallel}}{2}}\right] \frac{e^{i\boldsymbol{k}\boldsymbol{r}_{\shortparallel}}}{\sqrt{A}} d^2\boldsymbol{r}_{\shortparallel}\right|^2 . \tag{A.1}$$

in the lateral two-dimensional variables, using the relation [Lan91]

$$\frac{1}{A}\int_A e^{i(-\boldsymbol{k}'+\boldsymbol{k}+\boldsymbol{q}')\boldsymbol{r}_{\shortparallel}} d^2\boldsymbol{r}_{\shortparallel} = \delta_{\boldsymbol{q}',-\boldsymbol{k}'+\boldsymbol{k}}, \tag{A.2}$$

and introducing

$$q = |\boldsymbol{q}| = |\boldsymbol{k}-\boldsymbol{k}'| \tag{A.3}$$

leads to

$$\left|M^{\mathrm{2DEG}}_{i\boldsymbol{k}\to j\boldsymbol{k}'}\right|^2 = \left|\frac{1}{A}\frac{e^2 e^{-qd}}{2\epsilon_0\epsilon_r(q+\lambda_{\mathrm{2D}})}\left[e^{q\frac{a_z}{2}+i\boldsymbol{q}\frac{\boldsymbol{a}_{\shortparallel}}{2}} - e^{-q\frac{a_z}{2}-i\boldsymbol{q}\frac{\boldsymbol{a}_{\shortparallel}}{2}}\right]\right|^2 . \tag{A.4}$$

Equation (A.4) results directly into Eqn. (7.22)

$$\left|M^{\mathrm{2DEG}}_{i\boldsymbol{k}\to j\boldsymbol{k}'}\right|^2 = \frac{e^4 e^{-2qd}\left[\cosh(qa_z)-\cos(\boldsymbol{q}\boldsymbol{a}_{\shortparallel})\right]}{2A^2(\epsilon_0\epsilon_r)^2(q+\lambda_{\mathrm{2D}})^2}. \tag{A.5}$$

A.2 QD-3DEG

To obtain the final expression for the matrix element for the QD-3DEG Coulomb scattering an integration in z-direction has to be carried out additionally. Rewriting Eqn. (7.23)

$$\left|M^{\mathrm{3DEG}}_{i\boldsymbol{k}\to j\boldsymbol{k}'}\right|^2 = \frac{1}{A^2}\left|\int_d^\infty dz\sqrt{\frac{2}{L}}\sin(k'_z(z-d))\right.$$
$$\frac{e^2}{2\epsilon_0\epsilon_r q}\frac{2qe^{-qd+\sqrt{\lambda^2_{\mathrm{3D}}+q^2}(d-z)}}{q+\sqrt{\lambda^2_{\mathrm{3D}}+q^2}}\left[e^{q\frac{a_z}{2}+i\boldsymbol{q}\frac{\boldsymbol{a}_{\shortparallel}}{2}}-e^{-q\frac{a_z}{2}-i\boldsymbol{q}\frac{\boldsymbol{a}_{\shortparallel}}{2}}\right] \tag{A.6}$$
$$\left.\sqrt{\frac{2}{L}}\sin(k_z(z-d))\right|^2,$$

and introducing the variable $y = z - d$ leads to

$$\left|M^{\mathrm{3DEG}}_{i\boldsymbol{k}\to j\boldsymbol{k}'}\right|^2 = \frac{8e^4e^{-2qd}\left[\cosh(qa_z)-\cos(\boldsymbol{q}\boldsymbol{a}_{\shortparallel})\right]}{(AL)^2(\epsilon_0\epsilon_r)^2}$$
$$\frac{1}{(\sqrt{\lambda^2_{\mathrm{3D}}+q^2}+q)^2}\left[\int_0^\infty dy\sin(k'_z y)e^{-\sqrt{\lambda^2_{\mathrm{3D}}+q^2}y}\sin(k_z y)\right]^2. \tag{A.7}$$

The integral is given by

$$\begin{aligned}
&\int_0^\infty dy \sin(k_z' y) e^{-\sqrt{\lambda_{3\mathrm{D}}^2+q^2}y} \sin(k_z y) \\
&= \frac{1}{4}\int_0^\infty dy \left(e^{ik_z' y} - e^{-ik_z' y}\right) e^{-\sqrt{\lambda_{3\mathrm{D}}^2+q^2}y} \left(e^{ik_z y} - e^{-ik_z y}\right) \\
&= \frac{1}{4}\left[\frac{1}{i\left(k_z' + k_z - \sqrt{\lambda_{3\mathrm{D}}^2+q^2}\right)} - \frac{1}{i\left(k_z' - k_z - \sqrt{\lambda_{3\mathrm{D}}^2+q^2}\right)}\right. \\
&\left. - \frac{1}{i\left(-k_z' + k_z - \sqrt{\lambda_{3\mathrm{D}}^2+q^2}\right)} + \frac{1}{i\left(-k_z' - k_z - \sqrt{\lambda_{3\mathrm{D}}^2+q^2}\right)}\right] \\
&= -\frac{1}{2}\left[\frac{1}{(k_z'+k_z)^2 + \lambda_{3\mathrm{D}}^2 + q^2} - \frac{1}{(k_z'-k_z)^2 + \lambda_{3\mathrm{D}}^2 + q^2}\right].
\end{aligned} \tag{A.8}$$

Substituting Eqn. (A.8) into Eqn. (A.7), with Eqn. (A.3), and introducing

$$q_z = k_z' - k_z \quad \text{and} \quad p_z = k_z' + k_z, \tag{A.9}$$

leads to Eqn. (7.24)

$$\begin{aligned}
\left|M_{i\boldsymbol{k}\to j\boldsymbol{k}'}^{3\mathrm{DEG}}\right|^2 &= \frac{2e^4 e^{-2qd}\left[\cosh(qa_z) - \cos(\boldsymbol{q}\boldsymbol{a}_{\shortparallel})\right]}{(AL)^2(\epsilon_0\epsilon_r)^2} \\
&\frac{\lambda_{3\mathrm{D}}^2 + q^2}{(\sqrt{\lambda_{3\mathrm{D}}^2+q^2}+q)^2}\left[\frac{1}{p_z^2 + \lambda_{3\mathrm{D}}^2 + q^2} - \frac{1}{q_z^2 + \lambda_{3\mathrm{D}}^2 + q^2}\right]^2,
\end{aligned} \tag{A.10}$$

Physical Constants

Symbol	Description	Value
$\hbar$	Planck constant	1.05458×10^{-34} Js
k_B	Boltzmann constant	1.38006×10^{-23} J/K
e	Elementary charge	1.60219×10^{-19} C
m_0	Electron rest mass	9.109381×10^{-31} kg
ϵ_0	Vacuum permittivity	8.85418×10^{-12} F/m

Material properties

Symbol	Description	Value
ϵ_{GaAs}	Relative permittivity of GaAs	13.18
$m^*_{\mathrm{n,GaAs}}$	Electron effective mass in GaAs	0.063 m_0
$m^*_{\mathrm{l,GaAs}}$	Light hole effective mass in GaAs	0.076 m_0
$m^*_{\mathrm{h,GaAs}}$	Heavy hole effective mass in GaAs	0.5 m_0
$E_{\mathrm{g,GaAs}}$	Band gap in GaAs	1.424 eV
$\mu_{\mathrm{n,GaAs}}$	Electron mobility in GaAs	7900 cm^2/Vs
$\mu_{\mathrm{p,GaAs}}$	Hole mobility in GaAs	450 cm^2/Vs
ϵ_{InAs}	Relative permittivity of InAs	15.15
$m^*_{\mathrm{n,InAs}}$	Electron effective mass in InAs	0.0239 m_0
$m^*_{\mathrm{l,InAs}}$	Light hole effective mass in InAs	0.026 m_0
$m^*_{\mathrm{h,InAs}}$	Heavy hole effective mass in InAs	0.35 m_0
$E_{\mathrm{g,InAs}}$	Band gap in InAs	0.354 eV

(Source: [Hel82]. all values for room temperature)

Bibliography

[Adl96] F. Adler, M. Geiger, A. Bauknecht, F. Scholz, H. Schweizer, M. H. Pilkuhn, B. Ohnesorge and A. Forchel. *Optical transitions and carrier relaxation in self assembled InAs/GaAs quantum dots.* J. Appl. Phys. **80**, 4019 (1996).

[And82] T. Ando, A. B. Fowler and F. Stern. *Electronic properties of two-dimensional systems.* Rev. Mod. Phys. **54**, 437 (1982).

[Ari00] J. Arias, I. Esquivias, E. C. Larkins, S. Bürkner, S. Weisser and J. Rosenzweig. *Determination of the band offset and the characteristic interdiffusion length in quantum-well lasers using a capacitance-voltage technique.* Appl. Phys. Lett. **77**, 776 (2000).

[Ash92] R. C. Ashoori, H. L. Stormer, J. S. Weiner, L. N. Pfeiffer, S. J. Pearton, K. W. Baldwin and K. W. West. *Single-electron capacitance spectroscopy of discrete quantum levels.* Phys. Rev. Lett. **68**, 3088 (1992).

[Bim99] D. Bimberg, M. Grundmann and N.N. Ledentsov. *Quantum Dot Heterostructures.* (John Wiley & Sons Ltd., New York, 1999).

[Boc90] U. Bockelmann and G. Bastard. *Phonon scattering and energy relaxation in two-, one,- and zero-dimensional electron gases.* Phys. Rev. B **42**, 8947 (1990).

[Boc92] U. Bockelmann and T. Egeler. *Electron relaxation in quantum dots by means of Auger processes.* Phys. Rev. B **46**, 15574 (1992).

[Böd99] M. C. Bödefeld, R. J. Warburton, K. Karrai, J. P. Kotthaus, G. Medeiros-Ribeiro and P. M. Petroff. *Storage of electrons and holes in self-assembled InAs quantum dots.* Appl. Phys. Lett. **74**, 1839 (1999).

[Bro94] P. N. Brounkow, T. Benyattou, G. Guillot and S. A. Clark. *Admittance spectroscopy of InAlAs/InGaAs single-quantum-well structure with high concentration of electron traps in InAlAs layers.* J. Appl. Phys. **77**, 240 (1994).

[Bro96] P. N. Brounkow, T. Benyattou and G. Guillot. *Simulation of the capacitance-voltage characteristics of a single-quantum-well structure based on the self-consistent solution of the Schrödinger and Poisson equations.* J. Appl. Phys. **80**, 864 (1996).

[Bro98] P. N. Brounkow, V. V. Chaldyshev, A. A. Suvorova, N. A. Bert, S. G. Konnikov, A. V. Chernigovskii, V. V. Preobrazhenskii, M. A. Putyato and B. R. Semyagin. *Bistability of charge accumulated in low-temperature-grown GaAs.* Appl. Phys. Lett. **73**, 2796 (1998).

[Bru99] P. N. Brunkov, A. R. Kovsh, V. M. Ustinov, Yu. G. Musikhin, N. N. Ledentsov, S. G. Konnikov, A. Polimeni, A. Patane, P. C. Main, L. Eaves and C. M. A. Kapteyn. *Emission of electrons from the ground and first excited states of self-organized InAs/GaAs quantum dot structures.* Journal of Electronic Materials **28**, 486 (1999).

[Caz98] M. A. Cazilla, N. Lorente, R. Diez Muino, J.-P. Gauyyacq, D. Teillet-Billy and P. M. Echenique. *Theory of Auger neutralization and deexcitation of slow ions at metal surfaces.* Phys. Rev. B **58**, 13991 (1998).

[Dre94] H. Drexler, D. Leonard, W. Hansen, J. P. Kotthaus and P. M. Petroff. *Spectroscopy of quantum levels in charge-tuneable InGaAs quantum dots.* Phys. Rev. Lett. **73**, 2252 (1994).

[Eag90] D. J. Eaglesham and M. Cerullo. *Dislocation-free Stranski-Krastanow growth of Ge on Si(100).* Phys. Rev. Lett. **64**, 1943 (1990).

[Ech85] P. M. Echenique, F. Flores and F. Sols. *Lifetime of image surface states.* Phys. Rev. Lett. **55**, 2348 (1985).

[Fel01] J. Feldmann, S. T. Cundiff, M. Arzberger, G. Böhm and G. Abstreiter. *Carrier capture into InAs/GaAs quantum dots via multiple optical phonon emission.* J. Appl. Phys. **89**, 1180 (2001).

[Fer99] R. Ferreira and G. Bastard. *Phonon-assisted capture and intradot Auger relaxation in quantum dots.* Appl. Phys. Lett. **74**, 2818 (1999).

[Fin98] J. J. Finley, M. Skalitz, M. Arzberger, A. Zrenner, G. Böhm and G. Abstreiter. *Electrical detection of optically induced charge storage in self-assembled InAs quantum dots.* Appl. Phys. Lett. **73**, 2618 (1998).

[Fon93] T. Fondén and A. Zwartkruis. *Analysis of Auger spectra from a He^+ ion near a metal surface.* Phys. Rev. B **48**, 15603 (1993).

[Fry00] P. W. Fry, J. J. Finley, L. R. Wilson, A. Lemaitre, D. J. Mowbray, M. S. Skolnick, M. Hopkinson, G. Hill and J. C. Clark. *Electric-field-dependent capture and escape in self-assembled InAs/GaAs quantum dots.* Appl. Phys. Lett. **77**, 4344 (2000).

[Gro97] S. Grosse, J. H. H. Sandmann, G. von Plessen, J. Feldmann, H. Lipsanen, M. Sopanen, J. Tulkki and

J. Ahopelto. *Carrier relaxation dynamics in quantum dots: Scattering mechanisms and state-filling effects.* Phys. Rev. B **55**, 4473 (1997).

[Gru97] M. Grundmann and D. Bimberg. *Theory of random population for quantum dots.* Phys. Rev. B **55**, 9740 (1997).

[Gru00a] M. Grundmann. *Feasibility of 5 Gbit/s wavelength division multiplexing using quantum dot lasers.* Appl. Phys. Lett. **77**, 4265 (2000).

[Gru00b] M. Grundmann. *The present status of quantum dot lasers.* Physica E **5**, 167 (2000).

[Hei00] R. Heitz, H. Born, A. Hoffmann, D. Bimberg, I. Mukhametzhanov and A. Madhukar. *Resonant Raman scattering in self-organized InAs/GaAs quantum dots.* Appl. Phys. Lett. **77**, 3746 (2000).

[Hei01] R. Heitz, H. Born, F. Guffarth, O. Stier, A. Schliwa, A. Hoffmann and D. Bimberg. *Existence of a phonon bottleneck for excitons in quantum dots.* Phys. Rev. B **64**, 241305(R) (2001).

[Hel82] K.H. Hellwege and O. Madelung, editors. *Landolt-Börnstein: Numerical Data and Functional Relationships in Science and Technology*, volume III/17a. (Springer, Berlin, Heidelberg, New York, 1982).

[Kap98] C. M. A. Kapteyn, F. Heinrichsdorff, O. Stier, M. Grundmann and D. Bimberg. *Electron emission from InAs quantum dots.* In D. Gershoni, editor, *Proc. 24th International Conference on the Physics of Semiconductors (ICPS-24), Jerusalem 1998*, page 1339, World Scientific, 1998.

[Kap99] C. M. A. Kapteyn, F. Heinrichsdorff, O. Stier, R. Heitz, M. Grundmann, N. D. Zakharov, D. Bimberg and

P. Werner. *Electron escape from InAs quantum dots.* Phys. Rev. B **60**, 14265 (1999).

[Kap00a] C. M. A. Kapteyn, M. Lion, R. Heitz, D. Bimberg, P.N. Brunkov, B.V. Volovik, S.G. Konnikov, A.R. Kovsh and V.M. Ustinov. *Hole and electron emission from InAs quantum dots.* Appl. Phys. Lett. **76**, 1573 (2000).

[Kap00b] C. M. A. Kapteyn, M. Lion, R. Heitz, D. Bimberg, C. Miesner, T. Asperger, K. Brunner and G. Abstreiter. *Many-particle effects in Ge quantum dots investigated by time-resolved capacitance spectroscopy.* Appl. Phys. Lett. **77**, 4169 (2000).

[Kie02] G. Kießlich, A. Wacker and E. Schöll. *Many-particle charging effects and recombination current through a quantum dot array.* phys. status solidi (b) **234**, 215 (2002).

[Kie03a] G. Kießlich, A. Wacker and E. Schöll. *Shot noise of coupled semiconductor quantum dots.* Phys. Rev. B **68**, 125320 (2003).

[Kie03b] G. Kießlich, A. Wacker, E. Schöll, A. Nauen, F. Hohls and R. J. Haug. *Shot noise in tunneling through a quantum dot array.* phys. status solidi (c) **0**, 1293 (2003).

[Kie03c] G. Kießlich, A. Wacker, E. Schöll, S. A. Vitusevich, A. E. Belyaev, S. V. Danylyuk, A. Förster, N. Klein and M. Henini. *Nonlinear charging effect of quantum dots in a p-i-n diode.* Phys. Rev. B **68**, 125331 (2003).

[Koi00] K. Koike, S. Saitoh, S. Li, S. Sasa, M. Inoue and Y. Yano. *Room-temperature operation of a memory-effect AlGaAs/GaAs heterojunction field-effect transistor with self-assembled InAs nanodots.* Appl. Phys. Lett. **76**, 1464 (2000).

[Kro03] M. Kroutvar, Y. Ducommun, J. J. Finley, M. Bichler, G. Abstreiter and A. Zrenner. *Wavelength selective charge storage in self-assembled InGaAs/GaAs quantum dots.* Appl. Phys. Lett. **83**, 443 (2003).

[Lan91] P. T. Landsberg. *Recombination in Semiconductors.* (Cambridge University Press, Cambridge, 1991).

[Lu98] L. Lu, J. Wang, Y. Wang, W. Ge, G. Yang and Z. Wang. *Conduction-band offset in a pseudomorphic $GaAs/In_{0.2}Ga_{0.8}As$ quantum well determined by capacitance-voltage profiling and deep-level transient spectroscopy techniques.* J. Appl. Phys. **83**, 2093 (1998).

[Luy99] R. J. Luyken, A. Lorke, A. O. Govorov, J. P. Kotthaus, G. Medeiros-Ribeiro and P. M. Petroff. *The dynamics of tunneling into self-assembled InAs dots.* Appl. Phys. Lett. **74**, 2486 (1999).

[Mag02a] I. Magnusdottir. *Modeling of phonon- and Coulomb-mediated capture processes in quantum dots.* PhD thesis, Technical University of Denmark, 2002.

[Mag02b] I. Magnusdottir, A. V. Uskov, S. Bischoff, B. Tromborg and J. Mørk. *One- and two-phonon capture process in quantum dots.* J. Appl. Phys. **92**, 5982 (2002).

[Mag02c] I. Magnusdottir, A. V. Uskov, R. Ferreira, G. Bastard, J. Mørk and B. Tromborg. *Influence of quasibound states on the carrier capture in quantum dots.* Appl. Phys. Lett. **81**, 4318 (2002).

[Mal01] S. Malik, E. C. Le Ru, D. Childs and R. Murray. *Time-resolved studies of annealed InAs/GaAs self-assembled quantum dots.* Phys. Rev. B **63**, 155313 (2001).

[Mar86] P. A. Markovich. *The Stationary Semiconductor Device Equations.* (Springer, Wien, 1986).

[Mar90] P. A. Markovich, C. A. Ringhofer and C. Schmeiser. *Semiconductor Equations.* (Springer, Wien, 1990).

[Mei01a] M. Meixner, R. Kunert, S. Bose, E. Schöll, V. A. Shchukin, D. Bimberg, E. Penev and P. Kratzer. *Monte Carlo simulation of the self-organized growth of quantum dots with anisotropic surface diffusion.* In N. Miura and T. Ando, editors, *Proc. 25th International Conference on the Physics of Semiconductors (ICPS-25), Osaka 2000*, page 381, Springer, Berlin, 2001.

[Mei01b] M. Meixner, E. Schöll, M. Schmidbauer, H. Raidt and R. Köhler. *Formation of island chains in SiGe/Si heteroepitaxy by elastic anisotropy – a Monte Carlo study.* Phys. Rev. B **64**, 245307 (2001).

[Mei01c] M. Meixner, E. Schöll, V. A. Shchukin and D. Bimberg. *Self-assembled quantum dots: Crossover from kinetically controlled to thermodynamically limited growth.* Phys. Rev. Lett. **87**, 236101 (2001). ibid **88**, 059901 (2002).

[Mei02a] M. Meixner. *Simulation of self-organized growth kinetics of quantum dots.* PhD thesis, TU Berlin, 2002.

[Mei02b] M. Meixner, R. Kunert, E. Schöll, V. A. Shchukin and D. Bimberg. *Monte-Carlo simulation of self-organized quantum dot structures: crossover from kinetics to thermodynamics.* In *Proceedings of the* 10^{th} *International Symposium on Nanostructures: Physics and Technology*, page 12, Ioffe Institute, St. Petersburg, 2002.

[Mei03a] M. Meixner, R. Kunert and E. Schöll. *Control of strain-mediated growth kinetics of self-assembled semiconductor quantum dots.* Phys. Rev. B **67**, 195301 (2003).

[Mei03b] M. Meixner and E. Schöll. *Kinetically enhanced correlation and anticorrelation effects in self-organized quantum*

dot stacks. Phys. Rev. B **67**, 121202 (2003). Rapid Communication.

[Mie00] C. Miesner, T. Asperger, K. Brunner and G. Abstreiter. *Capacitance-voltage and admittance spectroscopy of self-assembled Ge islands in Si.* Appl. Phys. Lett. **77**, 2704 (2000).

[Mil97] B. T. Miller, W. Hansen, S. Manus, R. J. Luyken, A. Lorke, J. P. Kotthaus, S. Huant, G. Medeiros-Ribeiro and P. M. Petroff. *Few-electron ground states of charge-tuneable self-assembled quantum dots.* Phys. Rev. B **56**, 6764 (1997).

[Mo90] Y.-W. Mo, D. E. Savage, B. S. Swartzentruber and M. G. Lagally. *Kinetic pathway in Stranski-Krastanov growth of Ge on Si(001).* Phys. Rev. Lett. **65**, 1020 (1990).

[Mon95] R. Monreal and N. Lorente. *Dynamical screening in Auger processes near metal surfaces.* Phys. Rev. B **52**, 4760 (1995).

[Moo65] G. E. Moore. *Cramming more components onto integrated circuits.* Electronics **38** (1965).

[Moo98] C. R. Moon, B.-D. Choe, S. D. Kwon and H. K. Shin H. Lim. *Electron distribution and capacitance-voltage characteristics of n-doped quantum wells.* J. Appl. Phys. **84**, 2673 (1998).

[Mor99a] C. G. Morgan, P. Kratzer and M. Scheffler. *Arsenic dimer dynamics during GaAs growth: Theoretical evidence for a novel chemisorption state of As_2 molecules on GaAs surfaces.* Phys. Rev. Lett. **82**, 4886 (1999).

[Mor99b] D. Morris, N. Perret and S. Fafard. *Carrier energy relaxation by means of Auger processes in InAs/GaAs self-assembled quantum dots.* Appl. Phys. Lett. **75**, 3593 (1999).

[MR95] G. Medeiros-Ribeiro, D. Leonard and P. M. Petroff. *Electron and hole energy levels in InAs self-asembled quantum dots.* Appl. Phys. Lett. **66**, 1767 (1995).

[MR97a] G. Medeiros-Ribeiro, J. M. Garcia and P. M. Petroff. *Charging dynamics of InAs self-assembled quantum dots.* Phys. Rev. B **56**, 3609 (1997).

[MR97b] G. Medeiros-Ribeiro, F. G. Pikus, P. M. Petroff and A. L. Efros. *Single-electron charging and Coulomb interaction in InAs self-assembled quantum dot arrays.* Phys. Rev. B **55**, 1568 (1997).

[Ohn96] B. Ohnesorge, M. Albrecht, J. Oshinowo, A. Forchel and Y. Arakawa. *Rapid carrier relaxation in self-assembled $In_xGa_{1-x}As/GaAs$ quantum dots.* Phys. Rev. B **54**, 11532 (1996).

[Rac02a] A. Rack. Master's thesis, TU Berlin, 2002.

[Rac02b] A. Rack, R. Wetzler, A. Wacker and E. Schöll. *Dynamical bistability in quantum dot structures: The role of Auger processes.* Phys. Rev. B **66**, 165429 (2002).

[Rac03] A. Rack, R. Wetzler, A. Wacker and E. Schöll. *Bistability and hysteresis in self-organised quantum dot structures.* In J. H. Davies and A. R. Long, editors, *Proc. 26th International Conference on the Physics of Semiconductors (ICPS-26), Edinburgh 2002*, 2003.

[Ray00] S. Raymond, K. Hinzer, S. Fafard and J. L. Merz. *Experimental determination of Auger capture coefficients in self-assembled quantum dots.* Phys. Rev. B **61**, 16331 (2000).

[Rid74] V. L. Rideout. *A review of the theory and technology for Ohmic contacs to group III-V compound semiconductors.* Sol. State El. **18**, 541 (1974).

[San97] J. H. H. Sandmann, S. Grosse, G. von Plessen, J. Feldmann, G. Hayes, R. Phillips, H. Lipsanen, M. Sopanen and J. Ahopelto. *Carrier relaxation in (GaIn)As quantum dots.* phys. status solidi (a) **164**, 421 (1997).

[San02] S. Sanguinetti, K. Watanabe, T. Tateno, M. Wakaki, N. Koguchi, T. Kuroda, F. Minami and M. Gurioli. *Role of the wetting layer in the carrier relaxation in quantum dots.* Appl. Phys. Lett. **81**, 613 (2002).

[Sch87] E. Schöll. *Nonequilibrium Phase Transitions in Semiconductors.* (Springer, Berlin, 1987).

[Sch98a] E. Schöll, editor. *Theory of Transport Properties of Semiconductor Nanostructures*, volume 4 von *Electronic Materials Series.* (Chapman and Hall, London, 1998).

[Sch98b] E. Schöll and S. Bose. *Kinetic Monte Carlo simulation of the nucleation stage of the self-organized growth of quantum dots.* Sol. State El. **42**, 1587–1591 (1998).

[Sch01] E. Schöll. *Nonlinear spatio-temporal dynamics and chaos in semiconductors.* (Cambridge University Press, Cambridge, 2001). Nonlinear Science Series, Vol. 10.

[Sel84] S. Selberherr. *Analysis and Simulation of Semiconductor Devices.* (Springer, Wien, New York, 1984).

[Shc98] V. A. Shchukin, D. Bimberg, V. G. Malyshkin and N. N. Ledentsov. *Vertical correlations and anticorrelations in multisheet arrays of two-dimensional islands.* Phys. Rev. B **57**, 12262 (1998).

[Shi99] A. J. Shields, M. P. O'Sullivan, I. Farrer, D. A. Ritchie, K. Cooper, C. L. Foden and M. Pepper. *Optically induced bistability in the mobility of a two-dimensional electron gas coupled to a layer of quantum dots.* Appl. Phys. Lett. **74**, 735 (1999).

[Sos98] T. S. Sosnowski, T. B. Norris, H. Jiang, J. Singh, K. Kamath and P. Bhattacharya. *Rapid carrier relaxation in $In_{0.4}Ga_{0.6}As/GaAs$ quantum dots characterized by differential transmission spectroscopy.* Phys. Rev. B **57**, R9423 (1998).

[Sti99] O. Stier, M. Grundmann and D. Bimberg. *Electronic and optical properties of strained quantum dots modeled by 8-band k·p theory.* Phys. Rev. B **59**, 5688 (1999).

[Str39] I. N. Stranski and L. Krastanow. *Sitzungsberichte der Akademie der Wissenschaften in Wien.* Akad. Wiss. Lit. Mainz Math.-Natur. Kl. IIb **146**, 797 (1939).

[Sze81] S. M. Sze. *Physics of Semiconductor Devices.* (Wiley, New York, 1981).

[Usk97] A. V. Uskov, F. Adler, H. Schweizer and P. H. Kuhn. *Auger carrier relaxation in self-assembled quantum dots by collisions with two-dimensional carriers.* J. Appl. Phys. **81**, 7895 (1997).

[Usk98] A. V. Uskov, J. McInerney, F. Adler, H. Schweizer and M. H. Pilkuhn. *Auger carrier capture kinetics in self-assembled quantum dot structures.* Appl. Phys. Lett. **72**, 58 (1998).

[Ver00] O. Verzelen, R. Ferreira and G. Bastard. *Polaron lifetime and energy relaxation in semiconductor quantum dots.* Phys. Rev. B **62**, 4809 (2000).

[vK81] N. G. van Kampen. *Stochastic Processes in Physics and Chemistry.* (North-Holland, Amsterdam, 1981).

[Wan96] J. B. Wang, F. Lu, S. K. Zhang, B. Zhang, D. W. Gong, H. H. Sun and Xun Wang. *Analysis of capacitance-voltage characteristics of $Si_{1-x}Ge_x$/Si quantum-well structures.* Phys. Rev. B **54**, 7979 (1996).

[War98] R. J. Warburton, B. T. Miller, C. S. Dürr, C. Bödefeld, K. Karrai, J. P. Kotthaus, G. Medeiros-Ribeiro, P. M. Petroff and S. Huant. *Coulomb interactions in small charge-tunable quantum dots: A simple model.* Phys. Rev. B **58**, 16221 (1998).

[Wet00] R. Wetzler, C. M. A. Kapteyn, R. Heitz, A. Wacker, E. Schöll and D. Bimberg. *Capacitance-voltage characteristics of InAs/GaAs quantum dots embedded in a pn structure.* Appl. Phys. Lett. **77**, 1671 (2000).

[Wet01a] R. Wetzler, C. M. A. Kapteyn, R. Heitz, A. Wacker, E. Schöll and D. Bimberg. *Capacitance–voltage characteristics of self-organized quantum dots embedded in a pn junction.* In N. Miura and T. Ando, editors, *Proc. 25th International Conference on the Physics of Semiconductors (ICPS-25), Osaka 2000*, page 1093, Springer, Berlin, 2001.

[Wet01b] R. Wetzler, C. M. A. Kapteyn, R. Heitz, A. Wacker, E. Schöll and D. Bimberg. *Capacitance–voltage spectroscopy of self-organized InAs/GaAs quantum dots embedded in a pn diode.* phys. status solidi (b) **224**, 79 (2001).

[Wet03a] R. Wetzler, A. Wacker and E. Schöll. *Coulomb scattering with remote continuum states in quantum dot devices.* Phys. Rev. B (2003). submitted (cond-mat/0307235).

[Wet03b] R. Wetzler, A. Wacker and E. Schöll. *Self-consistent Coulomb effects and charge distribution of quantum dot arrays.* Phys. Rev. B **68**, 045323 (2003).

[Wet04] R. Wetzler, A. Wacker and E. Schöll. *Non-local Auger effect in quantum dot devices.* Semicond. Sci. Technol. (2004). HCIS-13, Modena 2003.

[Wha96] C. B. Whan, J. White and T. P. Orlando. *Full capacitance matrix of coupled quantum dot arrays: Static and dynamical effects.* Appl. Phys. Lett. **68**, 2996 (1996).

[Yus97] G. Yusa and H. Sakaki. *Trapping of photogenerated carriers by InAs quantum dots and persistent photoconductivity in novel GaAs/n-AlGaAs field-effect transistor.* Appl. Phys. Lett. **70**, 345 (1997).

[Yus98] G. Yusa and H. Sakaki. *Trapping of a single photogenerated hole by an InAs quantum dot in GaAs/n-AlGaAs quantum trap FET and its spectral response in the near-infrared regime.* Physica E **2**, 734 (1998).

[Zha00] L. Zhang, T. F. Boggess, D. G. Deppe, D. L. Huffaker, O. B. Shchekin and C. Cao. *Dynamic response of 1.3-μm-wavelength InGaAs/GaAs quantum dots.* Appl. Phys. Lett. **76**, 1222 (2000).

Publications

- R. Wetzler, A. Wacker and E. Schöll.
  Coulomb scattering with remote continuum states in quantum dot devices.
  cond-mat/0307235 (2003)

- R. Wetzler, A. Wacker and E. Schöll.
  Self-consistent Coulomb effects and charge distribution of quantum dot arrays.
  Phys. Rev. B **68**, 045323 (2003)

- A. Rack, R. Wetzler, A. Wacker and E. Schöll.
  Dynamical bistability in quantum dot structures: The role of Auger processes.
  Phys. Rev. B **66**, 165429 (2002)

- R. Wetzler, C.M.A. Kapteyn, R. Heitz, A. Wacker, E. Schöll and D. Bimberg.
  Capacitance-voltage characteristics of InAs / GaAs quantum dots embedded in a pn structure.
  Appl. Phys. Lett. **77**, 1671 (2000)

- R. Wetzler, A. Wacker and E. Schöll.
  Non-local Auger effect in quantum dot devices.
  Semicond. Sci. Technol. submitted (2004)

- A.Rack, R. Wetzler, A. Wacker and E. Schöll.
  Bistability and hysteresis in self-organized quantum dot structures .
  In: Proc. 26th International Conference on the Physics of Semiconductors (ICPS-26), Edinburgh 2002.

- R. Wetzler, C.M.A. Kapteyn, R. Heitz, A. Wacker, E. Schöll and D. Bimberg.
  Capacitance-voltage spectroscopy of self-organized InAs/GaAs quantum dots embedded in a pn diode.
  phys. status solidi (b) **224**, 79 (2001)

- R. Wetzler, C.M.A. Kapteyn, R. Heitz, A. Wacker, E. Schöll and D. Bimberg.
  Capacitance-voltage characteristics of self-organized quantum dots embedded in a pn junction.
  In: N. Miura and T. Ando, editors, Proc. 25th International Conference on the Physics of Semiconductors (ICPS-25), Osaka 2000, page 1093, Springer, Berlin, 2001.